Event-by-event Lambda Multiplicity Distributions in Au+Au Heavy-ion Collisions from the RHIC Fixed-target Program at $\sqrt{s_{NN}} = 3.0$ GeV

by
Jonathan Gonzalo Ball Cap

A dissertation submitted to the Department of Physics,
College of Natural Sciences and Mathematics
in partial fulfillment of the requirements for the degree of

Doctor of Philosophy
in Physics

Committee Chair: Rene Bellwied
Committee Member: Daniel Cherdack
Committee Member: Scott Gilbertson
Committee Member: John Miller
Committee Member: Claudia Ratti

University of Houston
August 2023

DEDICATION/EPIGRAPH

This dissertation is dedicated to my parents, Gonzalo Ball and Emilia Cap.

ACKNOWLEDGMENTS

I am deeply grateful to express my appreciation to Dr. Rene Bellwied, who has been an exceptional advisor throughout my Ph.D. journey. Without his unwavering support and invaluable guidance, the successful completion of this work would not have been possible. Rene's mentorship has been instrumental in shaping my academic growth, and I feel immensely fortunate to have had him as my advisor.

Furthermore, I extend my sincere thanks to the esteemed members of my committee Dr. John Miller, Dr. Claudia Ratti, Dr. Daniel Cherdack and Dr. Scott Gilbertson, who have consistently provided me with their invaluable support and guidance during my Ph.D. I would like to express my heartfelt gratitude to Dr. Carlos Ordonez for being the person who helped and motivated me to embark on my Ph.D. journey. Without him, none of this would have been possible.

I want to take a moment to extend my heartfelt thanks to Dr. Joseph R. Adams, Dr. Samuel Heppelmann, and Dr. Yu Zhang. Their assistance and valuable contributions to the analysis have been instrumental in the success of this endeavor, and I am deeply grateful for their support. In addition, I am thankful to all my fellow graduate students and colleagues from the STAR collaboration who have been a part of this journey. The stimulating discussions we have had together have been truly enriching, sparking new ideas and insights that have furthered our collective understanding of the subject.

The journey through my Ph.D. has not only been academically enriching but also filled with the warmth of friendship. I had the pleasure of meeting many exceptional individuals during this time, but the first friends I made played a vital role in helping me endure this long and challenging path. Carlos Sjogreen, Negin Alizadeh, Osakpolor Obakpolor, Arya Datta and Connor Cheek I owe you my deepest gratitude for being there for me when I needed support the most. Our close group made the entire experience more enjoyable and manageable, and I cherish the memories we created together.

As the process unfolded, I had the joy of forming lasting friendships with remarkable people with whom I shared living spaces. I want to express my thanks to Joaquin Grefa, who has become like a brother to me. Our bond has been a source of strength and companionship, making the

journey all the more delightful. And to Dennis Griffin, I am grateful for transforming our house into a brotherhood, and the camaraderie we shared filled my days with joy and laughter.

Last but certainly not least, I want to extend my deepest appreciation to my parents, Gonzalo and Emilia. Throughout my life, you both have unwaveringly believed in my potential and supported me with love and encouragement. Your constant motivation and vision for my future have been the driving force behind my accomplishments, and I am eternally grateful for all that you have done for me. I would like to express my heartfelt gratitude to my siblings Joshua Ball, Ricardo Ball, and Nikté Ball for their presence and support in my life.

In conclusion, my Ph.D. journey has been shaped by the remarkable support, understanding, and encouragement from numerous individuals who have touched my life in various ways. Each one of them has played an invaluable role in making this academic pursuit not only possible but also a fulfilling and enriching experience. I carry their influence and kindness with me as I venture into new horizons with a heart full of gratitude.

ABSTRACT

The Beam Energy Scan (BES) at the Relativistic Heavy Ion Collider (RHIC) aims at understanding the QCD phase diagram by using the most versatile detector in the world, the STAR detector. In the region where the chemical potential is finite, the transition from QGP matter to hadronic matter is less understood. Many models suggest the transition to be a first order phase transition, which requires the existence of a critical point. Fluctuations of conserved charge distributions have been used as a proxy to locate the critical point. Net-protons and net-kaons were used as proxies of net-baryon and net-strangeness, respectively. Results from net-proton C_4/C_2 showed a non-monotonic behavior as a function of collision energy representing a signature of the presence of the critical point. For the first Beam Energy Scan the results of net-lambda fluctuations were studied, but due to the lack of statistics higher order fluctuations were not calculated. The recent results of net-proton fluctuations at the lowest collision energy at RHIC motivated the study of the net-lambda fluctuations at the same energy. This dissertation reports the cumulants and correlation functions of the event-by-event lambda multiplicity distributions for the fixed-target physics run at $\sqrt{s_{NN}} = 3.0$ GeV Au+Au collisions up to the fourth order. The results are presented as a function of centrality and rapidity. The energy dependence is compared with previous results of net-lambda cumulant ratios up to the third order. Centrality and rapidity dependence of cumulants and correlation functions are compared with the transport model UrQMD and with Hadron Resonance Gas (HRG) calculations. Results indicate weak centrality dependence of the cumulant and correlation function ratios, except for more central collisions, where stronger deviations from the poissonian baseline are observed with increasing order of the ratios. In general, the results disagree from the observed behavior of net-proton cumulant ratios, implying relevance of the strangeness quantum number of lambda particles over the baryon quantum number at this energy. Cumulant ratios as a function of rapidity show suppression from the Poissonian baseline, implying the relevance of the local conservation of the strange quantum number at low collision energies.

Contents

DEDICATION **iii**

ACKNOWLEDGMENTS **iv**

ABSTRACT **vi**

LIST OF TABLES **ix**

LIST OF FIGURES **xii**

1 INTRODUCTION **1**
1.1 The Standard Model 1
1.2 Quantum Chromodynamics: QCD 3
  1.2.1 Color Confinement 4
  1.2.2 Asymptotic Freedom 4
  1.2.3 Screening and Antiscreening 7
1.3 The Quark Gluon Plasma(QGP) and the QCD Phase Diagram 10
1.4 Freeze-out Parameters 12
  1.4.1 Susceptibilities of Conserved Charges 13
  1.4.2 Connection Between Probability Functions and Susceptibilities 14
  1.4.3 Experimental Observables 17
1.5 Motivation 20

2 THE STAR EXPERIMENT **23**
2.1 The Relativistic Heavy-Ion Collider (RHIC) 23
2.2 The STAR Detector 24
  2.2.1 The Time Projection Chamber (TPC) Detector 24
  2.2.2 The Time of Flight (TOF) Detector 28
  2.2.3 The Beam-beam Counter (BBC) and the Event Plane Detector (EPD) 29
  2.2.4 The STAR Fixed-Target 30

3 DEFINITION OF IMPORTANT TERMS IN HEAVY ION COLLISIONS **32**
3.1 Kinematic of Heavy Ion Collisions 32
  3.1.1 Rapidity and Pseudo-rapidity 32
3.2 Geometry in Heavy Ion Collisions 35
  3.2.1 The Glauber Model 36
3.3 Reference Multiplicity 37
  3.3.1 Track Selection in the Reference Multiplicity 39
3.4 Centrality Bin Determination 40
  3.4.1 Inelastic Cross Section σ_{inel}^{NN} 40
  3.4.2 Particle Production Model 41

4 EVENT SELECTION AND LAMBDA RECONSTRUCTION **45**
4.1 Data Collection and Run Selection 45
4.2 Event Selection 46

4.3 Track Selection . . . 47
4.4 Lambda Reconstruction . . . 49
4.5 Purity of the V^0 Samples: . . . 53
4.6 Analysis Acceptance . . . 55
4.7 Net-lambda Distribution . . . 56

5 CUMULANTS AND CORRELATION FUNCTIONS 59
5.1 Moments and Cumulants . . . 59
5.2 Factorial Moments and Correlation Functions . . . 61

6 DETECTOR PERFORMANCE CORRECTIONS 63
6.0.1 Constant Efficiency Correction . . . 63
6.0.2 Multivariate Efficiency Bin Correction . . . 66
6.0.3 "Track-by-track" Efficiency Correction Method . . . 70
6.1 TPC Efficiency . . . 71
6.1.1 Embedding . . . 71
6.2 Lambda TPC Efficiency for Au + Au collisions at $\sqrt{s_{NN}} = 3.0$ GeV . . . 72
6.2.1 Rapidity Slice Fitting Procedure . . . 72
6.3 Methodology of the Efficiency Correction Applied to Cumulants . . . 75
6.4 Volume Fluctuation Effects . . . 77

7 ESTIMATION OF UNCERTAINTIES: 79
7.1 Statistical Uncertainty Estimation . . . 79
7.1.1 Delta Theorem . . . 79
7.1.2 Bootstrap Method . . . 81
7.2 Estimation of Systematic Uncertainties: . . . 82
7.2.1 Systematic Variations as a Function of $\langle N_{Part} \rangle$ . . . 84
7.2.2 Systematic Variations as a Function of Δy . . . 86

8 BASELINE AND MODEL COMPARISON 90
8.1 Poisson Baseline . . . 90
8.2 UrQMD Transport Model . . . 91
8.3 Hadron Resonance Gas Model . . . 91
8.3.1 Ideal HRG . . . 92
8.3.2 Quantum Van der Waals HRG . . . 93
8.3.3 Strangeness Canonical Ensemble HRG . . . 94

9 RESULTS AND DISCUSSION 95
9.1 Single Cumulants and Correlation Functions as a Function of Centrality . . . 95
9.2 Cumulant Ratios and Correlation Function Ratios as a Function of Centrality . . . 96
9.3 Cumulant Ratios and Correlation Function Ratios as a Function of Δy . . . 98
9.4 Comparison with Thermal Model Predictions . . . 101
9.5 Beam-energy Dependence of Net-lambda Cumulant ratios, C_2/C_1 and C_3/C_2 . . . 104

10 SUMMARY 108

BIBLIOGRAPHY 112

List of Tables

1 $FxtMult3$ centrality class 44

2 Purity of the V^0 candidates for different topological cut selections at $\sqrt{s_{NN}} = 3.0$ GeV, for centrality $0 - 60\%$ 56

3 Purity of the V^0 candidates for different centralities using cut set 3. 56

4 Track cuts used for the lambda reconstruction 57

5 Sources of the systematic uncertainty, their variations and the contribution for the systematic error. Relative contributions are calculated in the most central collisions($0 - 5\%$) of C_3/C_2 84

6 Parameters obtained from Thermal FIST [67] using preliminary particle yields at $\sqrt{s_{NN}} = 3.0$ GeV 103

List of Figures

1 Schematic representation of the classification of elementary particles in the Standard Model, taken from [4]. 2
2 Illustration of the total static quark potential as a function of the interquark separation. Figure from [9]. 5
3 Left: quantum fluctuation of an electron. Right: Photon exchange between two electrons. Figure from [7]. 7
4 Left: Quantum fluctuation involving the creation of a electron-positron pair. Right: Associated exchange process involving electron-positron pair. Figure from [7]. 8
5 Vacuum polarization corrections to gluon exchange in quark-quark scattering. Figure from [7]. 9
6 Measurements of α_s as a function of Q. The degree of QCD perturbation theory used in the calculation of α_s is shown in brackets (NLO: next-to-leading order; NNLO: next-to-next-to-leading order; NNLO+res.: NNLO matched to a resummed calculation; N3LO: next-to-NNLO). Figure from [11] 9
7 Schematic of the QCD Phase Diagram as a function of temperature (T) and baryochemical potential (μ_B). Figure from [21]. 11
8 Representation of a heavy ion collision between two ion beams. Figure from [25]. . . 13
9 Energy dependence of cumulant ratios (σ^2/M, $S\sigma$/Skellam and $\kappa\sigma^2$) of net-charge, net-kaon and net-proton multiplicity distributions in Au+Au collisions at $\sqrt{s_{NN}} = 7.7 - 200$ GeV [26]–[29] 18
10 a) Density plot of the quartic cumulant using the Ising mapping. b) Sketch of the energy dependence of the quartic cumulant. c) Possible scenario in which the critical contribution to kurtosis is large and negative. Figure taken from [19]. 19
11 Temperature (T) and baryochemical potential (μ_B) calculated at the chemical freeze-out using HRG model calculations with cumulant of net-kaon, net-proton, net-charge multiplicity distributions compared with thermal fits for measured particle yields [33]. 20
12 χ_4/χ_2 as a function of T for light and strange quarks in the continuum limit. LQCD data is compared to HRG calculations [34]. 21
13 Comparison between cumulant ratios C_2/C_1 and C_3/C_2 as functions of $\sqrt{s_{NN}}$ between net-lambda, net-proton, and net-kaon results [35]. 21
14 Overview of the Relativistic Heavy Ion Collider(RHIC) at Brookhaven National Laboratory(BNL). Figure taken from [37] 24
15 Schematic diagram of the STAR Detector showing the sub-detectors. Figure taken from [38]. 25
16 Schematic representation of the STAR detector in the fixed target mode. Figure from [39]. 25
17 A schematic of the TPC. Figure taken from [40]. 26
18 Energy loss in the TPC as a function of charge and momentum at $\sqrt{s_{NN}} = 3.0$ GeV. 28
19 Schematic of the location of TOF with respect to the TPC and VPD. Figure taken from [41]. 29
20 Schematic of the TOF detector. Figure from [42] 30
21 Schematic of the EPD. Figures shows the tiles in one ”wheel” of the EPD, it shows 372 tiles. Figure from [43]. 31

22 Fixed target apparatus including support beams, holding collar and gold foil. Figure from [39]. 31
23 Schematic representation of a heavy ion collision and the relation with the impact parameter and number of participants. Figure from [45]. 35
24 Illustration example of the total final state charge particle multiplicity N_{ch} distribution with Glauber-calculated quantities (b, N_{Part}). Figure from [47]. 38
25 Comparison between reference multiplicities in the collider mode (left panel) and the fixed target mode (right panel). 40
26 N_{coll} and N_{Part} distributions calculated from Glauber Monte Carlo events for different centralities. Figure from [39]. 41
27 Glauber Model+NBD fit on the $FxtMult3$ histogram. The lowest cut is at $N_{ch} = 4$, the upper cut is at $N_{ch} = 80$. Figure from [39]. 43
28 $\langle p_T \rangle$ averaged over the run as a function of the run index. Plot from Guannan Xie. . 46
29 v_z distribution peaked at $v_z = 200.7$ cm. Cut is applied $199.5 < v_z < 202$ 47
30 v_r distribution before and after cut. A cut on v_T about the beam spot $\langle v_{x,y} \rangle$ $(0, -2)$ cm is applied $v_T = 1.5$ cm 48
31 (a) $v_x - v_y$ distribution before cuts. (b)$v_x - v_y$ after all cuts. 49
32 Cross section of V^0 decay topology in x-y plane. 51
33 V_0 decay topology for strange particle decay used in the KFParticle method. P^+ refers to a positively charged particle (e.g., proton) and P^- refers to a negative charged particle (e.g., π^-). 52
34 Signal and background in the lambda invariant mass distribution using proton (p) and pion (π^-) pairs from $\sqrt{s_{NN}} = 3.0$ GeV Au+Au collisions. The green line shows the second-order polynomial fit to the background, the red line corresponds to the two summed Gaussian distribution fit on the background+signal. 54
35 Invariant mass distributions for 6 cut set variations from Table 2. 55
36 p_T and y of the lambda reconstruction. The red dashed line corresponds to the nominal cut boundary used in this analysis. 57
37 Event-by-event lambda multiplicity distribution for $\sqrt{s_{NN}} = 3.0$ GeV for three different centralities. Results are not corrected for reconstruction efficiency. 58
38 p_T dependence of reconstruction efficiency for $0-5\%$ central and $5-10\%$ central 200 GeV Au+Au collisions. Black vertical lines are the boundaries for three acceptance regions used in the corrections. Red horizontal line shows the equivalent p_T-averaged efficiency. Figure from [41]. 66
39 Toy simulation to test the multivariate efficiency bin correction. Figure from [56]. . . 70
40 Left panel: Generated lambda tracks for $0-5\%$ centrality. Right panel: Reconstructed tracks for $0-5\%$ centrality 72
41 2D efficiency map for lambda particles. 73
42 Plot of rapidity slices of TPC detector efficiency with exponential + 2nd order polynomial fits. Label on top of each sub-panel represents the rapidity slice in the y_{lambda}. 74
43 Comparison of proton TPC efficiency as a function of p_T for three centrality classes, integrated from $-0.9 < y < 0.1$. Figure from [39]. 75
44 Comparison of lambda TPC efficiency as a function of p_T for three centrality classes, integrated from $-0.9 < y < 0$. 76

45 Comparison between efficiency corrected and uncorrected cumulants: C_1, C_2, C_3 and C_4 as a function of average number of participant nucleons $\langle N_{Part} \rangle$. Results were corrected for CBWE. Only statistical errors are presented. 77
46 Comparison efficiency corrected and uncorrected cumulant ratios as a function of $\langle N_{Part} \rangle$. Results were corrected for CBWE. Only statistical errors are presented. . 78
47 Effect of cut parameter variations and efficiency variation on the efficiency corrected net-lambda *cumulant ratios* as a function of *centrality* at $\sqrt{s_{NN}} = 3.0$ GeV Au+Au collisions. 85
48 RMS values of *cumulant ratios* as a function of *centrality* at $\sqrt{s_{NN}} = 3.0$ GeV Au+Au collisions. 85
49 Effect of cut parameter variations and efficiency variation on the efficiency corrected net-lambda *correlation function ratios* as a function of *centrality* at $\sqrt{s_{NN}} = 3.0$ GeV Au+Au collisions. 86
50 RMS values of *correlation function ratios* as a function of centrality at $\sqrt{s_{NN}} = 3.0$ GeV Au+Au collisions. 87
51 Effect of cut parameter variations and efficiency variation on the efficiency corrected net-lambda cumulant ratios as a function of rapidity window at $\sqrt{s_{NN}} = 3.0$ GeV Au+Au collisions. 88
52 RMS values of cumulant ratios as a function of rapidity window at $\sqrt{s_{NN}} = 3.0$ GeV Au+Au collisions. 88
53 Effect of cut parameter variations and efficiency variation on the efficiency corrected net-lambda correlation function ratios as a function of rapidity window at $\sqrt{s_{NN}} = 3.0$ GeV Au+Au collisions. 89
54 RMS values of correlation function ratios as a function of rapidity window at $\sqrt{s_{NN}} = 3.0$ GeV Au+Au collisions. 89
55 Single cumulants as functions of centrality. 96
56 Correlation functions as functions of centrality. 97
57 Cumulant ratios as functions of centrality. 99
58 Correlation function ratios as functions of centrality. 100
59 Cumulant ratios as functions of rapidity window. 101
60 Correlation functions as functions of Δy. 102
61 Single cumulants as functions of rapidity window compared with thermal model calculations. 105
62 Cumulant ratios as functions of rapidity window compared with thermal model calculations. 106
63 Cumulant ratios (C_3/C_2 and C_2/C_1) as functions of center of mass energy. 107

1 Introduction

1.1 The Standard Model

The most successful model that describes elementary particles and their interactions from a theoretical point of view is the Standard Model of Particle Physics. The Standard Model of Particle describes three of the four fundamental forces in the Universe (electromagnetic, weak and strong) through a local SU(3)× SU(2)×U(1) gauge symmetry [1]. Its success relies on the experimental confirmation of the theoretical predictions, that started in 1969 at the SLAC accelerator at Stanford, where experiments were performed verify the theoretical work of James Bjorken [2].

The Standard Model is composed of fermions and bosons. The former represent the matter-generating elementary particles(leptons and quarks), while the latter correspond to the force carriers that mediate the interactions between fermions. Fermions are divided into leptons and quarks. There are six leptons(electron, muon, tau and their respective neutrinos) and there are six quarks (up, down, strange, charm, top, bottom). These particles are arranged based on their masses, charges and respective quantum numbers [3], which in the case of quarks and leptons are organized in families. A schematic representation of the elementary particles in the Standard Model is showed in Figure 1. Particles with spin = 1/2 that are in the same horizontal line have the same charge. Same "families" or "generations" are shown in vertical lines for the corresponding groups of quarks and leptons, that have identical properties except for their masses.

It is important to notice that all quarks have a baryon number of 1/3 and a quantum number called "color" and an "anticolor" for the antiquark. Leptons, on the other hand, do not carry a color charge. However, they have their own conserved quantum number called lepton number. All leptons shown in Figure 1 have lepton number 1, antileptons have lepton number -1. All other particles have lepton number 0. Additionally, every lepton family has its own quantum number: electron number (electron and electron-neutrino), muon number (muon and muon-neutrino) and tau number (tau and tau-neutrino).

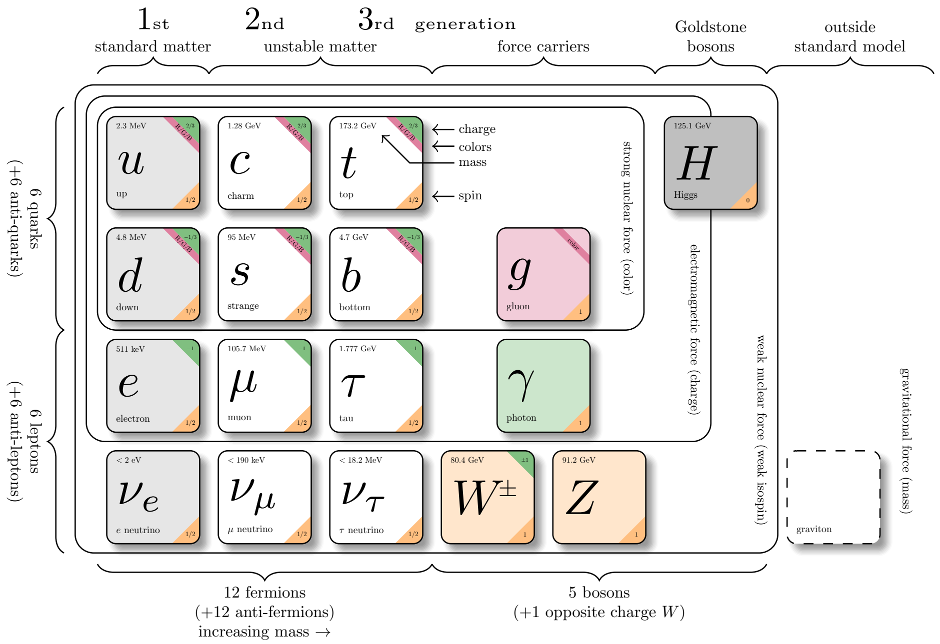

Figure 1: Schematic representation of the classification of elementary particles in the Standard Model, taken from [4].

The force carriers in the Standard Model are composed of gauge bosons (photon, gluon, Z boson and W$^{\pm}$ boson), which have a spin quantum number of 1. These spin 1 particles have masses heavier than the spin 1/2 particles (fermions). The gluon is the responsible for binding quarks into hadrons and hadrons into atomic nuclei. Gluons have a quantum number called “color”, which indicates any of the three colors (red, green, blue) and any of the anticolor charge. In total, there are 8 gluons instead of 9, this is due to the “white” gluon formed by a total color of zero. The $W^{\pm}$ and Z are the mediators of the weak nuclear force, the former are each other’s antiparticle, whereas the Z is its own antiparticle. The electromagnetic force is mediated by the photon, which is the responsible of interactions between electrically charged particles. The photon is its own antiparticle. The only particle with spin 2 is the graviton, which does not posses mass and it has not been observed directly. The graviton is its own antiparticle. Unlike the previously mentioned bosons, the massive Higgs boson has a spin of 0 and is a scalar boson, which interacts with mass and facilitates the generation of elementary particles [5], [6].

Generally, the strength of an interaction is proportional to the magnitude of the associated coupling constant, which are numerical coefficients that serve as parameters in an interaction. In the case of the electromagnetic interaction, the associated coupling constant is given by $\alpha_{em} = e^2/4\pi \approx 1/137$, where e is the coupling constant and α is the transition strength. In the case of the weak interactions, the associated quantity is $\alpha_w \approx 1/40$, which is about three times larger than α_{em}. For low energies, the effective coupling constant for weak interactions is lower than the electromagnetic one due to the non-zero $W^{\pm1}$ and Z masses. For the case of strong interactions, where the interactions are between colored elementary particles and also their bound states (such as protons and neutrons), the associated quantity is α_s and it is of the order of 1 and becomes smaller at higher energies this is due to the fact that gluons have color charge. The strong interaction is described by the Quantum Chromodynamics theory, which is described in the next Section 1.2.

1.2 Quantum Chromodynamics: QCD

QCD is similar to QED in a sense that both describe interactions mediated by a spin 1 boson. Theories of these types have a characteristic symmetry named gauge invariance. Gluons couple to the color charges, which leads to the fact that the different quark flavors must have identical strong interactions, because they exist in the same color states with the same possible values of color charges [7]. Another property of the strong interactions is that forces between quarks must be long range, this is due to the zero mass of gluons. On the other hand, the forces between hadrons are not long range, this is due to the zero colour total charge in hadrons. The forces between hadrons are residues of the forces between their quark constituents, which cancel when the hadrons are far apart. Even though both QCD and QED describe interactions which are mediated by massless spin 1 bosons, there is an important difference between them that affects the characteristics of the resulting force. This difference is originated by the fact that the photon that couples to the electromagnetic charge is itself neutral, while a gluon that couples to the color charge has a nonzero value. Just as quarks that exist in three color states, gluons can exist in 8 color states [7]. The implication of this gluon property is that gluons can couple with other gluons due to their nonzero color charge. This gluon-gluon interaction leads to the properties of the strong interactions, which are color confinement and asymptotic freedom.

1.2.1 Color Confinement

Contrary to leptons and electroweak gauge bosons, quarks and gluons cannot be observed as free particles. Instead, these particles bind to each other in order to compose a color neutral object, named hadrons, which are subdivided into two categories; baryons and mesons. Baryons are composed by three quarks states. In order to compose a color neutral object, each one of the three quarks must possess exclusively a red, green or blue color charge. Mesons are composed by a quark-antiquark pair, which requires for a quark to possess any of the three color charges, while the antiquark should match the corresponding anticolor charge. This feature of QCD is known as color confinement [8]. When separating the interacting quarks, the gluon field between them generates a string like flux, keeping a constant force per unit distance between them. In this context, it is more energetically favorable to create a pair of quark-antiquark rather than elongating the string-like flux between the quarks as they are separated.

In principle, bound states of two or more gluons can exist if the overall color charge is zero. These states are called glueballs. If they exist, it is expected that their electromagnetic interactions would be weaker compared to charged hadrons. Unfortunately, due to the limited understanding of confinement, precise theory calculations of the properties of glueballs are not possible [7].

1.2.2 Asymptotic Freedom

This property of QCD represents the weaker interaction that happens when distances between quarks are short distances, less than 0.1 fm, meaning that the contribution of the quark-quark scattering only relies on the lowest-order diagrams. As the distance between quarks increases, the interaction gets stronger and many higher-order diagrams have to be considered. At **short interquark distances** ($|r| \leq 0.1\text{fm}$), the interaction is dominated by one gluon exchange and it was shown that the potential is given by a Coulomb-like potential, which is analogous to the one-photon exchange in QED

$$V(r) = -\frac{4}{3}\frac{\alpha_s}{r} \quad (r \leq 0.1\text{fm}). \tag{1}$$

Here, α_s is the strong coupling constant, which represent the strength of the interaction. Due to asymptotic freedom, it is expected that α_s, decreases with decreasing r, but the variation of α_s at distances less than 0.1 fm is slight. At distances larger than 0.1 fm, the strength of the interaction increases rapidly and the contribution of one-gluon exchange no longer dominates. The potential in this region is given by:

$$V(r) \approx \lambda r \quad (r \geq 1\text{fm}), \tag{2}$$

where the constant λ is of the order of 1 GeVfm^{-1}. This potential is the representation of the confining potential between a quark-antiquark pair, which cannot be neglected even when the quark-antiquark pair is very far apart. Figure 2 shows an illustration of the total quark-antiquark potential as a function of the charge separation distance.

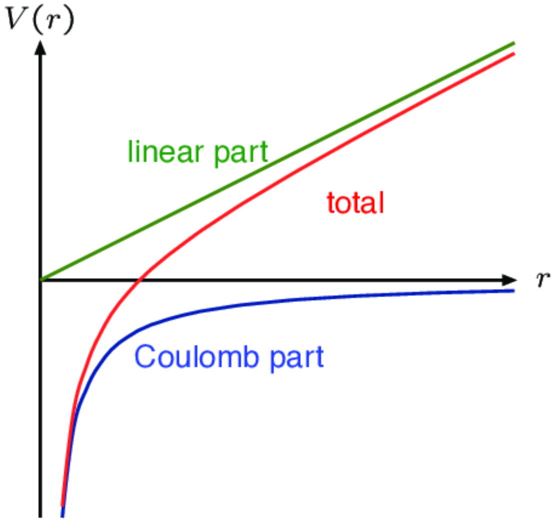

Figure 2: Illustration of the total static quark potential as a function of the interquark separation. Figure from [9].

As discussed previously, at short distances the interaction gets weaker. These short distance interactions are associated with large transfer of momentum $|\mathbf{q}|$ between particles, which is of the order of $1/r$, the distance at which the interaction occurs. One can think about the order of the momentum exchange by considering the amplitude for scattering from a spherical symmetric potential:

$$M(q) = 4\pi \int_0^\infty V(r) \frac{\sin(qr)}{qr} r^2 dr, \tag{3}$$

where one can observe that if r is small, the integrand is suppressed by the r^2 factor; for large r, the integrand is suppressed by the average of the oscillating sine factor. Therefore, the dominant contribution comes from values of r of the order of $1/q$. By considering a static spherical potential, we assume that the energy of the particle is unchanged. Energy of particles are unchanged in elastic scattering in the center of mass frame, in other reference frames or processes both energy and momentum can be exchanged between particles. In these cases, one has to consider that the strength of the interaction depends on $Q^2 \equiv |\mathbf{q}^2 - E_q^2|$, which is Lorentz-invariant. It can be shown that the QCD coupling constant (α_s) depends on Q^2 by using the fundamental fermion representation by the coupling-dependent function $\beta(g)$ as [10]

$$\beta(g) = -\frac{g^3}{(4\pi)^2} \left(\frac{11}{3} N - \frac{2}{3} n_f \right). \tag{4}$$

The overall minus sign displays the asymptotic freedom of any non-abelian gauge theory of SU(N) symmetry given by a small parameter n_f. By letting $\alpha_s = \frac{g^2}{4\pi}$, the QCD coupling constant, α_s at a given momentum Q^2 in terms of its value α at a different momentum scale Λ^2 is:

$$\alpha_s(Q^2) = \alpha \left[1 + \frac{\alpha}{4\pi} \left(\frac{11}{3} N - \frac{2}{3} n_f \right) \log(Q^2/\Lambda^2) \right]^{-1} \tag{5}$$

where $N = 3$, for the QCD case. n_f corresponds to the number of quark flavours (u,d,s,...). Equation (5) asymptotically approaches zero at large values of momentum scale, as discussed previously.

1.2.3 Screening and Antiscreening

A connection between asymptotic freedom and gluon self-interactions can be discussed qualitatively by using the example of screening in the context of QED. According to QED, when considering a one-photon exchange contribution to electron scattering, the electron emits and reabsorbs virtual photons always, independently of whether another electron is nearby. In the case that another electron is nearby, the second electron can absorb the photon before being reabsorbed by the original electron. Figure 3, show the corresponding processes, where the diagram on the left corresponds to the simplest **quantum fluctuation** process.

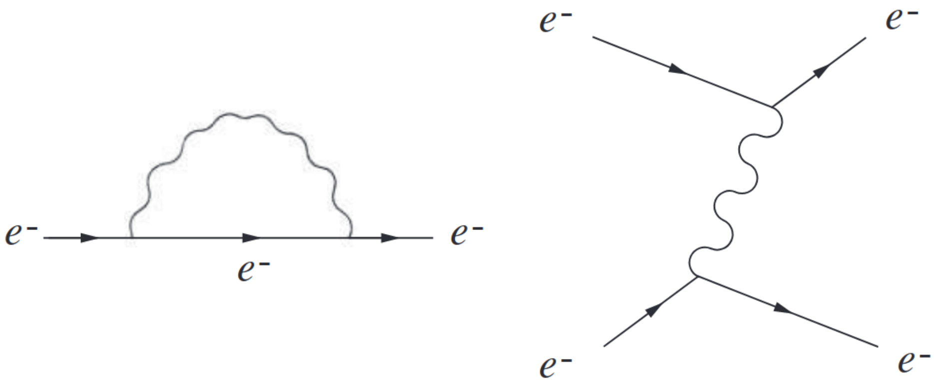

Figure 3: Left: quantum fluctuation of an electron. Right: Photon exchange between two electrons. Figure from [7].

Quantum fluctuations for electrons can also emit a photon that fluctuates into an electron-positron pair before it is reabsorbed by the initial electron, therefore the initial electron can indirectly reabsorb electron-positron pairs, as shown in Figure 4. These pairs produce polarization effects similar to the ones shown of charges immersed in a dielectric medium, where the effect of a positive charge inside the dielectric produces a **screening effect** that is perceived by a test charge. This screening changes the effective charge of the system (positive charge and dielectric) depending on the distance between the system and the test charge. A similar effect is observed in QED, which is related to the electron-positron pair produced by quantum fluctuations. If a second electron is close by, it can absorb the second photon before it is reabsorbed by the initial electron. The process is represented in the right diagram in Figure 4. This diagram contributes to the electron-electron interaction and for distances $r < 3.9 \times 10^{-13}$m the correction is of order α smaller than the Coulomb potential [7], from the diagram on the right panel of Figure 3. But as r decreases the effective potential increases, therefore the interaction strength increases at very short distances.

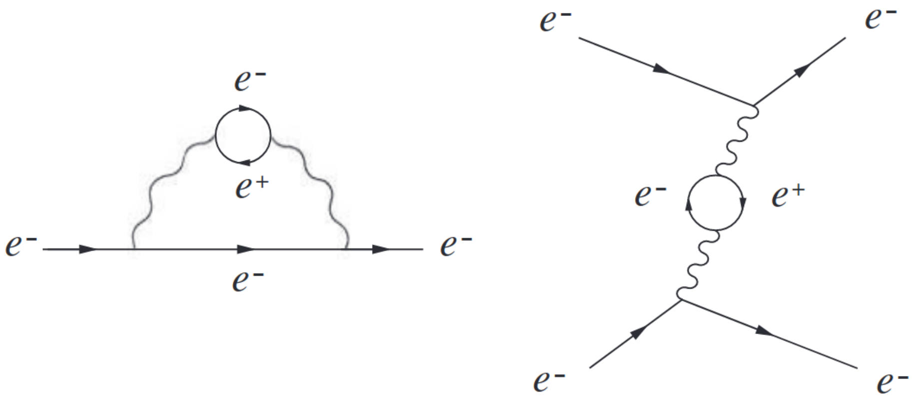

Figure 4: Left: Quantum fluctuation involving the creation of a electron-positron pair. Right: Associated exchange process involving electron-positron pair. Figure from [7].

Quantum fluctuations also exist in Quantum Chromodynamics(QCD), and also vary the interaction strength as a function of the distance. Similarly to the QED case, one can find that, due to quantum fluctuations in a quark-quark scattering, two lowest-order vacuum polarization corrections exist. These are shown in Figure 5, the diagram on the left leads to a screening correction, meaning that the interaction would grow stronger with shorter distances. On the other hand, the right diagram leads to an **antiscreening** effect, meaning that the interaction grows weaker at short distances. The net contribution of both effects results in a bigger contribution from the antiscreening effect at low distances, therefore the interaction grows weaker at short distances, which is a manifestation of asymptotic freedom.

Figure 6 shows the summary of measurements of α_s, as a function of the energy scale Q, where different perturbation orders in the calculations were used. The orders are shown in the legend

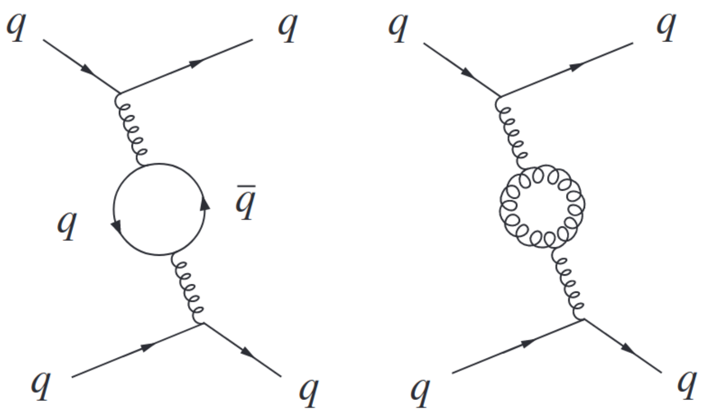

Figure 5: Vacuum polarization corrections to gluon exchange in quark-quark scattering. Figure from [7].

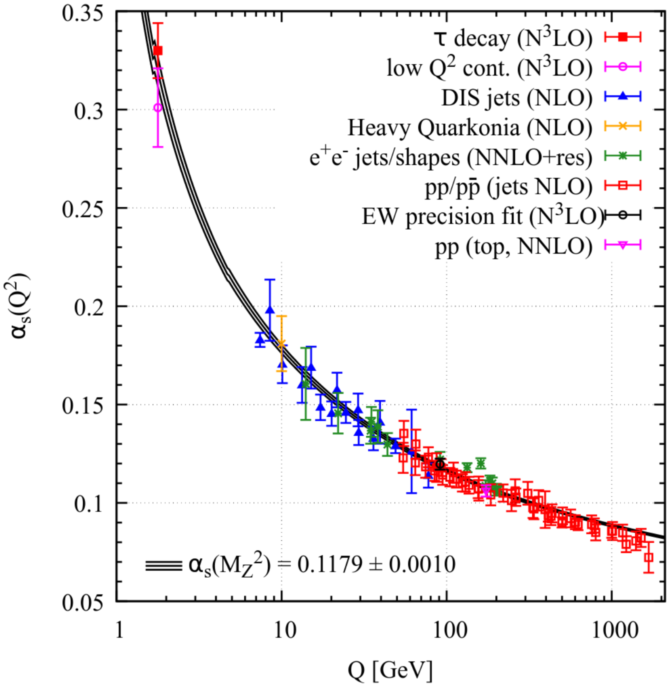

Figure 6: Measurements of α_s as a function of Q. The degree of QCD perturbation theory used in the calculation of α_s is shown in brackets (NLO: next-to-leading order; NNLO: next-to-next-to-leading order; NNLO+res.: NNLO matched to a resummed calculation; N3LO: next-to-NNLO). Figure from [11]

in enclosed parenthesis. The value of α_s decreases with increasing Q. In the high Q regime, perturbative methods are valid. For low values of Q, the best approach is Lattice QCD.

1.3 The Quark Gluon Plasma(QGP) and the QCD Phase Diagram

The properties of the strongly interacting matter are the focus of interest for this work, but most fundamentally is important in the understanding of the early universe, which some microseconds after the Big Bang was populated by strongly interacting matter made of quarks and gluons [12], [13]. In lattice QCD calculations of thermodynamics, it was shown that matter in thermal equilibrium has an energy density of 12.7 GeV/fm^3, which cannot be described as a collection of individual hadrons. This strongly interacting matter is coupled so that a collective medium can be formed and expands as a relativistic hydrodynamic fluid with low viscosity to entropy ratio $\eta/S \approx 1/4\pi$ [14], [15], with a flow time that can be shorter than 1 fm/c in the rest frame of the fluid. This form of matter was named **quark-gluon plasma (QGP)**. Therefore, at high temperatures and/or densities, the QCD matter can make a transition to a system of deconfined quarks and gluons, as a consequence of the asymptotic freedom. This transition of phases in QCD matter can be studied by varying the temperature and the baryochemical potential (μ_B), so that one can construct a **phase diagram of QCD matter**. The baryochemical potential (μ_B) can be understood as the net baryon density, meaning the total number of baryons minus the total number of antibaryons. From the work of [16], [17] it is known that Lattice QCD calculations of the pressure and energy density of hot QCD matter with the same amount of quarks and antiquarks predict that the transition is a continuous crossover, which agrees with cosmological observations [18]. In other words, a crossover transition from QGP to hadronic matter is expected to be found at $\mu_B \approx 0$, however the crossover transition is only observed for values very close to $\mu_B = 0$. As the value of μ_B is increased, the characteristics of the transition can change from smooth to discontinuous, also called a first order phase transition. The first order transition line should begin at a critical point [19], [20]. A sketch of the QCD phase diagram in the $T - \mu_B$ plane illustrating theoretical expectations is shown in Figure 7.

Apart from the QGP and hadron gas regions separated by the crossover and first order transitions, ordinary nuclear matter is shown for high values of μ_B and low values of T. By increasing

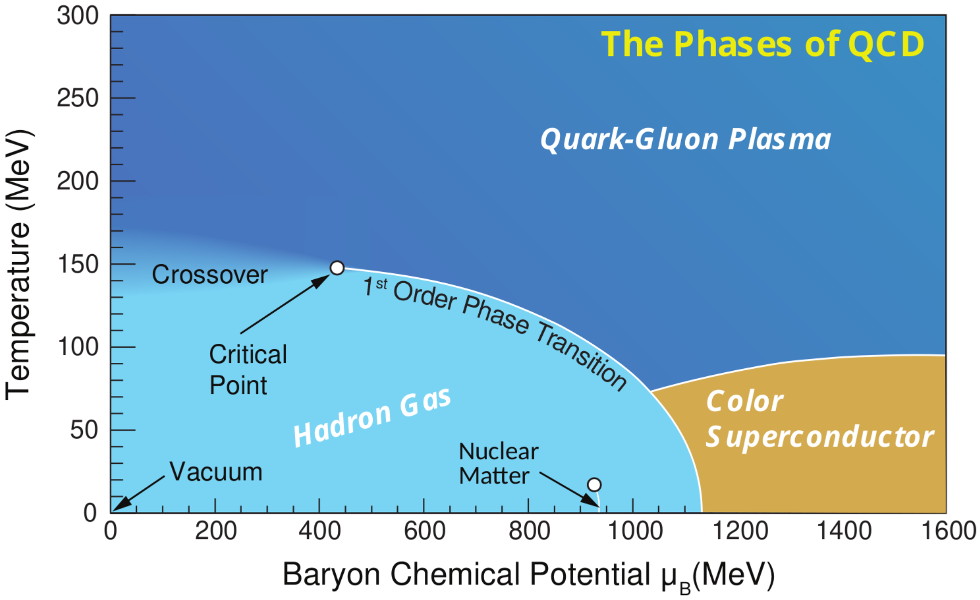

Figure 7: Schematic of the QCD Phase Diagram as a function of temperature (T) and baryochemical potential (μ_B). Figure from [21].

μ_B at these low temperatures one can reach a transition into a gaseous phase of degenerated neutrons, relevant to neutron stars [22], [23]. The most powerful method used to study the QCD phase diagram at $\mu_B = 0$ is first-principle lattice QCD. Due to the limitations of the method at $\mu_B \neq 0$, some extrapolation methods have been used, such as Taylor expansion method and the extrapolation from imaginary μ_B. The critical point is the point at which the first order phase transition line terminates. On the phase transition line, the two phases coexist and discontinuities are expected in conserved quantities. The coexisting of the two phases disappears when the phases become the same, this happens at the critical point, where, due to the increasing similarity of the phases as the system approaches the critical point, large fluctuations in conserved quantum numbers are expected. The search for the critical point is one of the most important objectives both for theorists and experimentalists in the nuclear physics field. On the experimental physics side, a way to study the QCD phase diagram is by using relativistic heavy ion colliders, which reproduce the first microseconds after the Big Bang, from QGP to its transition to hadronic matter. Experimentalists scan the QCD phase diagram by using the energy of the collision between the heavy ion beams, the scanning parameter used is the center-of-mass collision energy per nucleon pair ($\sqrt{s_{NN}}$), which affects the values of both T and μ_B. In general, when $\sqrt{s_{NN}}$ is larger than 100 GeV, one expects to find that the colliding nuclei traverse one another creating a high temperature and vanishing net-baryon density ($\mu_B \approx 0$). On the other hand, if the collision is not as energetic as the previous case, the colliding nuclei stop one another, creating a high temperature medium but with non-zero net baryon density ($\mu_B \neq 0$).

1.4 Freeze-out Parameters

In Relativistic Heavy Ion Collisions, the maximum energy density occurs just after the two Lorentz-contracted nuclei collide. The system at the beginning is out of equilibrium and it possesses an energy density which is far in excess of the typical energy density of a hadron (≈ 500 MeV fm^{-3}); this is at times 1 fm/c after the collision [24]. Therefore, the quarks and gluons created after the collision cannot be described as hadrons, instead they form strongly interacting QCD matter, the Quark Gluon Plasma. As the nuclei recede from each other and the QGP produced is expanding and cooling, new QGP is being created from the receding disk. After all possible QGP is created, the QGP expands in all directions and flows hydrodynamically until the systems cools down and reaches the energy density of an individual hadron, at which the system hadronizes into interacting hadrons and resonances. Hadrons and resonances interact inelastically until the system reaches a temperature, known as the **chemical freeze-out temperature** (T_{ch}). At this stage, the system is in equilibrium and all inelastic collisions cease, resulting in an unchanged number of hadron yields. The parameters that indicate this stage are called the **chemical freeze-out parameters**, which correspond to T_{ch} and μ_B. Hadrons can still interact elastically, until the system reaches a threshold temperature called the **kinetic freeze-out temperature** (T_{kin}). At this point, the transverse momentum (p_T) is fixed. The evolution of a heavy ion collision is represented in Figure 8.

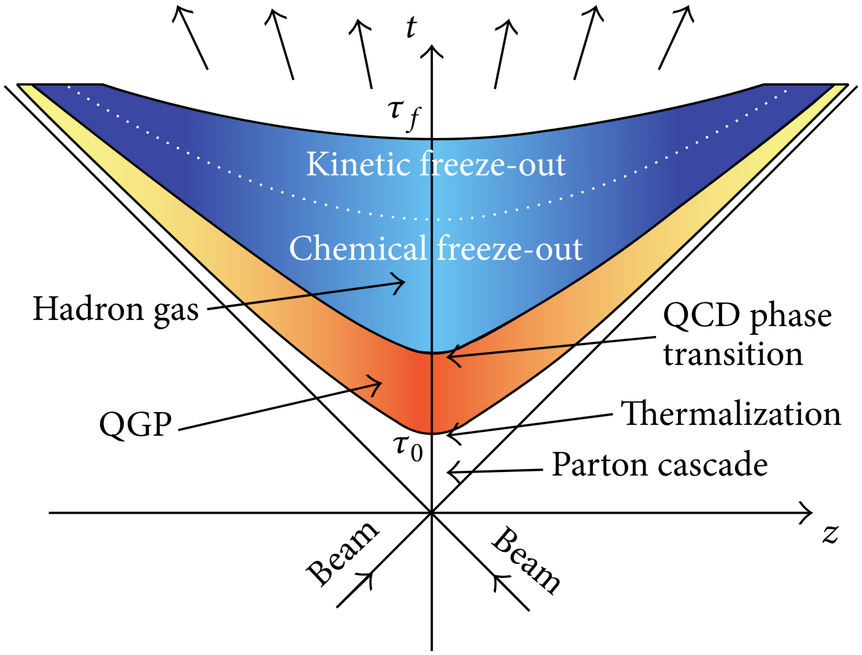

Figure 8: Representation of a heavy ion collision between two ion beams. Figure from [25].

1.4.1 Susceptibilities of Conserved Charges

As mentioned earlier, after the chemical freeze-out, hadrons go through many processes before reaching the detector but the signature of the transition from QGP to hadrons cannot be erased. Therefore, by studying the distributions and fluctuations of final state hadrons, one can learn about the properties of the medium and the transition. These observables are related to conservation of quantum numbers in heavy-ion collisions, which are: Net-charge(ΔQ), net-baryon number(ΔB) and net-strangeness(ΔS). If considered globally, these quantum numbers are conserved and should not fluctuate, but if they are considered in a reduced acceptance, fluctuations become relevant. The connection between fluctuations of hadronic distributions and theory can be understood by considering a system in thermal equilibrium in a Grand-Canonical Ensemble. One can use the partition function with Hamiltonian H, conserved charges Q_i and chemical potential μ_i for the respective conserved charge i. In heavy ion collisions the values of μ_i are fixed for each collision energy.

$$Z = \mathrm{tr}\left[\exp\left(-\frac{H - \sum_i \mu_i Q_i}{T}\right)\right]. \tag{6}$$

By taking derivatives of the natural logarithm of Eq. (6) with respect to the chemical potential (μ_i) one can construct the mean and the variance of the conserved charge Q_i as shown in Eq. (7) and Eq. (8), which are the central moments of the conserved charge:

$$\langle Q_i \rangle = T\frac{\partial}{\partial \mu_i} = T\frac{\partial}{\partial \mu_i}\mathrm{ln}Z \tag{7}$$

$$\langle (\delta Q_i)^2 \rangle = T^2\frac{\partial^2}{\partial (\mu_i)^2}\mathrm{ln}Z \tag{8}$$

where $\delta Q_i = Q_i - \langle Q_i \rangle$. One can also define the thermodynamic susceptibilities χ_n^i of conserved charges, where n represents the order of the derivative. The thermodynamic susceptibilities measure the response of the thermodynamic variable to an infinitesimal change in the chemical potential μ_i,

$$\chi_n^i = \frac{\partial^n (p/T^4)}{\partial (\mu_i/T)^n}. \tag{9}$$

Where p is the pressure of the system calculated from the partition function (Z). One can also have susceptibilities that measure the infinitesimal change due to two or more chemical potentials; they characterize correlations between conserved charge Q_l, Q_m, etc.

$$\chi_{ijk}^{lmn} = \frac{\partial^{i+j+k}(p/T^4)}{\partial (\mu_l/T)^i \partial (\mu_m/T)^j \partial (\mu_n/T)^k} \tag{10}$$

One can relate the previous susceptibilities with moments of probability functions, as shown in the next subsection.

1.4.2 Connection Between Probability Functions and Susceptibilities

Consider a real-valued function $F(x)$ that satisfies the following conditions:

1. $F(x)$ is monotonically increasing or constant .
2. $F(x)$ is continuous everywhere for positive values of x.

3. $F(-\infty) = 0$ and $F(+\infty) = 1$

If $F(x)$ satisfies these conditions, it is called a cumulative distribution function, which represents the probability of the event $X \leq x$, where X is a random variable,

$$Pr\{X < x\} = F(x). \tag{11}$$

For a continuous $F(x)$ one can write:

$$F(x) = \int_{-\infty}^{x} f(t)dt, \tag{12}$$

where $f(t)$ is denoted as the probability distribution density, which can be used to calculate the $n - th$ statistical moments of $F(x)$ about the origin:

$$\mu'_n = \int_{-\infty}^{\infty} x^n f(x)dx. \tag{13}$$

where the first moment is the mean (M):

$$M = \mu'_1 = \int_{-\infty}^{\infty} xf(x)dx. \tag{14}$$

For higher order moments, central moments are rather used; this is done in order to provide better information of the shape of the distribution:

$$\mu_n = \int_{-\infty}^{\infty} (x - M)^n f(x)dx. \tag{15}$$

Particularly, the variance is defined as:

$$\sigma^2 = \int_{-\infty}^{\infty} (x - M)^2 f(x)dx. \tag{16}$$

The variance can be used to defined normalized moments, in particular, the normalized third central moment (S) provides information about how skewed the distribution is, meaning how asymmetric the distribution is. A value of zero represents a symmetric distribution, a negative value corresponds to a distribution skewed to the left and a positive value to a distribution skewed to the right,

$$S = \frac{\mu_3}{\sigma^3}. \tag{17}$$

The normalized fourth central moment can also be defined (κ). κ is named kurtosis and it measures the heaviness of the tail of the distribution, compared to the normal distribution with the same σ^2.

$$\kappa = \frac{\mu_4}{\sigma^4} - 3 \tag{18}$$

Large values of κ represent heavy tails in the distribution while small values of κ correspond to light-tailed distributions. For values of $S = 0$ and $\kappa = 0$, the distribution is defined as a Gaussian distribution. An alternate quantity to the moments are the cumulants of the distribution C_n, which are mostly used in this work. The cumulants of a random variable are defined using the cumulant generating function, given by:

$$\ln(\Phi(t)) = \sum_{n=0}^{\infty} C_n \frac{t^n}{n!} \tag{19}$$

where $\Phi(t)$ is the moment generating function defined as:

$$\mu'_n = \frac{d^n}{dt^n}\Phi(t)_{t=0}. \tag{20}$$

It can be shown that cumulants and moments are related as:

$$\frac{C_1}{C_2} = \frac{M}{\sigma^2} \qquad \frac{C_3}{C_2} = S\sigma^2 \qquad \frac{C_4}{C_2} = \kappa\sigma^2 \tag{21}$$

From a statistical physics perspective, an extensive quantity in a large system can be thought of as a sum of the energies associated with a number of nearly independent regions. By looking at Eq. (9), one can observe that in order to construct the different orders of the susceptibilities, derivates of the pressure are calculated, therefore we can identify the pressure with the cumulant generating function:

$$p = -T \times \ln(\exp[-(E + \mu_i Q_i)/T]). \tag{22}$$

One can relate the susceptibilities with the central moments and therefore with the cumulants.

$$\frac{\chi_2}{\chi_1} = \frac{\sigma^2}{M} = \frac{C_2}{C_1} \tag{23}$$

$$\frac{\chi_3}{\chi_2} = S\sigma = \frac{C_3}{C_2} \tag{24}$$

$$\frac{\chi_4}{\chi_2} = \kappa\sigma^2 = \frac{C_4}{C_2} \tag{25}$$

1.4.3 Experimental Observables

As mentioned previously, fluctuations of hadronic multiplicity distributions can probe the nature of strongly interacting matter. Experimentally, one can measure in a heavy ion collisions the event-by-event particle multiplicity distributions of conserved quantities. Unfortunately, the actual measure of a conserved quantum number is not possible, instead proxies of those quantities are used. Fluctuations in net-protons are used as a proxy of net-baryon quantum number, net-kaons are used as a proxy for net-strangeness. Fluctuations of the mentioned proxies have been calculated and studied as functions of $\sqrt{s_{NN}}$ from the STAR Collaboration, the results are shown in Figure 9, where Skellam corresponds to the value of $S\sigma$ from a Skellam distribution, which is the difference between two independent random variables.

It can be observed that the behavior of $\kappa\sigma^2$ for net-protons shows a non-monotonic energy dependence for most central collisions. The non-monotonicity in net-baryon $\kappa\sigma^2$ is predicted to be

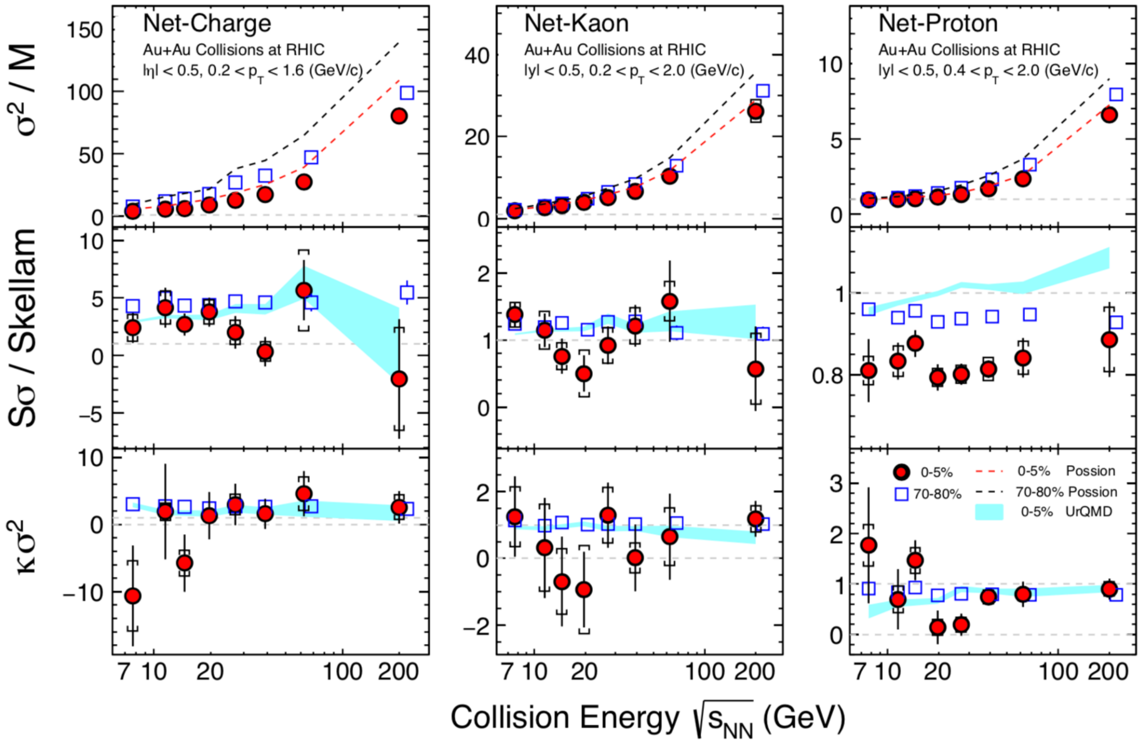

Figure 9: Energy dependence of cumulant ratios (σ^2/M, $S\sigma$/Skellam and $\kappa\sigma^2$) of net-charge, net-kaon and net-proton multiplicity distributions in Au+Au collisions at $\sqrt{s_{NN}} = 7.7 - 200$ GeV [26]–[29]

a signature of the QCD critical point from the sigma model [30]–[32], which is due to the fact that higher-order moments of conserved quantities are more sensitive to the correlation length (ξ). For instance, $\langle(\delta N)^3\rangle \sim \xi^{4.5}$ and $\langle(\delta N)^4\rangle - 3\,\langle(\delta N)^2\rangle \sim \xi^7$. Figure 10 shows the predicted value of the quartic cumulant of net-proton multiplicity fluctuation [19] using a mapping to Ising model, with the same universality class.

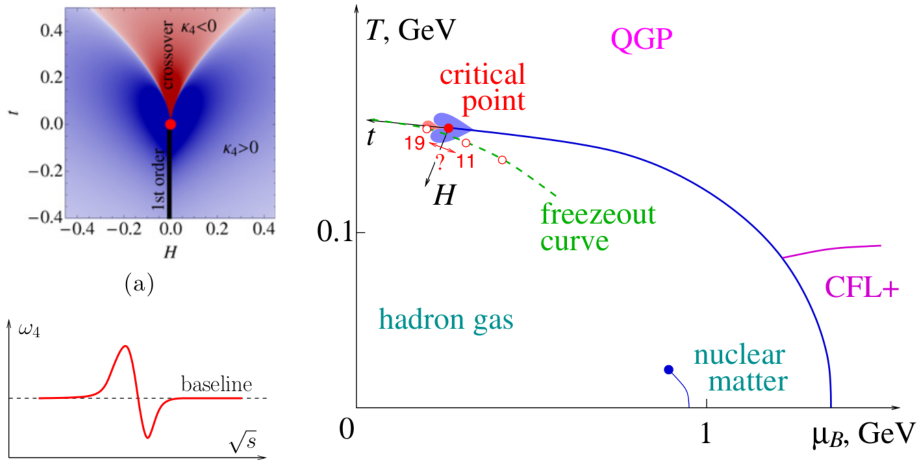

(a)

(b)

(c)

Figure 10: a) Density plot of the quartic cumulant using the Ising mapping. b) Sketch of the energy dependence of the quartic cumulant. c) Possible scenario in which the critical contribution to kurtosis is large and negative. Figure taken from [19].

Results from net-kaons, net-proton and net-charge were used to predict sequential hadronization and compared with HRG model using particle yields were the freeze-out parameters were extracted and compared. Figure 11, show the obtained freeze-out parameters (T and μ_B), the results show that for both the Hadron Resonance Gas (HRG) model and thermal fits, the freeze-out parameters follow different values for different particle species, specifically the difference is attributed to the presence of strange quarks compared to hadrons with light-quark content, which indicates a quark mass dependence in the process of hadronization.

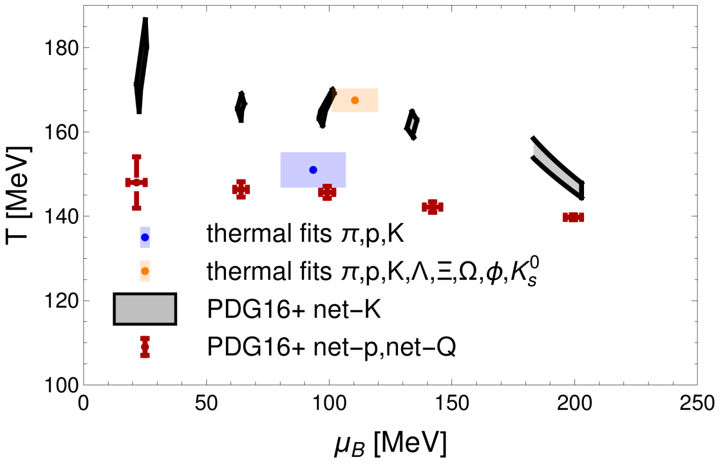

Figure 11: Temperature (T) and baryochemical potential (μ_B) calculated at the chemical freeze-out using HRG model calculations with cumulant of net-kaon, net-proton, net-charge multiplicity distributions compared with thermal fits for measured particle yields [33].

1.5 Motivation

Net-proton and net-kaon fluctuations have been used as proxies of net-baryon and net-strangeness to study the properties of the QCD phase boundary. However, as it was shown in Figure 11, the dependence on the quark content of hadrons can change the values of the freeze-out parameters. It was proposed from lattice QCD calculations compared with HRG model that the temperature separation at $\mu_B = 0$ is due to the flavor dependence of quarks in hadrons [34]. Figure 12 shows the susceptibility ratios for strange and light quarks from LQCD and HRG.

The inital motivation of the lambda fluctuation analyses was to provide a new measurement of the net-strangeness fluctuations, since only net-kaons do not provide the complete measurement of net-strangeness in a heavy ion collision. Furthermore, studying the lambda particles in a context of quark mass dependence can help to understand which of the conserved quantum numbers for lambda (Strangeness and Baryon quantum number) play a prominent role at hadronization. For the first Beam Energy Scan (BES) at the Relavitistic Heavy Ion Collider (RHIC), results of the event-by-event lambda multiplicity distributions were obtained [35] and the cumulants were calculated as a function of $\sqrt{s_{NN}}$. The results were compared with the results for proton and kaon fluctuations

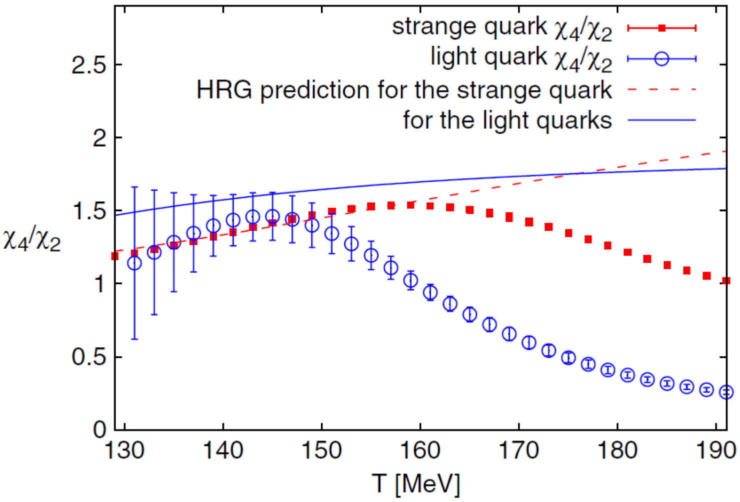

Figure 12: χ_4/χ_2 as a function of T for light and strange quarks in the continuum limit. LQCD data is compared to HRG calculations [34].

as shown in Figure 13. The results show that cumulant ratios of lambda show close values to the ones of proton.

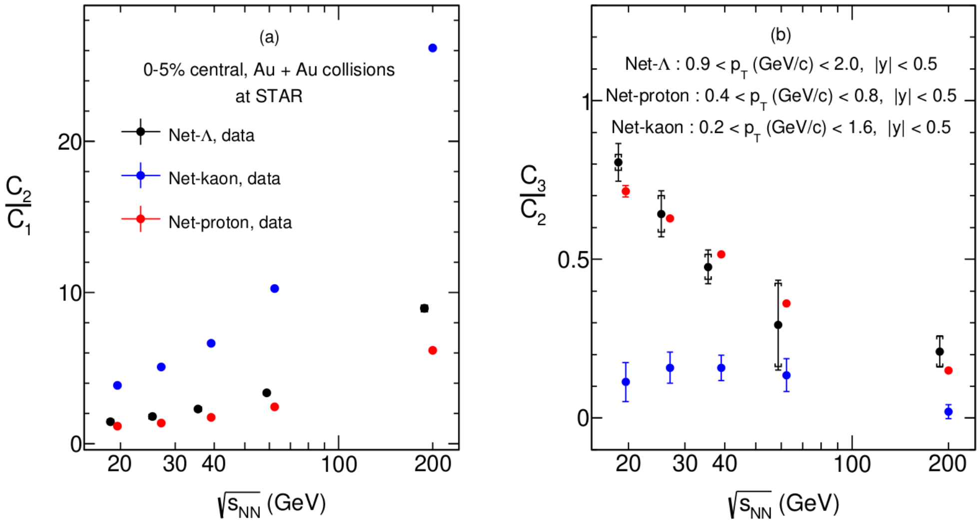

Figure 13: Comparison between cumulant ratios C_2/C_1 and C_3/C_2 as functions of $\sqrt{s_{NN}}$ between net-lambda, net-proton, and net-kaon results [35].

As mentioned previously, the net-proton C_4/C_2 cumulant ratio as a function of $\sqrt{s_{NN}}$ is the best proxy in the search of the critical point. The close behavior of cumulant ratios C_2/C_1 and C_3/C_2 of net-lambda rises questions about the sensitivity of the C_4/C_2 of net-lambda close to the critical point. Unfortunately, due to the low statistics, the cumulant ratio C_4/C_2 could not be calculated with precision. Therefore, with the increased statistics and extended range of $\sqrt{s_{NN}}$ obtained for the second BES at RHIC, we were able to continue with the comparison with protons up to C_4/C_2 and also study the behavior of lambda fluctuations at the lowest $\sqrt{s_{NN}}$ at RHIC.

2 The STAR Experiment

2.1 The Relativistic Heavy-Ion Collider (RHIC)

RHIC is the first machine in the world capable of colliding heavy ions at close to the speed of light. The collider was built at Brookhaven National Laboratory (BNL), located at Upton, NY, US [36]. RHIC collides two beams of ions/protons head-on, the beams travel inside rings in opposite directions at relativistic speed, the rings are cooled to temperatures of few Kelvin in order to use superconducting magnets. These two rings, named "Blue" and "Yellow", are nearly 2.5 miles of circumference, making for a total of 5 miles of superconducting, supercooled rings. RHIC accelerates heavy ions up to a top energy of 200 GeV per nucleon. After the collisions, a large number of particles are created and are measured by detectors around the circumference. There are six intersection points and four different detectors (STAR, PHENIX, BRAHMS and PHOBOS) located at four of the intersection points. The data used for the present work was collected by the STAR detector, which is located in the 6 o'clock position of the RHIC ring and is the only detector that is still operating.

Figure 14 shows an aerial view of the RHIC facility at BNL. The yellow ring carries particles in the counter-clockwise-direction, while the blue ring carries particles in the clockwise direction.

In order to accelerate beams around RHIC, the beams have to be fed by other accelerators in order to gradually ramp up the ions to sufficient energies. The beam starts either from the Electron Beam Ion Source (EBIS) as a source of heavy ions or from the Linear Accelerator (Linac) as a source of protons, these are shown in purple and red respectively in Figure 14. Further on, the beam is accelerated by the Booster Synchotron, shown in light blue, before passing into the Alternating Gradient Synchotron (AGS), shown in green. In collider conditions, the ions are piped in both beams of the RHIC ring. Specifically, for this work, only one beam of 3.85 GeV was required (yellow beam) for the 2018 fixed-target run. At low energies $\sqrt{s_{NN}} < 7\text{GeV/c}$, the beams become

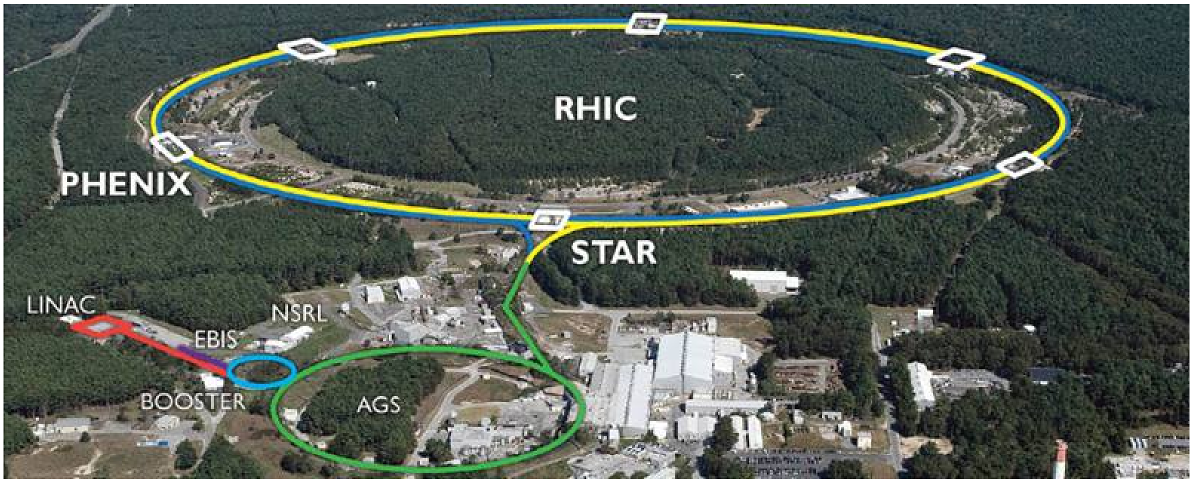

Figure 14: Overview of the Relativistic Heavy Ion Collider(RHIC) at Brookhaven National Laboratory(BNL). Figure taken from [37]

diffuse and difficult to collide at high rates, which limits the lowest $\sqrt{s_{NN}}$ in the collider mode. The fixed-target configuration extends the energy range to $\sqrt{s_{NN}} = 3.0$ GeV, which is the energy used in this work, which corresponds to a 3.85 GeV beam on a fixed-target.

2.2 The STAR Detector

The Solenoid Tracker at RHIC (STAR) is composed of many sub-detectors for specific purposes. Some of the most important detectors are; the Time Projection Chamber (TPC), Time of Flight (TOF), Event Plane Detector (EPD). The TPC can be used to track tracing of charged particles, measure momentum and identify charged particles at low transverse momentum range. TOF identifies charged particles at high transverse momentum range, and EPD measures the event plane for flow and polarization measurements. Schematic representations of the STAR detector are shown in Figs. 15 and 16.

2.2.1 The Time Projection Chamber (TPC) Detector

The TPC is usually referred to as the “heart” of the STAR detector, it is the main tracking detector at STAR, used to track charged particles. It has a large acceptance with pseudo-rapidity of $-1 < \eta < 1$ and full azimuthal coverage ($0 < \phi < 2\pi$). The identification capability of the

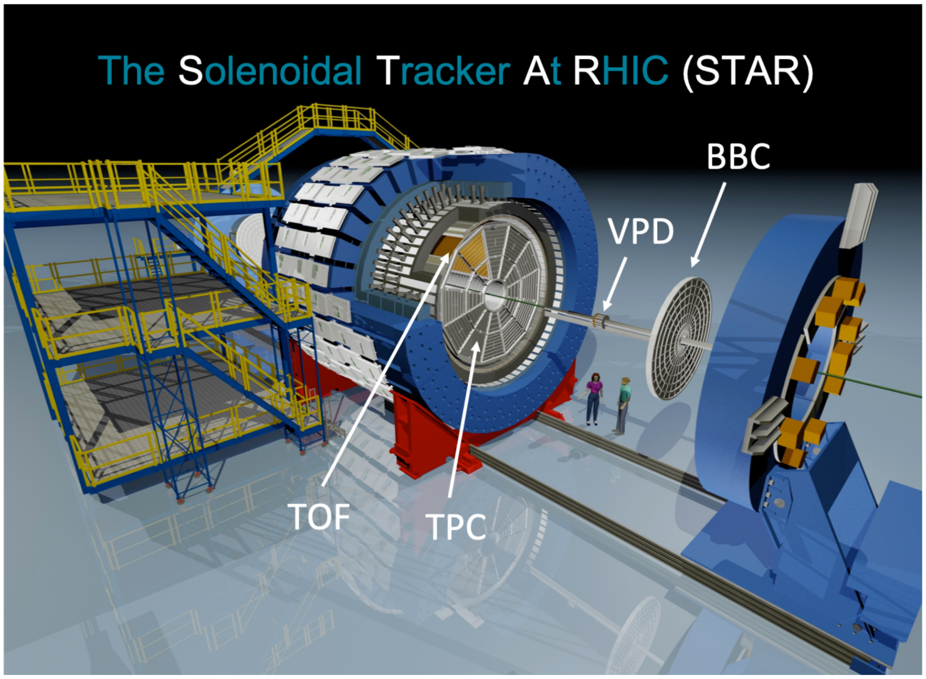

Figure 15: Schematic diagram of the STAR Detector showing the sub-detectors. Figure taken from [38].

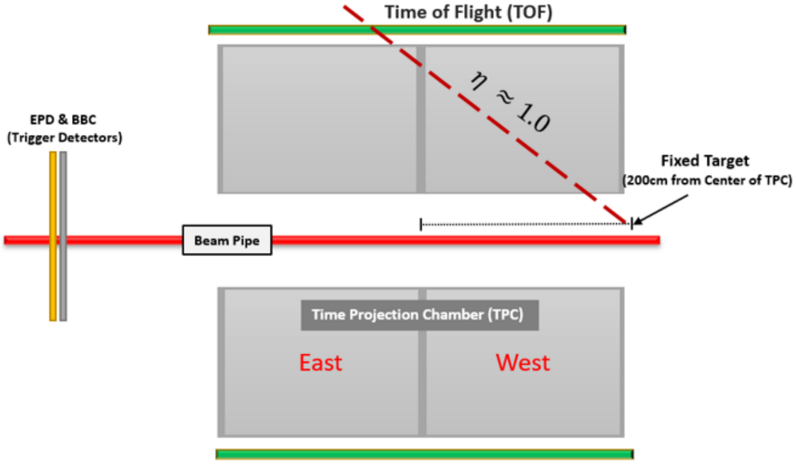

Figure 16: Schematic representation of the STAR detector in the fixed target mode. Figure from [39].

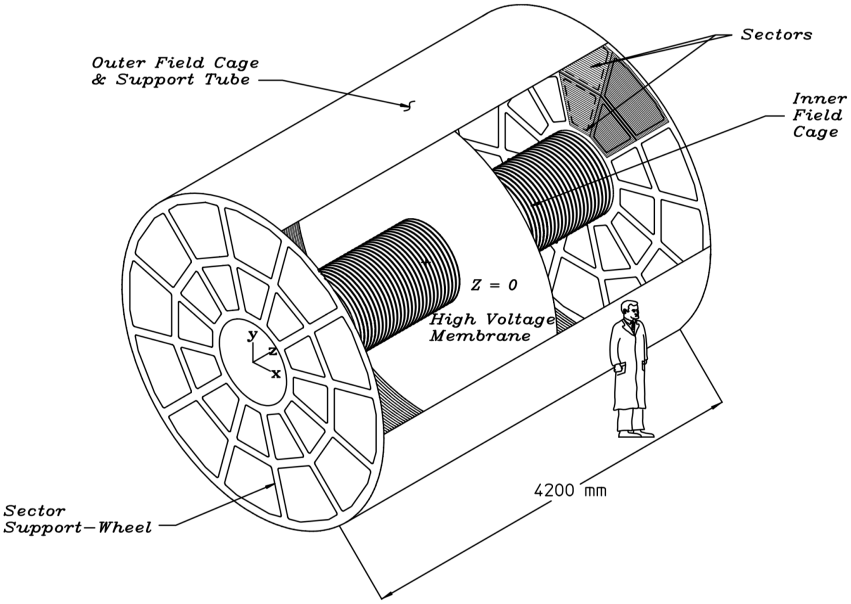

Figure 17: A schematic of the TPC. Figure taken from [40].

TPC ranges from 100 MeV/c to 1 GeV/c in transverse momentum for protons and transverse momentum of charged particles can be measured over a range of 100 MeV/c to 30 GeV/c. The TPC is a cylinder with dimensions of 4 m of diameter and 4.2 m of length (from $z = -210$ cm to $z = 210$ cm). The inner field cage is 50 cm from the center of the beam pipe and the outer field cage is 200 cm from the center of the beam pipe. The central membrane (CM) is located at the center of the TPC ($z = 0$) and operates at a voltage of 28 kV; a schematic representation of the TPC is shown in Figure 17.

A strong magnetic field of about 0.5 T is produced inside the detector parallel to the beam direction, the charged particles produced after the collision of the beams travel radially outwards at high speed; due to the effect of the magnetic field and electric field, the charged particles create helices. In order to gain information about the trajectory of the charged particles, the TPC is filled with P10 gas (10% methane CH_4 and 90% argon Ar) and a uniform electric field of $|E| = 135$ V/cm. The uniform electric field of the TPC is generated by the central membrane (CM), the outer field cage, the inner field cage and the end caps. The collisions take place near the center of the TPC. When the charged particles traverse the TPC, they will interact with the gas. The secondary electrons released by the ionized gas atoms will drift to the readout end caps at the bottom of the TPC under the uniform electric field, and the track of particles will be reconstructed with high resolution. The drift velocity of the gas in the TPC is typically 5.45 cm/μs. The readout system is based on Multi-Wire Proportional Chambers (MWPC) with readout pads. Consider that the initial primary vertex is at the center of the TPC, the reconstruction of the track starts from the outermost hit point and then is projected inward. The hit points in the pad rows are used to reconstruct the track, which is known as the global track. The global tracks are used to fit the primary interaction vertex by using at least ten hits. The primary vertex is found by considering all of the tracks reconstructed in the TPC and then extrapolating them back to the origin. The global average is the vertex position. For each global track, the closest distance to the primary vertex is called the distance of closest approach (DCA). The global tracks refitted with DCA < 3 cm including the primary vertex are the primary tracks. The TPC is also used to measure the particle energy loss(dE/dx) as it passes through the ionized gas as a function of momentum ($\vec{p}$). The energy loss for a given particle momentum is well know, however due to finite resolution the measured energy loss has non-zero thickness. The ionized energy loss (dE/dx) is calculated by using the Bethe-Bloch equation, that gives the mean rate of energy loss for a charged particle, shown in Eq. (26):

$$-\langle\frac{dE}{dx}\rangle = 2\pi N a r_e^2 m_e c^2 \rho \frac{Z}{A}\frac{z^2}{\beta^2}\left[\ln\left(\frac{2m_e\gamma^2 v^2 W_{max}}{I}\right) - 2\beta^2\right] \tag{26}$$

where $2\pi N_a r_e^2 m_e c^2 = 0.1535$ MeVcm^2/g and $\gamma = 1/\sqrt{1-(v/c)^2}$.

m_e : electron mass.

I: mean excitation potential.

ρ: density of absorbing material.

r_e: classical electron radius.

N_a: Avogadro's number.

W_{max}: maximum energy transfer in a single collision.

z: charge of incident particle in units of e.

Z: atomic number of absorbing material.

A: atomic weight of absorbing material.

The energy transfer is parameterized using the momentum transfer due to the fact that it is a measurable quantity. The identification of particles is achieved to first order by selecting tracks with values dE/dx close to the predicted value. At large $\sqrt{s_{NN}}$ and large values of momenta, $|\vec{p}| > 1.5 - 2$ GeV/c, the bands for different particles start to merge and particle identification becomes difficult. In order to identify particles in the high momentum range, the Time of Flight detector is used. Figure 18 shows the energy loss in the TPC as a function of particle charge and momentum.

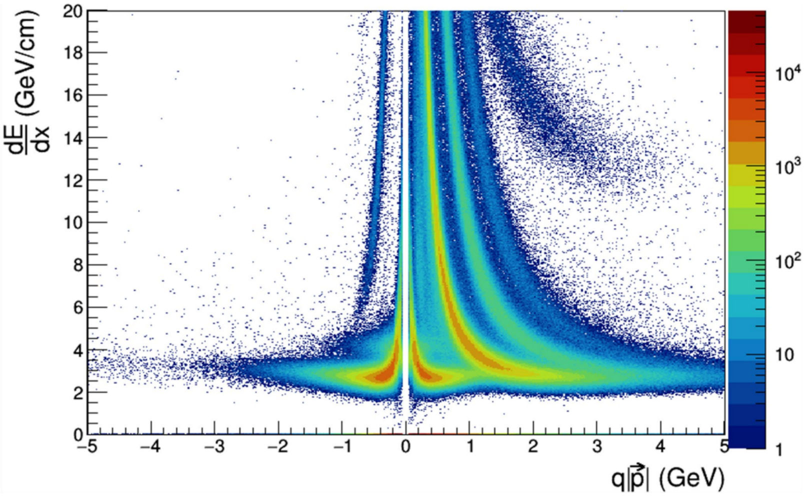

Figure 18: Energy loss in the TPC as a function of charge and momentum at $\sqrt{s_{NN}} = 3.0$ GeV.

2.2.2 The Time of Flight (TOF) Detector

In order to have better momentum coverage in the particle identification, the TOF is used. TOF is a cylindrical detector that wraps around the TPC, it basically measures the time at which particles exit the TPC, it is composed of stacks of thin glass plates separated by less than a quarter of a milimeter of gas, with high-voltage electrodes on the top and bottom of the stacks creating an electric field perpendicular to the plates. There are 120 trays mounted on the east and west sides of the TPC (60 on each side), with pseudorapidity coverage $-1 < \eta < 1$ and full azimuthal angles. Every TOF tray consists of 32 Multi-gap Resistive Plate Chamber (MRPC) modules. When the charged particles pass through the MRPC module, they produce an avalanche of electrons; the signal is the superposition of all avalanches in the gas gaps. The voltage drops created by these avalanches are measured by pads outside the electrodes and the time is recorded. In order to identify the particle, the mass is calculated by using Eq.(27) and Eq.(28).

$$\beta = \frac{v}{c} = \frac{L}{c\Delta t} \tag{27}$$

$$m^2 = p^2(1/\beta^2 - 1) \tag{28}$$

where $\beta = p/E$ and $E = \sqrt{p^2 + m^2}$, p is the momentum of the particles measured by the TPC and Δt is the difference between the start time measured by TOF and the stop time measured by VPD. A schematic of the location of TOF with respect to the TPC is shown in Figure 19. Figure 20 shows the basic setup of the TOF detector.

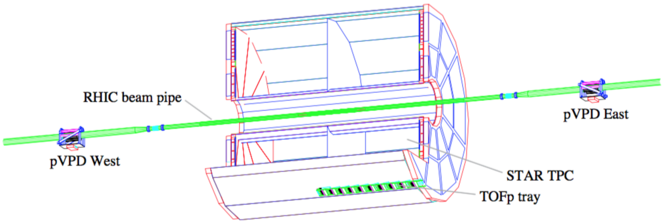

Figure 19: Schematic of the location of TOF with respect to the TPC and VPD. Figure taken from [41].

2.2.3 The Beam-beam Counter (BBC) and the Event Plane Detector (EPD)

The EPD and BBC are sets of forward/backward detectors. The BBC are scintillating tiles paired with photo-multiplier tubes with rapidity coverage of $3.4 < |\eta| < 5.0$. The EPD is a pair of disks consisting of plastic scintillator tiles embedded with wavelength-shifting fibers. Charged particles

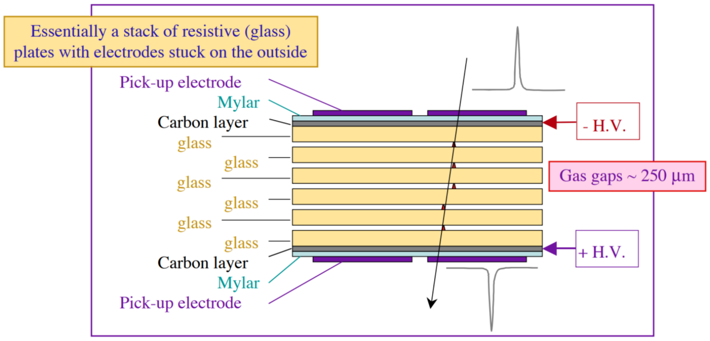

Figure 20: Schematic of the TOF detector. Figure from [42]

passing through the scintillator produce photons that are absorbed by the wavelength-shifting fibers and transmitted through clear fiber optics to Silicon Photomultipliers (SiPMs). These SiPMs are a stack of high- voltage electrodes that produce electron avalanches whenever photons are absorbed. Drops in potentials across the electrodes thus correspond to particles passing through a certain region in η and ϕ. The EPD is a detector used primarily to measure the event plane for flow and polarization measurements. It covers a pseudorapidity of $2.1 < |\eta| < 5.1$. In this analysis, the East BBC and EPD are used as the minimum bias trigger detector. Collisions are triggered and recorded if they include a hit in the East BBC or EPD and a hit in the TOF detector. A schematic of the EPD is shown in Figure 21.

2.2.4 The STAR Fixed-Target

The first test of the STAR fixed-target program was in 2015, with two data sets of Au+Au and Al+Au at 210 cm from the center of the TPC. Test runs displayed the capacity of the STAR detector to perform in a fixed-target configuration [44]. The success of the test runs motivated the fixed-target program, the dedicated fixed-target run in 2018 of Au+Au collisions at $\sqrt{s_{NN}} = 3.0$ GeV changed the location of the target to 200.7 cm, closer to the edge of the TPC. This change showed an improvement of the acceptance at target rapidity. The fixed-target setup consists of two long support rods and a half collar to hold the thin gold target. For the 2018 run, the target thickness was reduced to 0.25 mm; Figure 22 shows a picture of the rods, holding collar and gold

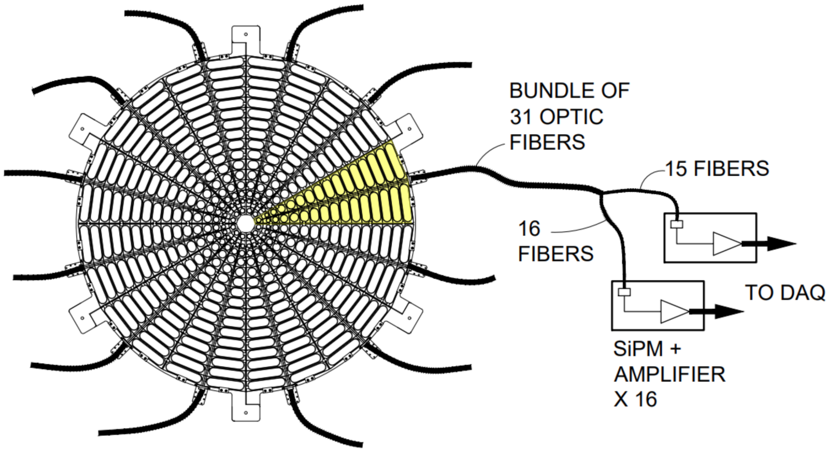

Figure 21: Schematic of the EPD. Figures shows the tiles in one "wheel" of the EPD, it shows 372 tiles. Figure from [43].

foil.

Figure 22: Fixed target apparatus including support beams, holding collar and gold foil. Figure from [39].

The RHIC setup for the 2018 run ran 12 bunches of 7×10^9 ions. The data acquisition system limited the data taking rate at 1 kHz. The beam was lowered 1.8 cm onto the target and in order to achieve the 1 kHz rate only the edge of the beam was incident on the target. At high energy collider mode, the acceptance is independent of $\sqrt{s_{NN}}$. However, in a fixed-target geometry, as the beam energy increases, midrapidity is closer to the beam line. Additionally, midrapidity is different for each particle species.

3 Definition of Important Terms in Heavy Ion Collisions

3.1 Kinematic of Heavy Ion Collisions

Some of the most important kinematic variables used in this work are described in the following subsections.

3.1.1 Rapidity and Pseudo-rapidity

Figure 8 shows the evolution of a heavy ion collision of two nuclei in the time (t) and position (z), the latter corresponds to a position along the direction of the beam line. In the case of a fixed-target experiment, only one beam is accelerated, which shows a Lorentz contracted nucleus that approaches the target at the speed of light. In Figure 8, the collision happens at ($t = 0$, $z = 0$). In the collision, a fireball is created and it expands in space-time until it creates particles which are measured by the detectors. In relativistic mechanics, neither Δt nor Δz are invariant quantities. Instead, the quantity $\Delta\tau^2 = \Delta t^2 - \Delta z^2$ is an invariant quantity, it is known as the proper time (τ). In heavy ion collisions, the accelerated particles have a finite mass, therefore they cannot travel faster than the speed of light. Hence, the only accessible region is when $\tau^2 = t^2 - z^2 > 0$, which corresponds to the "time-like" region. Therefore, particle production only happens in the time-like region. In relativistic kinematics, the rapidity variable is defined as:

$$y = \frac{1}{2}\ln\frac{E + p_z c}{E - p_z c} \tag{29}$$

$$y = \frac{1}{2}\ln\frac{1 + p_z c/E}{1 - p_z c/E} = \tanh^{-1}\left(\frac{p_z c}{E}\right) \tag{30}$$

where p_z is the momentum in the beam-line direction and E stands for energy of the particle. The energy can be calculated by using the energy-momentum relationship of the particle with rest mass M

$$E^2 = c^2p_z^2 + c^2p_y^2 + c^2p_x^2 + c^4M^2. \tag{31}$$

Rapidity is the relativistic analog of non-relativistic velocity. This can be observed in the non-relativistic limit, which is when $p << M$, where $p = |\vec{p}|$

$$y = \frac{1}{2}\ln\frac{\sqrt{c^2p^2 + c^4M^2} + Mv_zc}{\sqrt{c^2p^2 + c^4M^2} - Mv_zc} \approx \frac{1}{2}\ln\frac{Mc^2 + Mv_zc}{Mc^2 - Mv_zc}$$

$$y = \frac{1}{2}\left[\ln(1 + v_z/c) - \ln(1 - v_z/c)\right] \approx v_z/c. \tag{32}$$

Consider that the beam-direction is chosen to be in the z-direction. Therefore the Lorentz boost occurs only in the z-axis. The Lorentz transformed quantities are:

$$ct' = \gamma(ct - \beta z) \tag{33}$$

$$z' = \gamma(z - \beta ct) \tag{34}$$

$$E'/c = \gamma(E/c - \beta p_z) \tag{35}$$

$$p'_z = \gamma(p_z - \beta E/c) \tag{36}$$

where $\gamma = 1/\sqrt{1 - (v/c)^2}$ and $\beta = v/c$. The momentum and position in the x and y directions remain unchanged. The values of rapidity when there is no contribution in the z-direction gives a zero rapidity. On the other hand, when the particle moves exclusively in the z-direction, the value of rapidity approaches infinity. One can calculate the rapidity for the boosted frame.

$$
\begin{aligned}
y' =& \frac{1}{2}\ln\left(\frac{E' + p'_z c}{E' - p'_z c}\right) && (37)\\
=& \frac{1}{2}\ln\left(\frac{\gamma E/c - \beta\gamma p_z + \gamma p_z - \beta\gamma E/c}{\gamma E/c - \beta\gamma p_z - \gamma p_z + \beta\gamma E/c}\right) && (38)\\
=& \frac{1}{2}\ln\left(\frac{\gamma(E/c + p_z) - \beta\gamma(E/c + p_z)}{\gamma(E/c - p_z) + \beta\gamma(E/c - p_z)}\right) && (39)\\
=& \frac{1}{2}\ln\left(\frac{E/c + p_z}{E/c - p_z}\frac{\gamma - \beta\gamma}{\gamma + \beta\gamma}\right) && (40)\\
=& \frac{1}{2}\ln\left(\frac{E + p_z c}{E - p_z c}\right) + \ln\left(\sqrt{\frac{1-\beta}{1+\beta}}\right) && (41)
\end{aligned}
$$

y' can be expressed in term of y as:

$$
y' = y + \ln\left(\sqrt{\frac{1-\beta}{1+\beta}}\right). \tag{42}
$$

If two particles after the collision have rapidities y_1 and y_2 according to an observer, another observer also measures the rapidities of the same two particles as y'_1 and y'_2. The difference between the rapidities of the two particles is independent of the Lorentz boost along the z-direction.

$$
y'_1 - y'_2 = y_1 - \ln\left(\sqrt{\frac{1-\beta}{1+\beta}}\right) - (y_2 - \ln\left(\sqrt{\frac{1-\beta}{1+\beta}}\right)) = y_1 - y_2. \tag{43}
$$

Therefore, Δy is not affected by the Lorentz boost of the system along the z-axis. When the system is highly relativistic, rapidity cannot be measured easily. Therefore, rapidity is approximated in the high momentum regime and is called pseudo-rapidity(η)

$$
\begin{aligned}
y =& \frac{1}{2}\ln\left(\frac{E + cp_z}{E - cp_z}\right) && (44)\\
=& \frac{1}{2}\ln\left(\frac{\sqrt{c^4M^2 + c^2p^2} + pc\cos\theta}{\sqrt{c^4M^2 + c^2p^2} - pc\cos\theta}\right). && (45)
\end{aligned}
$$

At very high energy, $p >> m$, the mass can be neglected:

$$y = \frac{1}{2} \ln \left(\frac{cp + cp \cos\theta}{cp - cp \cos\theta} \right) \tag{46}$$

$$= - \ln(\tan\theta/2) \equiv \eta \tag{47}$$

θ corresponds to the angle made by the particle trajectory with the beam pipe. η only depends on the angle, which is useful experimentally when the details of the particle (mass and momentum) are not known.

3.2 Geometry in Heavy Ion Collisions

Two accelerated nuclei close to the speed of light contract along the direction of the motion. Due to relativistic effects, the shape of the two nuclei just before the collision resembles the shape of two "pancakes". The impact parameter (b) is defined as the distance between the centroids of the two colliding nuclei, a schematic representation of the overlap between two nuclei is shown in Figure 23. The system size dependence and the number of colliding nucleons can be studied by either changing the species of colliding ions or by changing the impact parameter between the colliding nuclei.

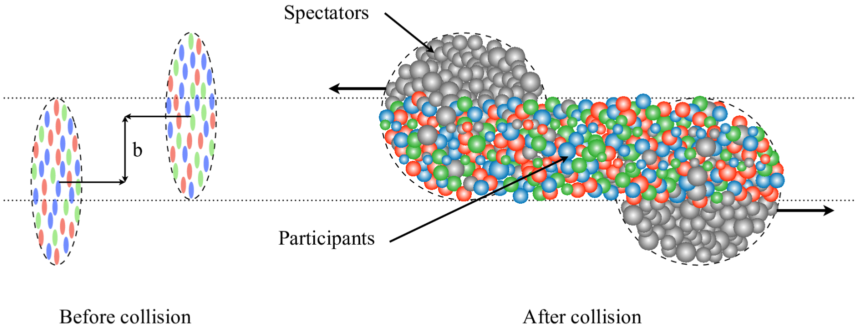

Figure 23: Schematic representation of a heavy ion collision and the relation with the impact parameter and number of participants. Figure from [45].

An event with small impact parameter ($\sim 0-3$ fm for Au+Au collisions) is referred to as a central event, in which most of the colliding nucleons participate in the collision. Mid-central collision are found between ($\sim 3-6$ fm), semi-peripheral($\sim 6-8$ fm) and peripheral ($\gtrsim 10$ fm). Measuring the impact parameter directly, could give access to study observables as a function of system size. Unfortunately, the impact parameter cannot be measured directly and therefore one relies on models to estimate the initial geometry of the event. The most common model used to determine the event centrality is the Glauber Monte Carlo (GMC) method. In this model, the nucleus is described as a collection of uncorrelated nucleons. The Glauber Monte Carlo model depends on two experimental inputs, the nuclear charge density and the nucleon-nucleon cross section.

3.2.1 The Glauber Model

As mentioned before, the GM provides the initial conditions of the heavy-ion collision but it does not provide the particle production after the collision. Due to that, the GM is paired with the negative binomial distribution (NBD). Two experimental inputs are necessary in the Glauber Monte Carlo model, the nuclear charge density of the nucleus and the nucleon-nucleon cross section. The nuclear charge density is described by a three parameter Fermi distribution and the nucleon-nucleon cross section is obtained from $p+p$ data. The Glauber Monte Carlo model uses a nucleon distribution obtained from measurements of charge distribution of the nucleon with electron scattering experiments. The charge distribution is then parameterized by using the three parameter Fermi distribution (Wood-Saxon Distribution [46]). The calculation begins by placing the two gold (Au) ions in a 3D space. The Au ions are populated with nucleons randomly selected from the Wood-Saxon density, with Gold parameters, surface thickness $a = 0.535$ fm, nuclear radius $R = 6.38$ fm and a spherical deformation $\omega = 0$. After placing the 197 nucleons inside each nucleus, a random impact parameter (b) is chosen. In order to simulate the initial conditions of the collisions, the 3D space has to be projected on to a 2D system, to represent the "Pancake" like behavior of the ions before the collision.

3.3 Reference Multiplicity

The impact parameter (b) is directly correlated with the number of participants (N_{Part}); the latter is defined as the number of nucleons that participate in at least one inelastic nucleon-nucleon reaction. These two quantities are used to define the centrality and it should be noted that although they are physically different quantities, they are often used interchangeably to represent centrality. In real experimental heavy ion collisions, measuring the number of participants N_{Part} or b is a difficult task, therefore a direct experimental measurement is used to define centrality. Both b and N_{Part} are monotonically related with the particle multiplicity after the collision at both forward rapidity and midrapidity [47]. For low values of the impact parameter (b), it is expected to observe high number of participants, which results in a small number of spectators and large particle multiplicity at midrapidity. The uncorrected charged track multiplicity in a pseudorapidity window (reference multiplicity) is often used as an observable to define centrality. The average value of a reference multiplicity class should correspond to the average of N_{Part} and b, this relation can be observed in Figure 24, where it illustrates the event multiplicity within $|\eta| < 1$ distribution. The corresponding values are determined by using a Glauber and particle production model.

The dataset used for the centrality determination is the same used in the lambda fluctuation analysis. The data set contains 147 million of minimum bias events. The minimum bias events are required to satisfy more than three hits in the Time of Flight (TOF) detector and a hit in either trigger detector, the EPD or BBC detector. The events used in the centrality definition require a z vertex location between $199.5 < v_z < 202$ cm with respect to the center of the TPC, as shown in Figure 16 and a radial vertex location of $v_r < 1.5$ cm from the center of the beam spot, corresponding to $v_{x,y} = (0, -2)$ cm. The reference multiplicity used in the STAR detector is limited to the particle production at midrapidity. In the collider mode at STAR, the reference multiplicity used is the $RefMult$, which is defined as the total number of charged tracks in a pseudorapidity window of $|\eta| < 0.5$ with specific detector cuts. Particle fluctuation analyses are susceptible to artificial enhancements due to the inclusion of the same particle in the reference multiplicity. This

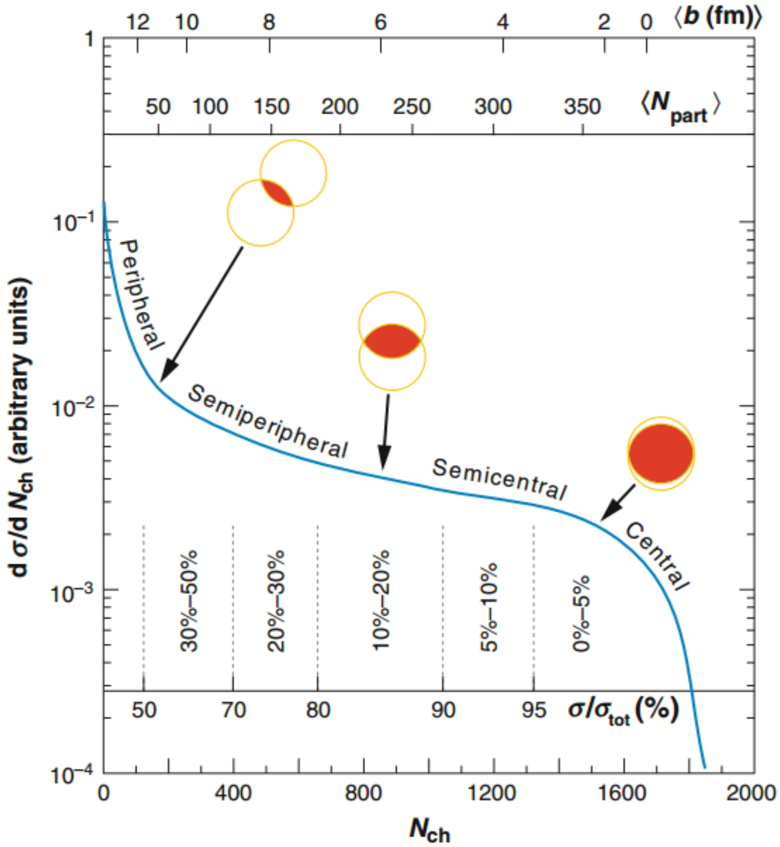

Figure 24: Illustration example of the total final state charge particle multiplicity N_{ch} distribution with Glauber-calculated quantities (b, N_{Part}). Figure from [47].

effect is labeled as the “auto-correlation” effect [48]. For the first Beam Energy Scan (BES), it was shown that the $RefMult$ is not a suitable reference multiplicity for the proton fluctuation analysis, due to the inclusion of proton tracks in the reference multiplicity. In order to suppress the auto-correlation effect, the reference multiplicity used for the protons analysis is the $RefMult3$ which excludes protons. Additionally, the pseudorapidity window for the reference multiplicity was increased from $|\eta < 0.5|$ to $|\eta < 1.0|$ to offset the lowered particle multiplicity. Similarly, for the first lambda fluctuations analysis, the reference multiplicity used is the $RefMult3$. This is done in order to avoid autocorrelations from the proton daughter particle used for the lambda reconstruction. Studies showed that the inclusion of pions (daughter particle of lambda) does not contribute to autocorrelation effects [41].

3.3.1 Track Selection in the Reference Multiplicity

In the fixed target mode, two new reference multiplicity were introduced: The $FxtMult$ and the $FxtMult3$, the first was used as a common reference multiplicities in many physics analyses and the latter was the reference multiplicity used in the event-by-event proton analysis and the event-by-event lambda analysis. Both of the reference multiplicities are uncorrected charged tracks in the detector acceptance of $-2 < \eta < 0$, with the exclusion of primary protons in order to reduce autocorrelation effects in the fluctuation analysis of protons and lambdas. Additional track quality cuts were used in the references multiplicities to ensure that all tracks were originated from the primary vertex:

- A track must be a primary track.
- The distance of closest approach (DCA) of a track to the primary vertex is less than 3 cm.
- A track must have a ratio between the number of fit points and possible fit points ($nHitsFit/NHitsPoss$) greater than 0.52.
- The number of dE/dx points of a track is greater than 10.
- The track is reconstructed with a pseudorapidity between -2.0 and 0.0.
- In the $FxtMult3$, proton tracks are not considered. Therefore, the proton band dE/dx vs rigidity is 3σ below the model prediction.

Figure 25 shows diagrams of the difference between the detector acceptance of the different reference multiplicities between the collider geometry ($RefMult$ and $RefMult3$) and the fixed target geometry ($FxtMult$ and $FxtMult3$). The left panel shows the acceptance for the collider geometry, where red and blue lines indicate the opening angle of $RefMult$ ($|\eta| < 0.5$) and $RefMult3$ ($|\eta| < 1$) tracks, respectively. The right panel shows the acceptance for the fixed target geometry, where green lines indicate the opening angle of $FxtMult$ and $FxtMult3$ ($-2 < \eta < 0$) tracks. The yellow square indicates the position of the fixed target. The main difference between the reference multiplicity from collider geometry and fixed target geometry, is the larger opening angle at the fixed target geometry, which increases the particle yield at these lower energies, where particle production is reduced.

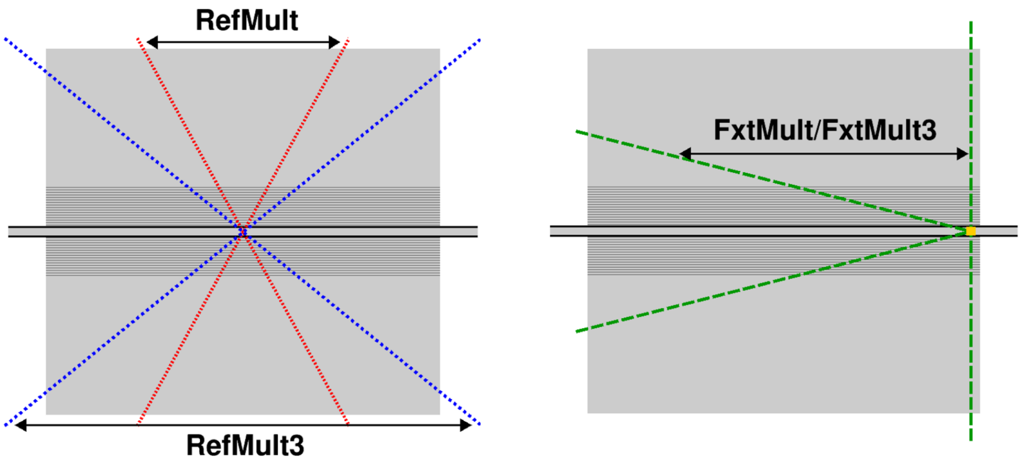

Figure 25: Comparison between reference multiplicities in the collider mode (left panel) and the fixed target mode (right panel).

3.4 Centrality Bin Determination

The Centrality Bin determination was determined by the UC Davis Nuclear Group [39]. This section briefly describes the procedure. In order to determine the centrality bins used in the fluctuation analysis using the multiplicity distribution from the reference multiplicity, the Glauber Model (GB) and a Negative Binomial Distribution (NBD) are used. The geometric model used in heavy ion physics is the Glauber Monte-Carlo, which provides an estimate of the number of binary collisions (N_{coll}), participant nucleons (N_{Part}) and impact parameter of the initial collisions (b).

3.4.1 Inelastic Cross Section σ_{inel}^{NN}

The inelastic cross section is used as a criterion for a nucleon-nucleon interaction. In the Glauber Monte Carlo, a collision occurs if two nucleons are within $\sqrt{\sigma^{NN}/\pi}$ in the transverse plane. At high center of mass energies ($\sqrt{s_{NN}}$) the input cross section of the Glauber Monte Carlo is dominated

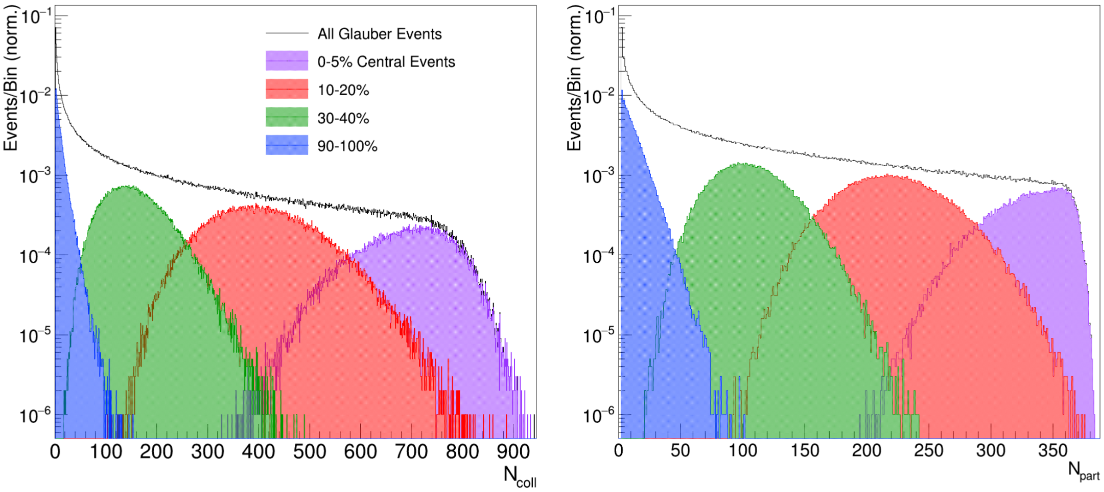

Figure 26: N_{coll} and N_{Part} distributions calculated from Glauber Monte Carlo events for different centralities. Figure from [39].

by inelastic scattering while elastic scattering is negligible. At low center of mass energies, the elastic scattering is no longer negligible and is comparable to the inelastic contribution. The elastic contribution comes from elastically-scattered protons, which for our purposes in the $FxtMult3$ are excluded. Therefore, elastically-scattered protons and the elastic cross section are ignored. The inelastic nucleon-nucleon cross section used for the $\sqrt{s_{NN}} = 3.0$ GeV dataset is $\sigma_{inel}^{pp} =$ (27.28±0.76±0.3) mb taken from the PDG summary tables [49]. Figure 26 shows the distributions of N_{Part} and N_{coll} produced from the Glauber Monte Carlo model, using the Wood-Saxon distribution and the inelastic cross section mentioned above.

3.4.2 Particle Production Model

As mentioned before, the Glauber Monte Carlo model outputs N_{Part}, N_{coll} and b, which cannot be related to the reference multiplicity $FxtMult3$ directly. Therefore, in order to generate the final state particle multiplicity, a particle production model is required. The model assumes that the particle multiplicity is composed by two processes, the "hard" and the "soft" processes. Therefore, the total collision energy produced is $E_{tot} \propto E_{hard} + E_{soft}$. Where E_{hard} is proportional to N_{coll} while E_{soft} is proportional to N_{part}, which gives $E_{tot} \propto \sqrt{s_{NN}}(xN_{coll} + (x-1)N_{Part}/2)$, x being the scaling between the hard and soft particle production. With the assumption that the particle production is proportional to the energy, E_{tot} can be converted to the total number of produced particles N_{ch}

$$N_{ch} = n_{pp}\left(xN_{coll} + (1-x)\frac{N_{part}}{2}\right) \tag{48}$$

where n_{pp} is the particle multiplicity of a p+p collision at the same energy per nucleon of the system under study, for this analysis $\sqrt{s_{NN}} = 3.0$ GeV. This method relies on the assumption that there is an equivalence between the nucleon-nucleon and $p + p$ collisions, and also that there is a clear distinction between hard and soft collisions. This method is known as the two component model [50]. The two component model converts the N_{Part} and N_{coll} obtained from Glauber model to a total multiplicity which can be related to the reference multiplicity. It requires two parameters; the hardness parameter x and the event-by-event $p + p$ multiplicity n_{pp}. From previous work, it was shown that $p + p$ multiplicity distributions are well simulated using a negative binomial distribution (NBD) [51]. A negative binomial distribution (NBD) describes the number of successes (n) from identical Bernoulli trials before a number of failures occur (k). The number of successes are represented by the number of generated particles n_{pp} and the k-parameter is related to the particle dispersion $D^2 = \langle n_{pp}^2\rangle - \langle n_{pp}\rangle^2$ by

$$\frac{D^2}{\langle n_{pp}\rangle^2} = \frac{1}{\langle n\rangle} + \frac{1}{k}. \tag{49}$$

Therefore, the NBD for particle production is given by

$$NBD_{n_{pp},k}(n_{pp}, \langle n_{pp}\rangle, k) = \left(\binom{n_{pp}+k-1}{k-1}\right)\left[\frac{\langle n_{pp}\rangle/k}{1+\langle n_{pp}\rangle/k}\right]^{n_{pp}}\frac{1}{[1+\langle n_{pp}\rangle/k]^{n_{pp}}}. \tag{50}$$

The hardness parameter used for the two component model is $x = 0.06$. The Glauber Model + NBD model provides a method to relate the total particle production to a centrality class. However, detector effects such as acceptance or efficiency are not considered. To account for both effects, the UrQMD(Ultrarelativistic Quantum Molecular Dynamics), which is discussed in Section 8, was used to simulate events and to estimate the acceptance limitations and the STAR embedding, which is discussed in Section 6.1.1. Efficiency curves were used to estimate the efficiency effects. The centrality classes were determined by applying the Glauber+NBD fit to the reference multiplicity $FxtMult3$, as shown in Figure 27. At high multiplicities, there is a disagreement between data and the model fit. This is due to double collisions in the data (pile up). Below 80, the pile up contamination is insignificant to the centrality determination ($\approx 0.5\%$ background effect) which does not affect the fitting procedure. The cuts for the corresponding centrality classes are shown in red dotted lines, while the black dashed line is the upper pile up cut at $FxtMult3 = 80$. The lowest centrality bin for this analysis is $50 - 60\%$ which corresponds to the range $4 \leq FxtMult3 < 6$.

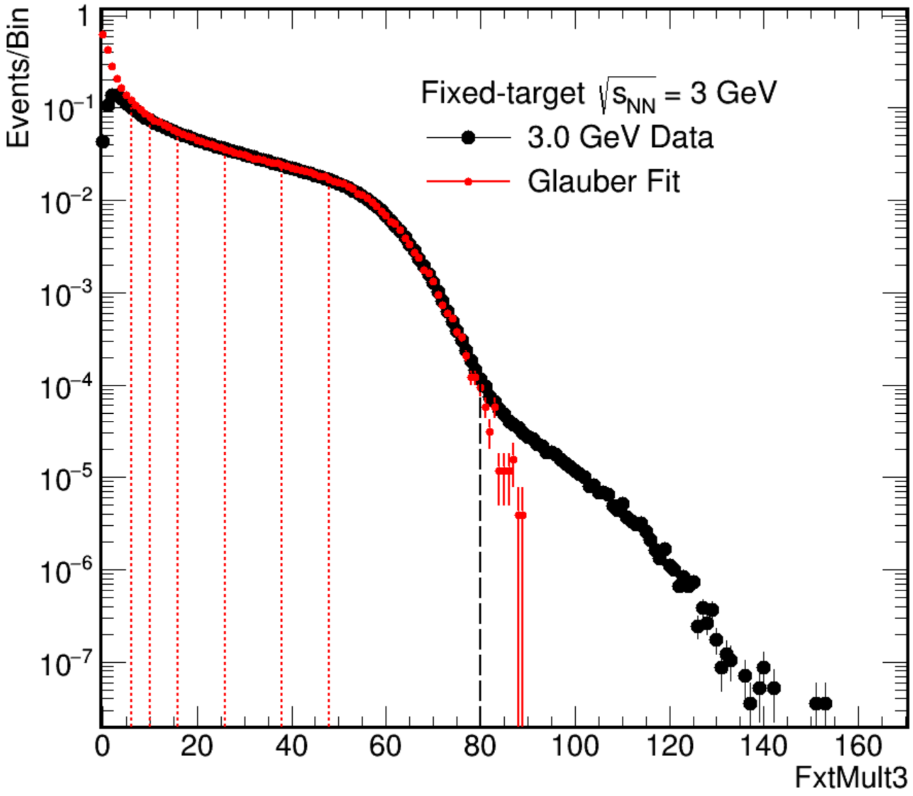

Figure 27: Glauber Model+NBD fit on the $FxtMult3$ histogram. The lowest cut is at $N_{ch} = 4$, the upper cut is at $N_{ch} = 80$. Figure from [39].

Table 1 shows the centrality classes with the corresponding $\langle N_{Part} \rangle$, $\langle N_{coll} \rangle$ and $\langle b \rangle$.

Table 1: $FxtMult3$ centrality class

% Central	N_{ch} Cut	$\langle N_{Part} \rangle$	$\langle N_{coll} \rangle$	$\langle b \rangle$ (fm)
$0-5$	48	326 ± 11	679 ± 24	2.5 ± 0.3
$5-10$	38	282 ± 8	562 ± 23	3.9 ± 0.2
$10-20$	26	219 ± 8	409 ± 17	5.5 ± 0.3
$20-30$	16	157 ± 7	259 ± 16	7.2 ± 0.3
$30-40$	10	107 ± 5	157 ± 9	8.6 ± 0.2
$40-50$	6	70 ± 5	92 ± 6	9.7 ± 0.2
$50-60$	4	47 ± 5	56 ± 7	10.6 ± 0.4

4 Event Selection and Lambda Reconstruction

The lambda fluctuation analysis uses the data set collected from the fixed-target runs at RHIC. The full data-set was collected from May 31st to June 4th of 2018 and the total number of triggered events were 320 million at $\sqrt{s_{NN}} = 3.0$ GeV. The number of used events for the analysis was reduced due to the removal of poor-quality data and also the sensitivity of the analysis, which required the removal of periods of data taken with unusual events. This chapter covers briefly the data collection and storage, the event selection and the lambda reconstruction procedure.

4.1 Data Collection and Run Selection

During the running of the experiment, the raw data from each sub-detector is recorded in a data acquisition file ("DAQ" file). In order to use the data for physics analysis purposes, the "DAQ" files were parsed and calibrated to extract detector measurements. The output is saved in two file formats used for physics analyses: The MuDST and picoDST, which are stored in the Brookhaven national Laboratory Scientific Data and Computing Center (SDCC). These files store event information in a data tree, which is useful for event-based analysis. The commonly used event and track information is stored in picoDST files, which are the ones used for this analysis. To reduce the data sizes using just information necessary to a particular analysis, analyzers designed the femtoDST, which can be used for analysis performed on a personal computer. To give a idea of the file sizes, the total picoDST and femtoDST for the $\sqrt{s_{NN}} = 3.0$ GeV are ~ 4.0 TB and ~ 40 GB, respectively.

As mentioned before, due to the sensitivity of the fluctuation analysis, runs with fluctuations outside certain variable values were removed. Tracks and event variables were averaged over a run in order to identify poor quality runs. The studied variables were $\langle FxtMult \rangle$, $\langle V_r \rangle$, $\langle V_z \rangle$, $\langle \eta \rangle$, $\langle \phi \rangle$, $\langle DCA \rangle$ and $\langle p_T \rangle$. Figure 28 shows an example of the run-averaged $\langle p_T \rangle$. Runs outside 3 root mean squared (RMS) of the run-averaged variable are removed, the run-average is calculated again. This process is repeated until all data points outside the 3 RMS are removed. After all cuts. the analysis includes 72 high quality runs.

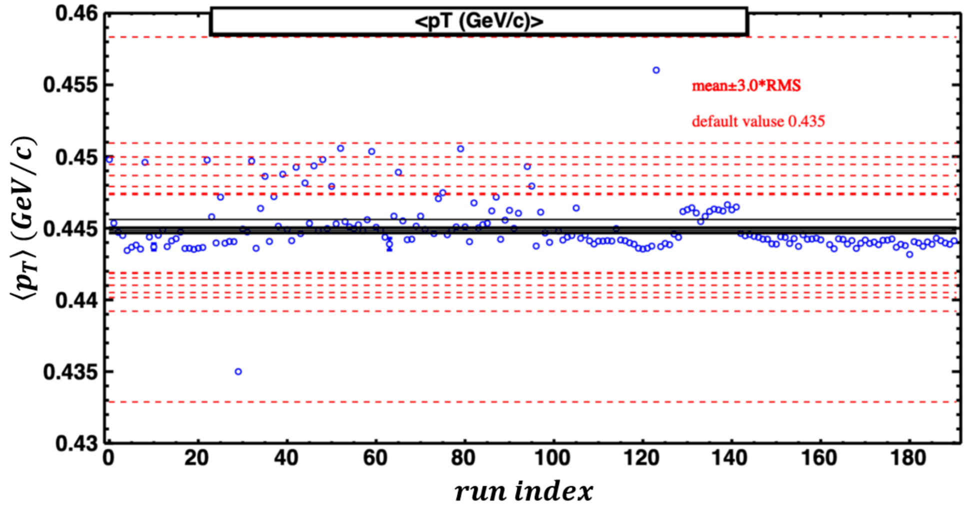

Figure 28: $\langle p_T \rangle$ averaged over the run as a function of the run index. Plot from Guannan Xie.

4.2 Event Selection

The minimum-bias Au+Au collisions taken in 2018 in fixed target mode required triggered events that had at least one hit in either EPD or the East BBC and three or more hits in the TOF detector. These triggers were labeled as “bbce_tofmult1” and “epde_tofmult1”. The eastward beam (with nucleon energy of 3.85 GeV) was steered down (shifted in the $y = -2$ cm direction in the STAR geometry) to hit a 1 mm-thick gold foil (fixed-target) placed at 200.7 cm from the center of the TPC. In order to remove potential collisions with the target-support material and events with incorrect timing information, all events require a z vertex location of $199.5 < v_z < 202$ cm, a radial vertex cut of $v_r < 1.5$ cm from the center of the beam spot, meaning $v_{x,y} = (0, -2)$ cm. Figure 29 and Figure 30 show the event distribution for the z-component and the transverse component, respectively.

The $v_x - v_y$ 2D distribution, before and after all cuts are shown in Figure 31.

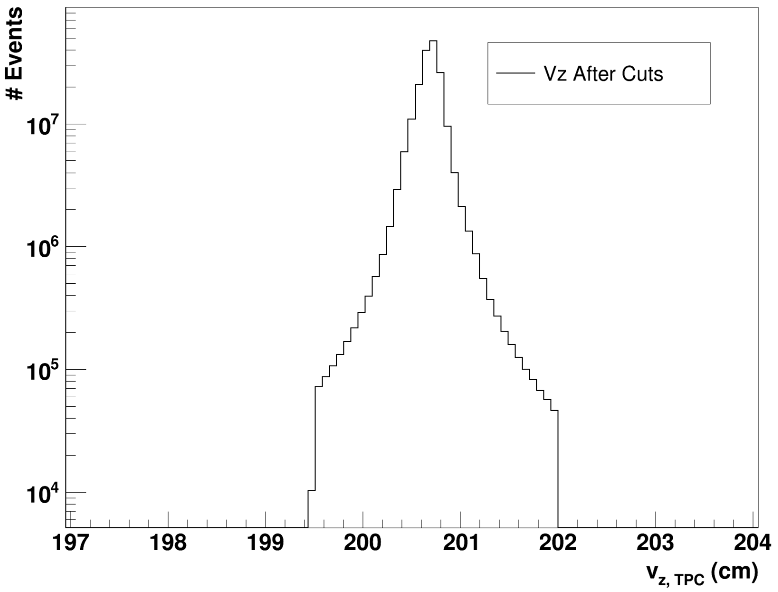

Figure 29: v_z distribution peaked at $v_z = 200.7$ cm. Cut is applied $199.5 < v_z < 202$.

4.3 Track Selection

Certain track-level cuts were implemented in order to ensure that tracks contain the correct dE/dx and momentum information. The location of an event vertex is determined by projecting global track helices to the beam line and then searching for the intersection of tracks. The vertex candidate is generated by searching for multiple tracks that intersect within the beam line. The primary vertex is defined by sorting the vertex candidates. If the distance of closest approach (DCA) of the track to the primary vertex is below 3.0 cm, the global track is labelled as a primary track. For this analysis, a cut of DCA $<$ 3.0 cm is used in order to lower the background contribution from beam-pipe collisions and contribution of secondary decays, the latter especially for the $FxtMult3$ definition.

The charged particle helices are fitted by using the spatial points from the TPC in order to generate tracks. The fits are performed using a Kalman filter procedure. The number of spatial points used to fit each helix is known as $NHitsFit$, the helix fitting procedure requires at least five spatial points. In general, the greater the number of $NHitsFit$ the better the momentum

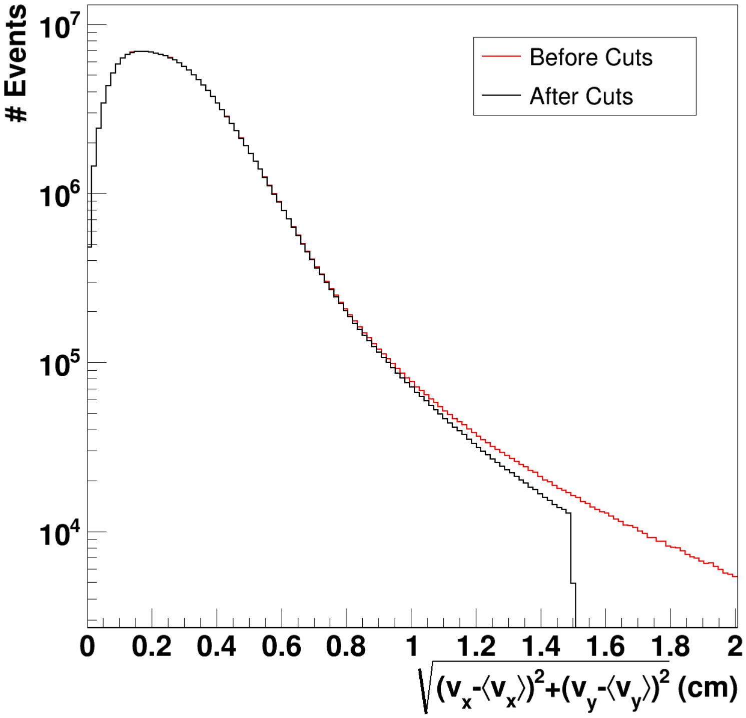

Figure 30: v_r distribution before and after cut. A cut on v_T about the beam spot $\langle v_{x,y}\rangle$ $(0, -2)$ cm is applied $v_T = 1.5$ cm

resolution of the track. Therefore, in order to increase the track quality, a minimum number of $NHitsFit$ is used. For the lambda analysis a minimum of at least 15 fit points ($NHitsFit > 15$) is required. A decrease of $NHitsFit$ to 12 and 10 is used for systematic studies.

In order to ensure that, during the reconstruction of charged particles, a single charged particle is identified, the value $NHitsPoss$ is used. $NHitsPoss$ allows to identify duplicate, or split, tracks from the possible $NHitsFit$. In the central region of the TPC, the maximum number of spatial points is the number of pad rows. By requiring all tracks to have $NHitsFit/NHitsPoss > 0.52$, duplicated tracks are eliminated.

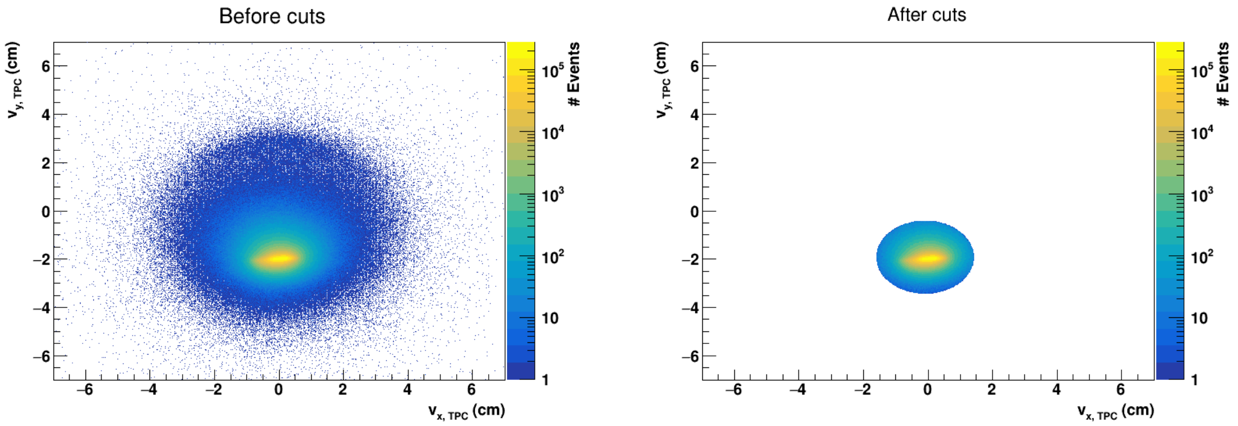

Figure 31: (a) $v_x - v_y$ distribution before cuts. (b)$v_x - v_y$ after all cuts.

4.4 Lambda Reconstruction

The reconstruction of the primary lambda particle (Λ) is done using the secondary protons (p) and pions (π^-). The identification of the daughter particles (p and π^-) was done using the ionization-energy loss in the TPC gas as explained in Section 2.2.1. In order to obtain high quality tracks, the cuts discussed in Section 4.3 were imposed. Since lambda particles are neutral particles, the direct identification is not possible due to the lack of deflection in the presence of the external magnetic field. Therefore, the extraction of the lambda yields was done by reconstructing the decay vertex of the particle. The lambda baryon decays weakly in the decay channel, $\lambda \to p + \pi^-$, the branching ratio is $(63.9 \pm 0.5)\%$ [52]. The reconstruction of the lambda particle is done via the calculation of the lambda invariant mass (M_{p,π^-}) using the properties of the identified daughter particles by considering the conservation of the 4-momentum. Consider p_Λ, p_p and p_{π^-}; the 4-momentum of lambda, proton and pion, respectively. The 4-momentum of a particle is given by $p = (E, \vec{p})$, where $\vec{p}$ is the momentum of the particle; and the speed of light $c = 1$ convention is used.

$$p_\lambda = p_p + p_{\pi^-} \tag{51}$$

Using the invariance of the quantity $p^{\mu}p_{\mu} = E^2 - \vec{p}^2$:

$$
\begin{aligned}
-M^2_{p,\pi^-} &= (p_p + p_{\pi^-})^2 \\
-M^2_{p,\pi^-} &= M^2_p + M^2_{\pi} + 2(E_p E_{\pi^2} - \vec{p}_p \cdot \vec{p}_{pi^-}).
\end{aligned} \tag{52}
$$

The calculated invariant mass uses all identified proton and pion pairs, independently of whether they come from a primary lambda decay or not. Protons and pions that do not come from a lambda decay reconstruct into a mass different from the lambda rest mass ($M_{\Lambda} = 1115.683 \pm 0.006$ MeV/c^2) [52]. The net-lambda fluctuation analysis is an event-by-event fluctuation measurement. Therefore, the counting of lambda particles should be done on an event-by-event basis. The lambda particle yield in all the events can be done by integrating the peak above the background. Most of the background can be eliminated by applying a mass cut that considers the invariant mass of the lambda baryon. The mass cut used for this analysis is $1112.7 < M^{inv}_{p,\pi^-} < 1118.7$ MeV/c^2. Notice that, even after imposing the mass cut window, the invariant mass distribution inside the window still contains contribution from the background. In order to reduce the contamination from the background below the signal, certain cuts associated with the decay geometry were optimized to extract the signal with high purity. The appearance of the unobserved lambda decay into two observed charged daughter particles gives rise to the terminology V^0 to describe the decay topology. The standard method used to reconstruct lambda particles in the BESI [35], used several geometrical measurements associated with the V^0 decay as seen in Figure 32. This method relies on so-called distances of closest approach (DCA), which uses the distance between the V^0 to the primary vertex (PV), the distance between proton to PV, pion to PV, and proton to pion. The topological cuts are optimized to reduce the combinatorial background and obtain good statistics in the lambda signal.

For the lambda fluctuation analysis at $\sqrt{s_{NN}} = 3.0$ GeV, the standard method was not used. The procedure to reconstruct lambda baryons was by using a machine-learning-based algorithm which achieves overall better purity, called KFParticle [53], [54]. The Kalman filter (KF) method,

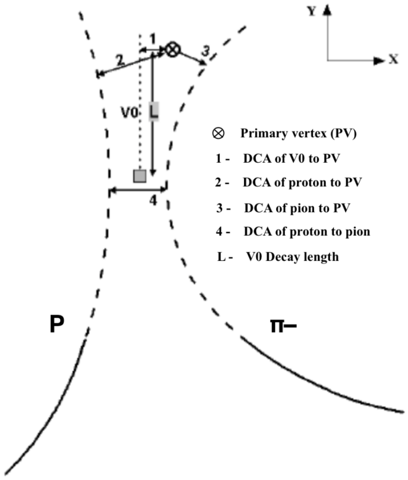

Figure 32: Cross section of V^0 decay topology in x-y plane.

is a recursive method used for the analysis of linear discrete dynamic systems described by a vector of parameters, called state vector. The state vector of the particle includes eight parameters: three coordinates of the particle (x, y, z), three components of its momentum (p_x, p_y, p_z), the energy of the particle (E) and when the production point of the particle is known, the time between the production and decay points measured in a distance normalized by the momentum $(s = l/p)$.

$$\vec{r} = (x, y, z, p_x, p_y, p_z, E, s). \tag{53}$$

By using the state vector, the KFParticle can determine the decay vertex, momentum and energy of a reconstructed particle. The covariance matrix is estimated together with the state vector, which allows to obtain parameters and also their accuracy by calculating the value of the χ^2. Some of the most important χ^2 criterion are:

- χ^2_{prim}: Defines the probability that the track intersects the primary vertex within the errors under the assumptions that parameters of tracks are Gaussian distributed and χ^2_{prim} is distributed according to the χ^2-distribution with the number of degrees of freedom (NDF) equal to 2. NDF is equal to 2 since only two coordinates of a track (out of three) are independent, since the tracking systems provide measurements with one coordinate fixed.

- χ^2_{topo} : χ^2 criterion of the lambda candidate with a production point constraint set to the primary vertex; this criterion characterizes whether the particle is produced in the primary vertex region.

- χ^2_{NDF}: criterion calculated by the KFParticle in the lambda candidate fit, that characterizes whether trajectories of daughter particles (p and π^-) intersect within their errors.

Within the KFParticle framework, one cuts on probabilities (parameters normalized on the error) rather than absolute values of topological variables as done in the standard method. The default cuts used in the KFParticle for the lambda reconstruction is shown in table 5.

Figure 33 shows V^0 topological structures used by the KFParticle; certain cuts are applied in order to significantly reduce the combinatorial background. The cuts were optimized by considering reducing the combinatorial background and increasing the reconstruction efficiency.

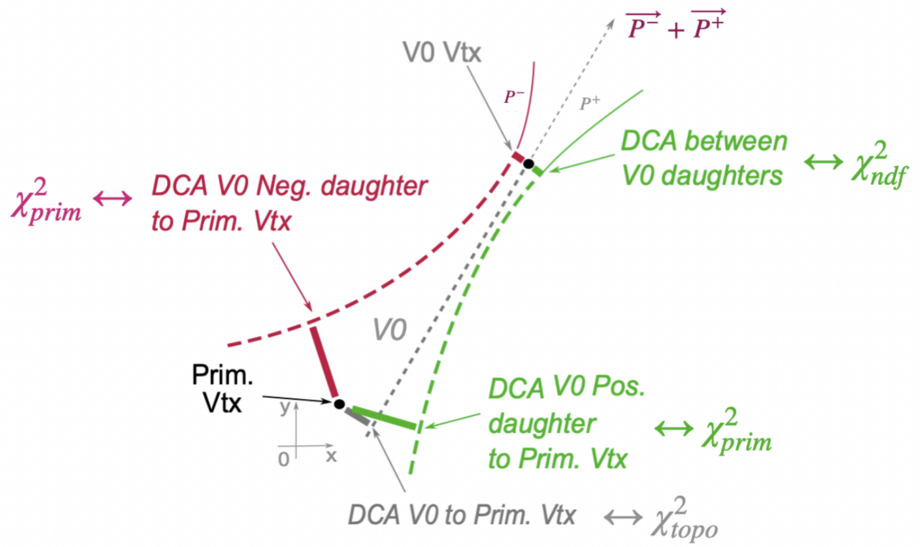

Figure 33: V_0 decay topology for strange particle decay used in the KFParticle method. P^+ refers to a positively charged particle (e.g., proton) and P^- refers to a negative charged particle (e.g., π^-).

4.5 Purity of the V^0 Samples:

Various topological structures in the KFParticle were used in order to obtain the most probable V^0 candidate in the sample. The purity of the resulting V^0 was calculated for different variations of topological cut structures. In order to calculate the purity of the sample, one needs the extraction of the yield from the signal and the yield from the background under the signal region. This was done by counting the entries of the signal and background areas of the invariant mass distribution. A second-degree polynomial fit was applied to the background as shown by the green line in Figure 34. By using the background fit function, the area below the signal was estimated. The yield of the signal region was estimated by adding to the second-order polynomial fit two summed Gaussian distributions, which was found to work quite well to fit the data. The fit is shown by the red line in Figure 34. The area between the two summed Gaussian distribution fit and the second-order polynomial corresponds to the yield of the signal region.

By using the information from the signal and background yield, two quantities were calculated to quantify the level of the lambda reconstruction. The first is the signal to background ratio shown in Eq. (54) and the second is the purity shown in Eq. (55)

$$\frac{S}{B} = \frac{Signal}{Background} \tag{54}$$

$$Purity = \frac{Signal}{Signal + Background} \times 100\%. \tag{55}$$

Many topological cuts were studied but for our purposes only five cut-set variations were used in this analysis as shown in Figure 35 and included in the systematic uncertainties. Table 2 shows the cut variations used in the analysis with the corresponding information about the background, signal, S/B and purity.

As seen in Table 2, the purity of the sample depends strongly on the topological cuts used. The most strict topological cut used (cut set 3) shows purity of about 93.75%, but it can also be observed that, by increasing the purity, a portion of the signal is also lost at the same time.

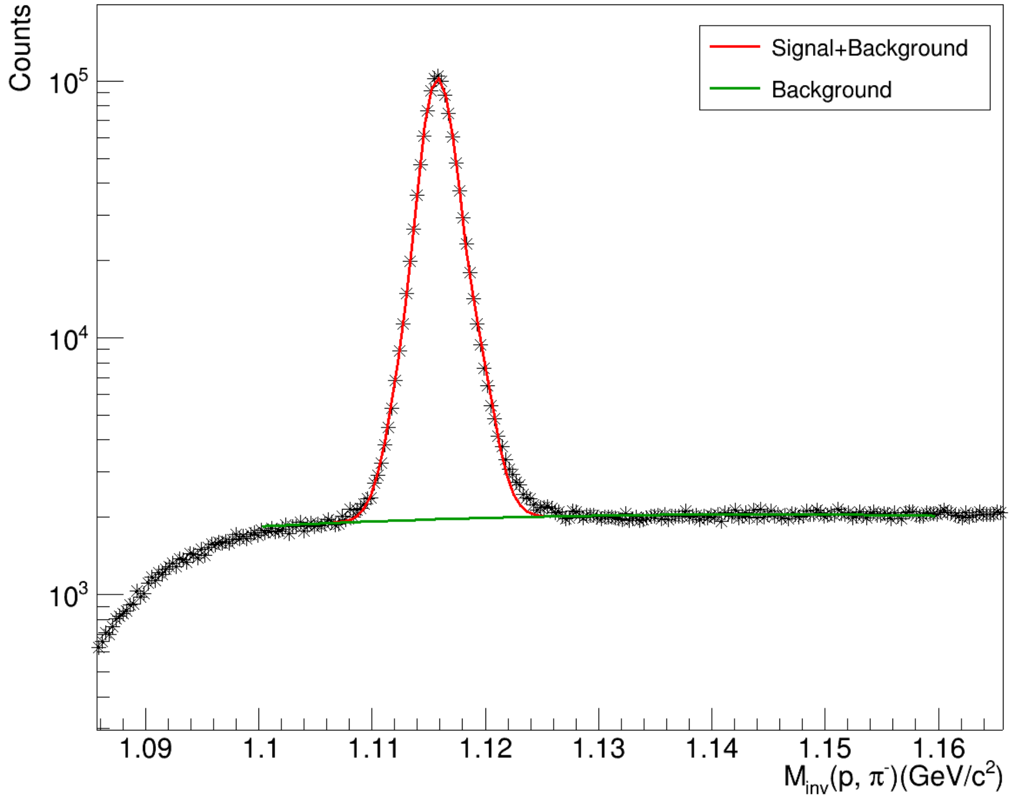

Figure 34: Signal and background in the lambda invariant mass distribution using proton (p) and pion (π^-) pairs from $\sqrt{s_{NN}} = 3.0$ GeV Au+Au collisions. The green line shows the second-order polynomial fit to the background, the red line corresponds to the two summed Gaussian distribution fit on the background+signal.

Therefore, in order to address the loss in the signal, the maximum purity of the sample used for this analysis is cut set 3. All other track-cut sets used in this analysis are listed in Table 4. The high purity of the sample can be also observed as a function of centrality for cut set 3 in Table 3

The pion lower-bound p_T cut is applied due to the low tracking efficiency. The proton lower-bound p_T cut is applied to avoid spallation protons. The lower-bound p_T cut of lambda is applied because of low efficiency reconstruction (see Figure 41)

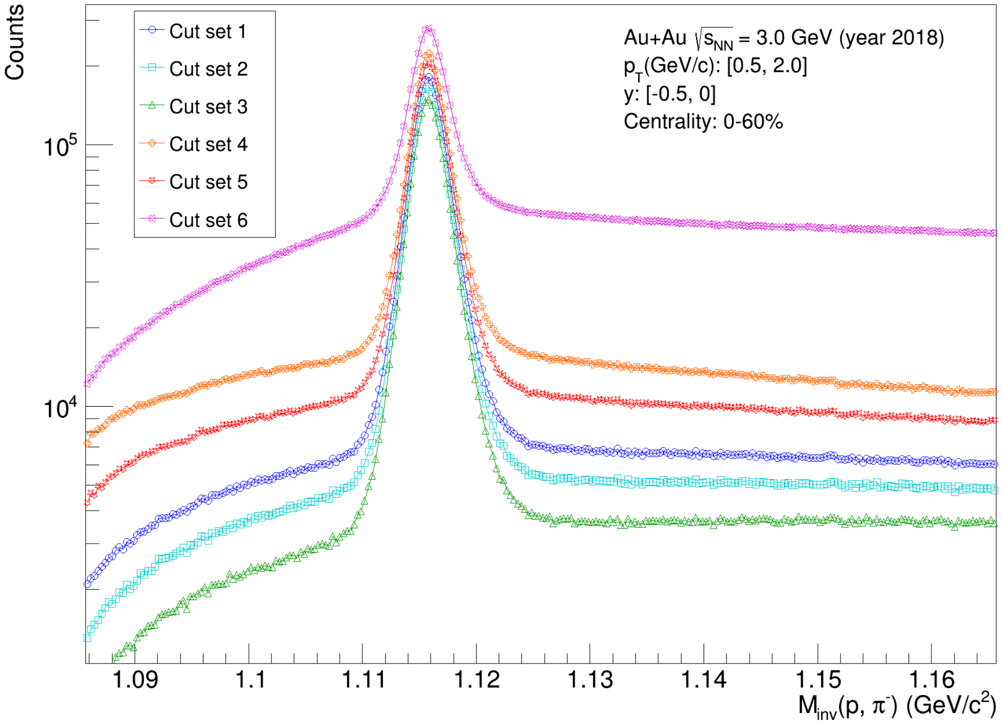

Figure 35: Invariant mass distributions for 6 cut set variations from Table 2.

4.6 Analysis Acceptance

The kinematic acceptance used in an event-by-event fluctuations of particle distributions has to be chosen carefully. If the acceptance window is too small, the correlations are expected to vanish. On the other hand, if the window covers a large fraction of the lambda distribution, the fluctuation is suppressed as the baryon number cannot fluctuate in the 4π yield due to baryon number conservation. For this analysis, the chosen nominal rapidity window is within $-0.5 < y < 0$, which represents approximately half the measurable acceptance of $-0.9 < y < 0.1$. The lambda candidates are required to have a transverse momentum within $0.5 < p_T(\text{GeV/c}) < 2.0$. The transverse momentum (p_T) and rapidity (y) of the reconstructed V^0 in the signal region $1.1127 < M_{inv}(p, \pi^-)(GeV/c^2) < 1.1187$ at $\sqrt{s_{NN}} = 3.0$ GeV is shown in Figure 36. The red dashed line corresponds to the cut of $0.5 < p_T(GeV/c) < 2.0$ and $-0.5 < y < 0$ used in the analysis for a fixed acceptance. To study the effect of the selected kinematic acceptance, the rapidity was

Table 2: Purity of the V^0 candidates for different topological cut selections at $\sqrt{s_{NN}}$ = 3.0 GeV, for centrality $0-60\%$

Parameter	Cut Set 1	Cut Set 2	Cut Set 3	Cut Set 4	Cut Set 5	Cut Set 6
χ^2_{prim}	10	12	15	5	7	5
χ^2_{topo}	5	5	5	7	10	20
χ^2_{NDF}	5	5	5	5	6	7
Background	66.05	49.74	33.83	156.52	108.67	720.74
Signal	611.71	565.24	507.49	734.06	682.62	910.33
S/B	9.26	11.36	15.00	4.68	6.28	1.26
Purity	90.25 %	91.91 %	93.75 %	82.42 %	86.26 %	55.81 %

Table 3: Purity of the V^0 candidates for different centralities using cut set 3.

centrality	B	S	S/B	Purity
60-50	0.493	5.053	10.241	91.1 %
50-40	1.217	15.886	13.057	92.9 %
40-30	2.241	36.701	16.375	94.2 %
30-20	5.071	90.254	17.800	94.7 %
20-10	8.430	138.818	16.466	94.3 %
10-5	8.034	118.232	14.717	93.6 %
5-0	8.326	102.565	12.319	92.5 %

varied. These results are presented in Section 9.3. The rapidity dependence ($y_{min} < y < 0$), y_{min} is varied from -0.2 to -0.9 with a transverse momentum range of $0.5 < p_T$(GeV/c) < 2.0.

4.7 Net-lambda Distribution

After the lambda reconstruction was performed and by using the centrality definition the event-by-event multiplicity distribution of net-lambda particles is performed. It should be noted that, compared to the previous net-lambda analysis [35], at $\sqrt{s_{NN}}$ = 3.0 GeV the antilambda to lambda ratio is of the order of 10^{-7}, therefore the amount of antilambda is negligible and the results in the lambda and net-lambda fluctuations are equivalent. The event-by-event multiplicity distribution of net-lambda is shown in Figure 37 for three different centralities; $0-5\%$, $20-30\%$ and $50-60\%$. It can be observed that the distributions are dominated by events without a lambda candidate. For most central collisions ($0-5\%$) an enhancement of lambda candidates is observed compared with more peripheral collisions ($50-60\%$), which leads to an increase in the width of the distribution.

Table 4: Track cuts used for the lambda reconstruction

Particle	Cut parameter	Cut boundary
Proton	Tranverse momentum	p_T(GeV/c) > 0.4
	$nHitsPoss$	≥ 5
	$nHitsFit$	≥ 15
	$nHitsFit/nHitsPoss$	≥ 0.52
	PID	$n\sigma < 3.0$
Pion	Tranverse momentum	p_T(GeV/c) > 0.15
	$nHitsPoss$	≥ 5
	$nHitsFit$	≥ 15
	$nHitsFit/nHitsPoss$	≥ 0.52
	PID	$n\sigma < 3.0$
Lambda	Tranverse momentum	$0.5 < p_T$(GeV/c) < 2.0
	Rapidity	$-0.5 < y < 0$
	Max. Lambda DCA to PV (cm)	1.0

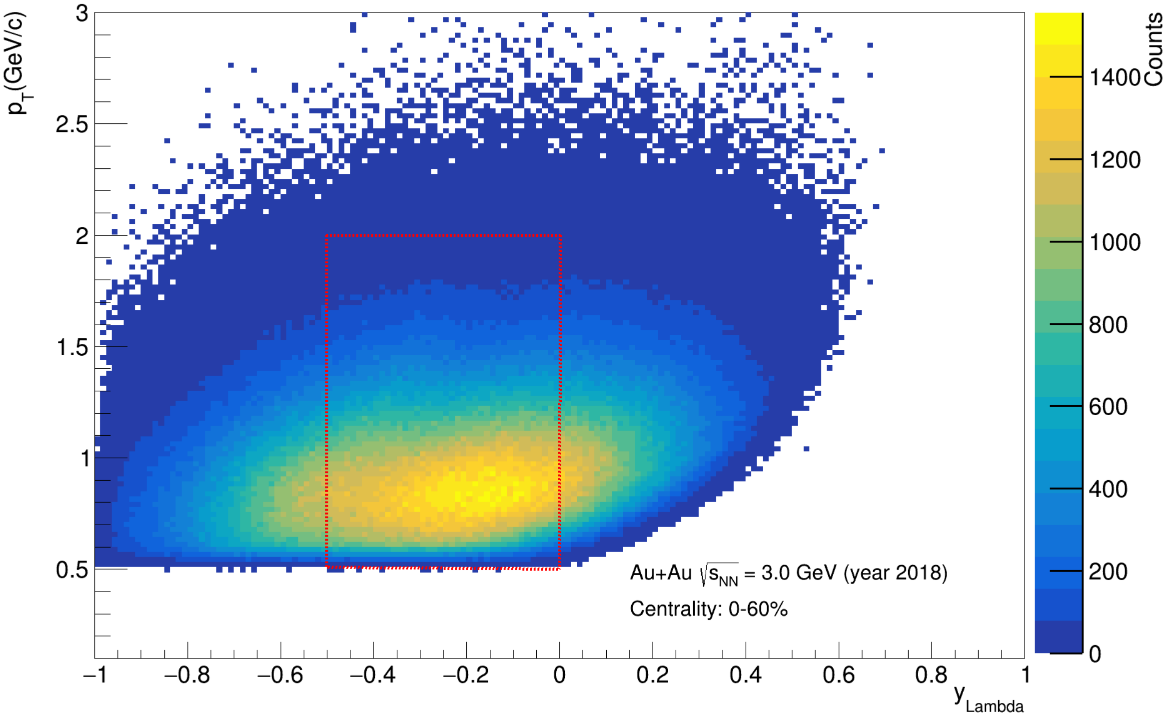

Figure 36: p_T and y of the lambda reconstruction. The red dashed line corresponds to the nominal cut boundary used in this analysis.

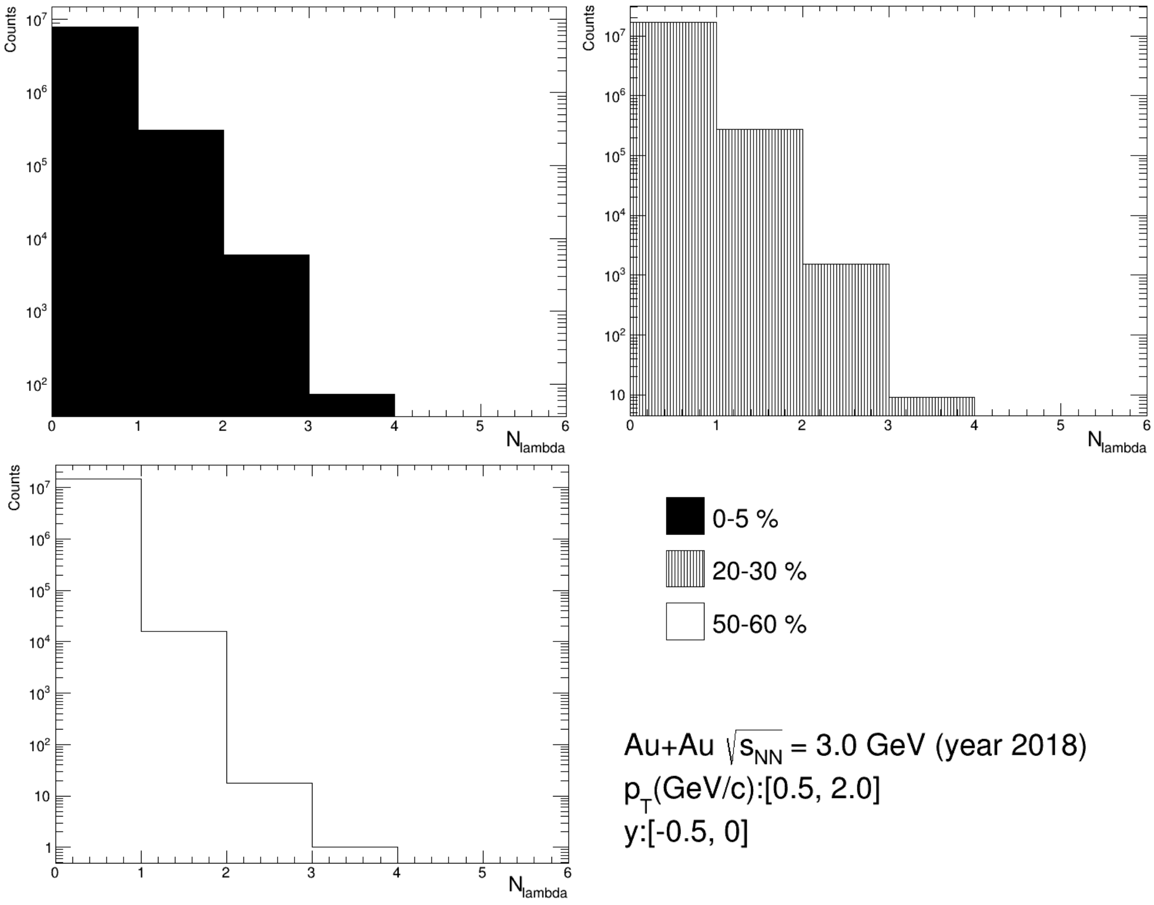

Figure 37: Event-by-event lambda multiplicity distribution for $\sqrt{s_{NN}} = 3.0$ GeV for three different centralities. Results are not corrected for reconstruction efficiency.

5 Cumulants and Correlation Functions

5.1 Moments and Cumulants

The present analysis is based on the counting of net-lambda on an event-by-event basis, as shown in Figure 37. By obtaining the multiplicity distribution of net-lambda, one can obtain the moments and cumulants of the distribution. As described briefly in Section 1.4.3, cumulants and moments of a probability distribution describe the shape of the distribution. Moments can be constructed by using the moment-generating function. Let N be a random variable of a normalized probability distribution $P(N)$. The moment generating function is given by:

$$M_N(t) = \sum_N e^{tN} P(N) = \langle e^{tN} \rangle \,. \tag{56}$$

By using the series expansion of e^{tN}, one can express $M_N(t)$ as:

$$M_N(t) = 1 + t \langle N \rangle + t^2 \frac{\langle N^2 \rangle}{2!} + t^3 \frac{\langle N \rangle^3}{3!} + ... + t^n \frac{\langle N^n \rangle}{n!} + ... \tag{57}$$

where the m^{th} raw moment μ'_m is computed by taking the m^{th} derivative of $M_N(t)$ and evaluate it at $t = 0$:

$$\mu'_m = M_N^{(m)}(0) = \frac{d^m M_N}{dt^m}\Big|_{t=0}. \tag{58}$$

For a probability distribution $P(N)$, in which N is an entry in the data sample, the raw moments are

$$\mu'_m = \langle N^m \rangle = \sum_N N^m P(N). \tag{59}$$

The central moments of a distribution are given by

$$\mu_m \equiv \langle (\delta N)^m \rangle = \sum_N (\delta N)^m P(n) \tag{60}$$

where $\langle N \rangle$ is the first moment and $\delta N = N - \langle N \rangle$ is the deviation from the mean value. Likewise, cumulants can be computed from a cumulant-generating function which is the natural logarithm of the moment generating function:

$$K_N(\theta) = \ln \langle e^{\theta N} \rangle . \tag{61}$$

Cumulants can be written in terms of the moments as

$$\begin{aligned} C_1 &= \langle N \rangle \\ C_2 &= \langle (\delta N)^2 \rangle = \mu_2 \\ C_3 &= \langle (\delta N)^3 \rangle = \mu_3 \\ C_4 &= \langle (\delta N)^4 \rangle - 3 \left\langle (\delta N)^2 \right\rangle^2 = \mu_4 - 3\mu_2^2. \end{aligned} \tag{62}$$

The explicit relation between the moments and cumulants is given by :

$$\begin{aligned} M(\text{Mean}) &= C_1 \\ \sigma^2(\text{Variance}) &= C_2 \\ S(\text{Skewness}) &= \frac{C_3}{C_2^{3/2}} \\ \kappa(\text{Kurtosis}) &= \frac{C_4}{C_2^2} \end{aligned} \tag{63}$$

Moments and cumulants are often interchangeable. In the case of a Poisson distribution, all cumulants are equal ($C_1 = C_2 = ... = C_i = \langle N \rangle$). Therefore, all cumulant ratios equate to one for a poissonian distribution.

5.2 Factorial Moments and Correlation Functions

In addition to moments and cumulants, in this analysis factorial moments and cumulants were used in the calculation of the efficiency correction (see Section 6) of cumulants and also as a measure of multiparticle correlations. The r^{th} factorial moment is define as:

$$\langle N^r \rangle_f = \langle N(N-1)(N_2)...(N-r+1) \rangle \tag{64}$$

similarly, the factorial cumulant is defined as

$$\langle N^r \rangle_{fc} = \langle N(N-1)(N-2)...(N-r+1) \rangle_c . \tag{65}$$

Like the moments and cumulants, the factorial moments and cumulants can be obtained by using a generating function given by:

$$\langle N^r \rangle_f = \frac{d^m M_f(s)}{ds^m}\Big|_{s=1}, \quad \langle N^r \rangle_{fc} = \frac{d^m K_f(s)}{ds^m}\Big|_{s=1} \tag{66}$$

where $K_f(s) = K(\ln)s$ and $M_f(s) = M(\ln s)$. Factorial cumulants can describe the multi-particle correlation functions κ_n. First, let us introduce the correlation function using the two particle density $\rho(p_1, p_2)$ for particles with momenta p_1 and p_2

$$\rho_2(p_1, p_2) = \rho(p_1)\rho(p_2) + \kappa_2(p_1, p_2) \tag{67}$$

where $\rho(p_1)$ is the one particle density, and $\kappa(p_1, p_2)$ represents the two particle correlation function. In general, the two particle density depends on the particle momentum of both particles. For simplicity, let us restrict to correlations in rapidity, with the following notation

$$\rho_2(y_1, y_2) = \int dp_{t,1} d\phi_1 dp_{t,2} d\phi_2 \rho_2(p_1, p_2) \tag{68}$$

$$\kappa_2(y_1, y_2) = \int dp_{t,1} d\phi_1 dp_{t,2} d\phi_2 \kappa_2(p_1, p_2) \tag{69}$$

$$\kappa_2 = \int dy_1 dy_2 \kappa_2(y_1, y_2) \tag{70}$$

and similarly for higher order particle densities and correlation functions. Integrating $\rho_2(p_1, p_2)$ from Eq. (67) over the momenta, we obtain

$$\langle N^2 \rangle_{fc} = \langle N(N-1) \rangle = \int dp_1 dp_2 \rho_2(p_1, p_2) = \langle N \rangle^2 + \kappa_2 \tag{71}$$

where N in this case corresponds to the number of lambdas and κ_2 is the integrated two-particle correlation function. Notice that, in the absence of correlations, $\kappa_2(p_1, p_2) = 0$, giving $\langle N^2 \rangle - \langle N \rangle^2 = \langle N \rangle$. This can be done for higher order particle densities as well, where the following relationships are obtained

$$\langle N^3 \rangle_f = \langle N \rangle^3 + 3 \langle N \rangle \kappa_2 + \kappa_3 \tag{72}$$

$$\langle N^4 \rangle_f = \langle N \rangle^4 + 6 \langle N \rangle^2 \kappa_2 + 4 \langle N \rangle \kappa_3 + 3\kappa_2^2 \kappa_4 \tag{73}$$

By using Eq. (65), the correlation functions are expressed in terms of cumulants as

$$\kappa_1 = C_1 \tag{74}$$

$$\kappa_2 = -C_1 + C_2 \tag{75}$$

$$\kappa_3 = 2C_1 - 2C_2 + C_3 \tag{76}$$

$$\kappa_4 = -6C_1 + 11C_2 - 6C_3 + C_4 \tag{77}$$

6 Detector Performance Corrections

In real experiments,the measured event-by-event lambda multiplicity distribution does not represent the true multiplicity distribution. The measurements are subject to efficiency and background effects and therefore not allowing the measurement to obtain the true multiplicity distribution $P(N)$. Certain corrections have to be applied to obtain the true multiplicity distribution ($P(N)$) from the measured multiplicity distribution($\tilde{P}(n)$). This section covers the efficiency correction techniques and the method to estimate the values of efficiencies of the Time Projection Chamber (TPC) detector.

6.0.1 Constant Efficiency Correction

For the lambda fluctuation analysis in the fixed target $\sqrt{s_{NN}} = 3.0$ GeV mode, the “track-by-track” efficiency correction was used [55], [56]. Let us start with the description of the simple efficiency correction, the constant efficiency correction. The technique applied for efficiency correction for the STAR detector assumes a binomial detector response, such that a detected track has an independent probability compared with adjacent detected tracks. Tests have been performed using non-binomial detector corrections [57] in order to compare it with the binomial correction. The effect was minimal and is diminished at lower collision energies [58]. In order to extract the true net-lambda multiplicity distribution $P(N)$, from the measured net-lambda distribution $\tilde{P}(n)$, one can define

$$\tilde{P}(n) = \sum_{N} P(N) B_{p,N}(n) \tag{78}$$

Where $B_{p,N}(n)$ is the binomial efficiency

$$B_{p,N}(n) = \frac{N!}{n!(N-n)!} p^n (1-p)^{N-n}. \tag{79}$$

The probability of detection is given by p, which is basically the efficiency of the detector. The measured number of net-lambdas is given by n. The efficiency correction can be written in terms of the factorial cumulants. The cumulant generating function of the net-lambda probability distribution is given by

$$K(\theta) = \ln \sum_N e^{N\theta} P(N) = \ln \langle e^{N\theta} \rangle \tag{80}$$

where the m^{th} order cumulant is defined as

$$\langle N^m \rangle_c = \frac{\partial^m}{\partial \theta^m} K(\theta)|_{\theta=0} \tag{81}$$

Likewise, the factorial cumulants are defined by changing $e^{N\theta} \to s^N$, which gives the cumulant generating function for factorial cumulants

$$K_f(s) = \ln \langle s^N \rangle \,. \tag{82}$$

With Eq. (82), one can evaluate the factorial cumulants

$$\langle N^m \rangle_{fc} = \frac{\partial^m}{\partial s^m} K(s) \Big|_{s=1}. \tag{83}$$

For the case of the measured factorial cumulants, the generating function is given by

$$\tilde{K}(s) = \ln \sum_n \tilde{P}(n) s^n = \ln \sum_N P(N) e^{\tilde{\kappa}_{p,N}(s)} \tag{84}$$

$$= \ln \sum_N P(N)(q - p + ps)^N \tag{85}$$

$$= K_f(1 + p(s-1)) \tag{86}$$

where

$$\tilde{\kappa}_{p,N}(s) = \ln \sum_n s^n B_{p,N}(n) = N \ln(1 - p + ps) \tag{87}$$

Like in Eq. (83), one can evaluate the factorial cumulant for the measured probability distribution $\tilde{P}(n)$ and relate it with the true factorial cumulant

$$\frac{\partial^m}{\partial s^m}\tilde{K}(s)|_{s=1} = p^m \frac{\partial^m}{\partial s^m}K(s)|_{s=1} \tag{88}$$

which is simplified to

$$\langle n^m \rangle_{fc} = p^m \langle N^m \rangle_{fc} \tag{89}$$

Therefore, by using factorial cumulants, the relation between measured and true distribution becomes trivial. With the use of the true factorial cumulants, one can convert it back to cumulants or moments. By using Eq. (89), one can construct the true cumulants of $P(N)$ in four steps:

1. Calculate the cumulants of $\tilde{P}(n)$.
2. Convert cumulants of $\tilde{P}(n)$ into factorial cumulants.
3. Calculate the factorial cumulants of $P(N)$ using factorial cumulants of $\tilde{P}(n)$ from Eq. (89).
4. Convert factorial cumulants of $P(N)$ into cumulants.

By following the procedure above, the cumulants of $P(N)$ are calculated:

$$\langle N \rangle_c = \langle N \rangle_{fc} = \frac{1}{p}\langle n \rangle_{fc} = \frac{1}{p}\langle n \rangle_c \tag{90}$$

$$\langle N^2 \rangle_c = \frac{1}{p^2}\langle n^2 \rangle_c + \left(\frac{1}{p} - \frac{1}{p^2}\right)\langle n \rangle_c \tag{91}$$

$$\langle N^3 \rangle_c = \frac{1}{p^3}\langle n^3 \rangle_c + \left(-\frac{3}{p} + \frac{3}{p^2}\right)\langle n^2 \rangle_c + \left(\frac{1}{p^3} - \frac{3}{p^2} + \frac{1}{p}\right)\langle n \rangle_c \tag{92}$$

$$\langle N^4 \rangle_c = \frac{1}{p^4}\langle n^4 \rangle_c + \left(-\frac{6}{p^4} + \frac{6}{p^3}\right)\langle n^3 \rangle_c + \left(\frac{11}{p^4} - \frac{18}{p^3} + \frac{7}{p^2}\right)\langle n^2 \rangle_c + \left(\frac{6}{p^4} + \frac{12}{p^3} - \frac{7}{p^2} + \frac{1}{p}\right)\langle n \rangle_c . \tag{93}$$

This method is effective but limited to the requirement of a constant efficiency, whereas in the STAR detector the efficiencies vary with p_T. Therefore, let us consider the multivariate efficiency bin correction.

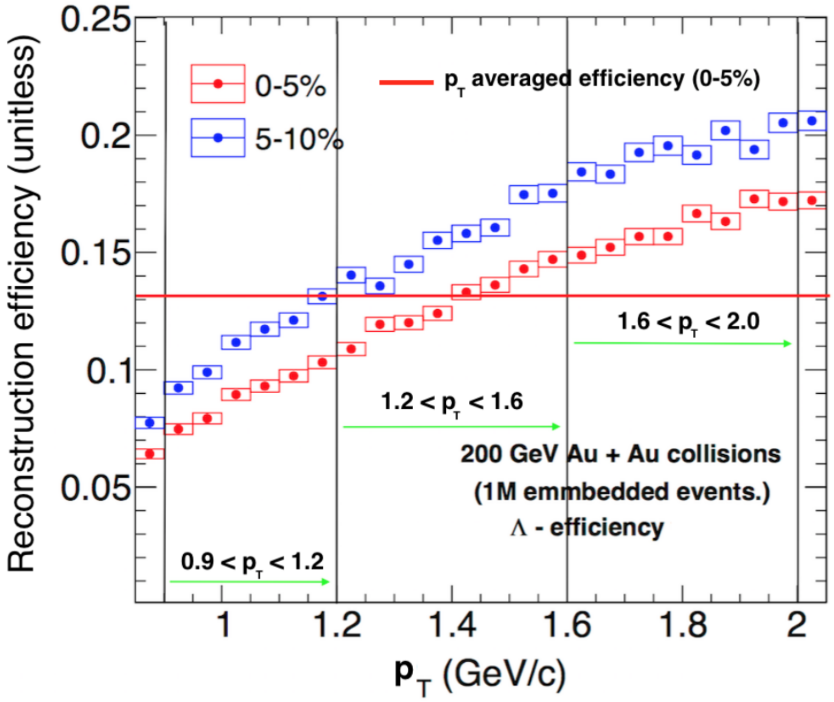

Figure 38: p_T dependence of reconstruction efficiency for $0-5\%$ central and $5-10\%$ central 200 GeV Au+Au collisions. Black vertical lines are the boundaries for three acceptance regions used in the corrections. Red horizontal line shows the equivalent p_T-averaged efficiency. Figure from [41].

6.0.2 Multivariate Efficiency Bin Correction

Consider now M discrete acceptance bins in which N_i number of particles enter the i^{th} acceptance bin. Therefore the distribution $P(N)$ corresponds to a multivariate distribution $P(\mathbf{N}) = P(N_1, N_2, ..., N_M)$. For the net-lambda analysis in the first beam energy scan (BES) at RHIC [35], a similar technique was used, with three discrete efficiency bins, one bin at low p_T, one at mid-values of p_T and one at high p_T, this can be seen in Figure 38. In the multivariate case, one can extract the true multiplicity distribution from the measured multiplicity distribution by assuming that the efficiency is now a product of binomial distributions. The measured probability distribution $\tilde{P}(\mathbf{n})$ is given by

$$\tilde{P}(\mathbf{n}) = \sum_{N} P(\mathbf{N}) \prod_{i=1}^{M} B_{p_i,N_i}(n_i) \tag{94}$$

where one can define the linear combination of particles and antiparticles of interest in the i_{th} efficiency bin as

$$Q_{(a)} = \sum_{i=1}^{M} a_i N_i \tag{95}$$

where $a = 1$ and $a = -1$ for particle and anti-particle, respectively. The corresponding cumulant generating function is defined in the multivariate case as

$$K(\boldsymbol{\theta}) = \ln\left[\sum_{\mathbf{N}} e^{\theta_1 N_1 + \ldots + \theta_M N_M} P(\mathbf{N})\right] \tag{96}$$

and the m^{th} order cumulant of Q_a is

$$\langle Q_{(a)}^{m} \rangle_c = \partial_{(a)}^{m} K(\theta)|_{\boldsymbol{\theta}=0} \tag{97}$$

with

$$\partial_{(a)} = \sum_{i=1}^{M} a_i \frac{\partial}{\partial \theta_i}. \tag{98}$$

In the case of the factorial cumulant, the generating function of the $P(\mathbf{N})$ is defined as

$$K_f(\mathbf{s}) = \ln\left[\sum_{\mathbf{N}} P(\mathbf{N}) \prod_{i=1}^{M} s_i^{N_i}\right] \tag{99}$$

and the factorial cumulants are defined as

$$\langle Q_{(a)} \rangle_{fc} = \bar{\partial}_{(a)}^{m} K_f(s)|_{s=1} \tag{100}$$

with

$$\bar{\partial}_{(a)} = \sum_{i=1}^{M} a_i \frac{\partial}{\partial s_i}. \tag{101}$$

With $s_i = e^{\theta_i}$, a similar relation between cumulants and factorial cumulants is derived

$$\langle Q_{(a)} \rangle = \partial_{(a)} K = \sum_{i=1}^{M} a_i \frac{\partial}{\partial \theta_i} K = \sum_{i=1}^{M} a_i \frac{\partial s_i}{\partial \theta_i} \frac{\partial}{\partial s_i} K_f = \bar{\partial}_{(a)} K_f = \langle Q_{(a)} \rangle_{fc} . \tag{102}$$

The factorial cumulant generating function of the product of binomial distributions can be written as

$$\tilde{K}_f(\mathbf{s}) = \ln \sum_{\mathbf{N}} P(\mathbf{N}) \prod_{i=1}^{M} (1 + p_i(s_i - 1))_i^N = K_f(\mathbf{s}') \tag{103}$$

where $s'_i = 1 + p_i(s_i - 1)$. Finally, one obtains the version of Eq. (89), which relates the multivariate cumulants to the multivariate factorial cumulants

$$\bar{\partial}_{(a)} K_f = \bar{\partial}_{(a/p)} \tilde{K}_f . \tag{104}$$

Therefore, one can calculate the cumulants of the true distribution $P(\mathbf{N})$ with cumulants of the measured distribution $\tilde{P}(\mathbf{n})$ as follows

1. Calculate the cumulants of $\tilde{P}(\mathbf{n})$
2. Convert the cumulants of $\tilde{P}(\mathbf{n})$ into factorial cumulants.
3. Convert the factorial cumulants of $\tilde{P}(\mathbf{n})$ into factorial cumulants of $P(\mathbf{N})$ with the efficiency of the p^i efficiency bin.
4. Convert the factorial cumulants of $P(\mathbf{N})$ into cumulants.

The cumulants expressed as measured cumulants up to the third order are shown below

$$\begin{aligned}
\left\langle Q_(a) \right\rangle_c &= \left\langle Q_{(a)} \right\rangle_{fc} = \left\langle q_{a/p} \right\rangle_{fc} = \left\langle q_{(a/p)} \right\rangle_c && (105) \\
\left\langle Q^2_{(a)} \right\rangle_c &= \left\langle Q^2_{(a)} \right\rangle_{fc} + \left\langle Q_{(a^2)} \right\rangle_{fc} = \left\langle q^2_{(a/p)} \right\rangle_{fc} + \left\langle q_{(a^2/p)} \right\rangle_{fc} \\
&= \left\langle q^2_{(a/p)} \right\rangle_c - \left\langle q_{(a^2/p^2)} \right\rangle_c + \left\langle q_{(a^2/p)} \right\rangle_c && (106) \\
\left\langle Q^3_{(a)} \right\rangle_c &= \left\langle Q^3_{(a)} \right\rangle_{fc} + 3 \left\langle Q_{(a)} Q_{(a^2)} \right\rangle_{fc} + \left\langle Q_{(a^3)} \right\rangle_{fc} \\
&= \left\langle q^3_{(a/p)} \right\rangle_{fc} + 3 \left\langle q_{(a/p)} q_{(a^2/p)} \right\rangle_{fc} + \left\langle q_{(a^3/p)} \right\rangle_{fc} \\
&= \left\langle q^3_{(a/p)} \right\rangle_c - 3 \left\langle q_{(a/p)} q_{(a^2/p^2)} \right\rangle_c + 2 \left\langle q_{(a^3/p^3)} \right\rangle_c + 3 \left(\left\langle q_{(a/p)} q_{(a^2/p)} \right\rangle_c - \left\langle q_{(a^3/p^2)} \right\rangle_c \right) \left\langle q_{(a^3/p)} \right\rangle_c \\
& && (107)
\end{aligned}$$

where, $q_{(a)}$ is defined as

$$q_{(a^r/p^s)} = \sum_{i=1}^{M} \frac{a_i^r}{p_i^s} n_i. \tag{108}$$

where p_i is the efficiency on the i^{th} acceptance bin and n_i is the number of measured particles in the i^{th} acceptance bin. Although the multivariate efficiency correction method is an improvement over the constant efficiency method, it can still fail to characterize efficiency distributions that vary drastically [56]. Figure 39 shows a toy simulation testing the multivariate efficiency bin correction. To model a detector with different levels of effectiveness, 50 separate binomial distributions were created and applied to simulated events. By using the multivariate efficiency technique, the cumulants are calculated for different M averaged efficiency bins (x-axis). The simulation shows that a minimum 50 efficiency bins ($M = 50$) is necessary to accurately reproduce the true cumulants. The multivariate efficiency method works well for high number of bins but it requires the number of net-particles in each bin M. An improved method was proposed, where the number of net-particle in the bin is not required. This method is discussed in the following section.

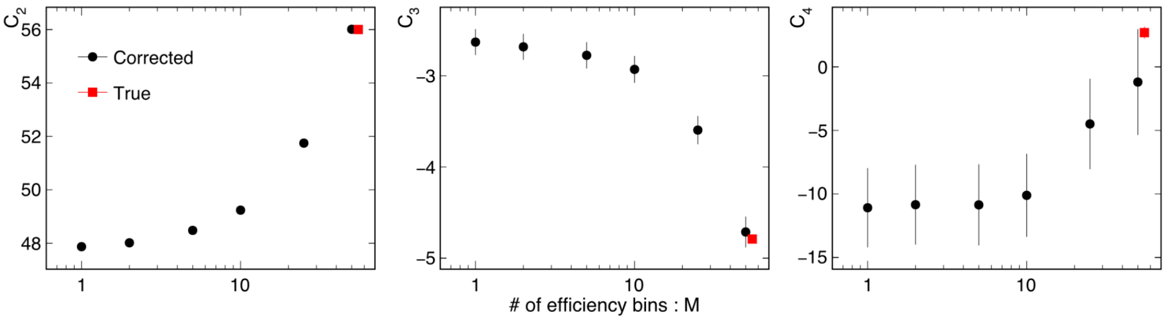

Figure 39: Toy simulation to test the multivariate efficiency bin correction. Figure from [56].

6.0.3 "Track-by-track" Efficiency Correction Method

In the multivariate case, the efficiency bins are assumed to have a finite bin size and each bin is weighted by the number of net-particles n. In the "track-by-track" correction, the bin size is made to be infinitesimal ($M \to \infty$) and the number of net-particles in each bin ends up to be either $n_i = 0$ or $n_i = 1$. Therefore, the sum in Eq. (108) is simplified, as the sum only considers efficiency bins in which a particle is measured and $n = 1$. The efficiency corrected raw moment is given by

$$q_{(a^r/p^s)} = \sum_{i=1}^{O} \frac{a_i^r}{p_i^s} \tag{109}$$

where O is the total measured number of particle/anti-particle yield and p_i is the efficiency at a given rapidity and momentum. The procedure to calculate the cumulants using the "track-by-track" method is the same as the one described for the multivariate method. The advantage of the "track-by-track" method is that it does not require the particle spectra to properly weigh the finite efficiency bins, since the method assumes at maximum one particle per infinitesimal bin and the efficiency is calculated directly from embedding efficiency curves which are shown in Figure 42.

6.1 TPC Efficiency

6.1.1 Embedding

In order to calculate the TPC efficiency in the STAR detector, the collaboration relies on detector simulations. The STAR detector is modeled using a detector framework capable of simulating the passage of particles through matter, GEANT3. The simulated tracks are passed through the GEANT3STAR model, which generates TPC pad positional and dE/dx data. The simulated event is embedded into real event data and both the simulated and real detector event hits are reconstructed to generate the TPC tracks. This process of simulating tracks and embed them into real data is called "embedding". By using the embedded reconstructed data, one can calculate the fraction of simulated tracks that were able to be reproduced. For the case of the lambda embedding data, the simulated tracks were generated using a uniform p_T : $[0, 3]$ GeV/c and η : $[-2, 0]$ distribution, 2.5 millions of events were used, in which 5% of the reference multiplicity were Monte Carlo tracks per event. Lambda particles were reconstructed using the same track quality, topological and purity of the particle identification parameters as used in data. This is done in order to account for the loss in efficiency when tight cuts are used, Section 7.2 present a discussion of the cuts used in the analysis. The respective rapidity (y) in the lambda center of mass was calculated, which ranges from $y : [-1, 1]$ corresponding to a pseudo-rapidity of $\eta : [-2, 0]$ in the detector. The generated and reconstructed lambda particles are shown in Figure 40, which is shown as a function of p_T and y_{lambda} which is the rapidity in the lambda reference frame. Additionally, the multiplicity of the real events is varied to study the efficiency as a function of centrality. Figure 40 shows the generated and reconstructed tracks in the mentioned region, the efficiency is calculated by taking the ratio between the reconstructed and the generated lambdas ($Eff = Rec/Gen$) in a particular bin.

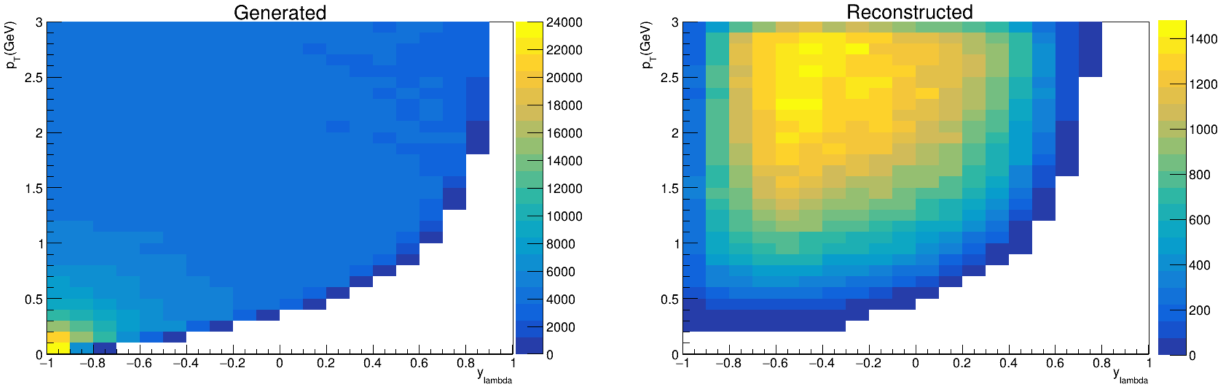

Figure 40: Left panel: Generated lambda tracks for $0-5\%$ centrality. Right panel: Reconstructed tracks for $0-5\%$ centrality

6.2 Lambda TPC Efficiency for Au + Au collisions at $\sqrt{s_{NN}} = 3.0$ GeV

In order to apply the “track-by-track” efficiency correction on the cumulants, the embedding sample has to be finely binned in the transverse momentum and rapidity. The single track efficiency correction was applied in the proton fluctuation analysis at STAR [59] where a fine binning was used, due to the high number of proton tracks produced in an event. In the case of lambda particles at $\sqrt{s_{NN}} = 3.0$ GeV, the amount of produced lambdas in an event can be 100 times less than in the case of protons, therefore the binning used for this analysis is half of the number of bins used in the proton analysis. This is done in order to obtain values of efficiencies per bin with small statistical uncertainties. The efficiency at a given transverse momentum and rapidity bin is calculated by dividing the number of reconstructed lambdas from the Monte Carlo tracks by the total simulated Monte Carlo lambdas as it can be observed in the 2D efficiency map in Figure 41. The number of bins in p_T were 30 and 20 in y.

6.2.1 Rapidity Slice Fitting Procedure

The 2D efficiency plot as a function of rapidity and transverse momentum is shown in Figure 41 for most central collisions. To reduce statistical fluctuations, the 2D histogram is divided into

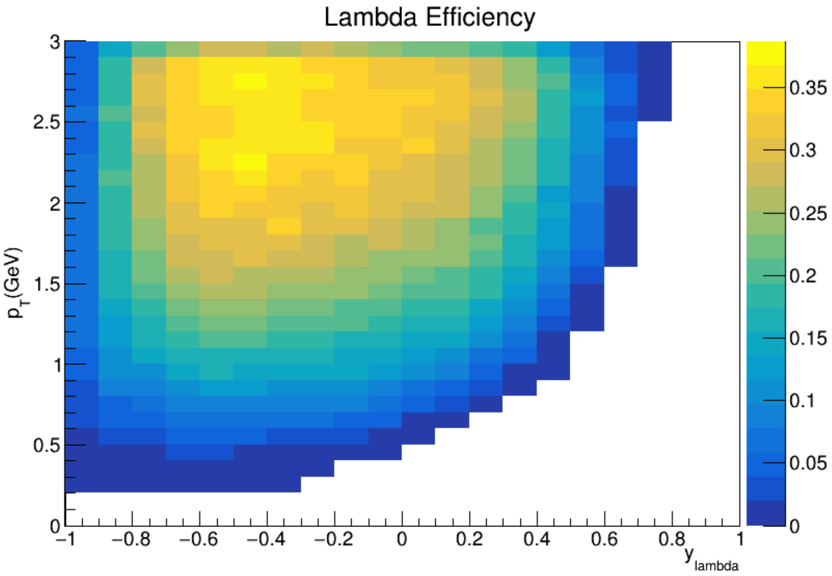

Figure 41: 2D efficiency map for lambda particles.

20 rapidity slices and then projected on to a 1D histogram for each particular slice, which is the efficiency as a function of transverse momentum. Then, each 1D histogram is parameterized by an exponential + 2^{nd} order polynomial function. Figure 42 shows the

$$f(x) = p_1 e^{-p_2/x} + p_3 x + p_4 x^2. \tag{110}$$

The first term of the fitting function, the exponential $p_1 e^{-p_2 x}$, is motivated by the fast increase of the efficiencies with increasing p_T, as seen in Figure 42. The last two terms $p_3 x$ and $p_4 x^2$, are motivated to capture the small increase at $p_T > 2.0$ GeV. As it can be observed in Figure 42, the fits does not to describe the data accurately at values of $p_T \gtrsim 2.5$ GeV, but for this analysis the maximum value of p_T considered is at $p_T = 2.0$ GeV. The reason of rejecting higher p_T bins is due to the fact that in data there is no contribution of lambda tracks above $p_T = 2.0$ GeV, which means that the efficiency correcting method cannot correct the measured multiplicity if there are no lambda tracks.

For the previous analyses of lambda fluctuations for the BES-I, a sizeable anti-correlation between the total particle multiplicity and the detector efficiency was found. This anti-correlation

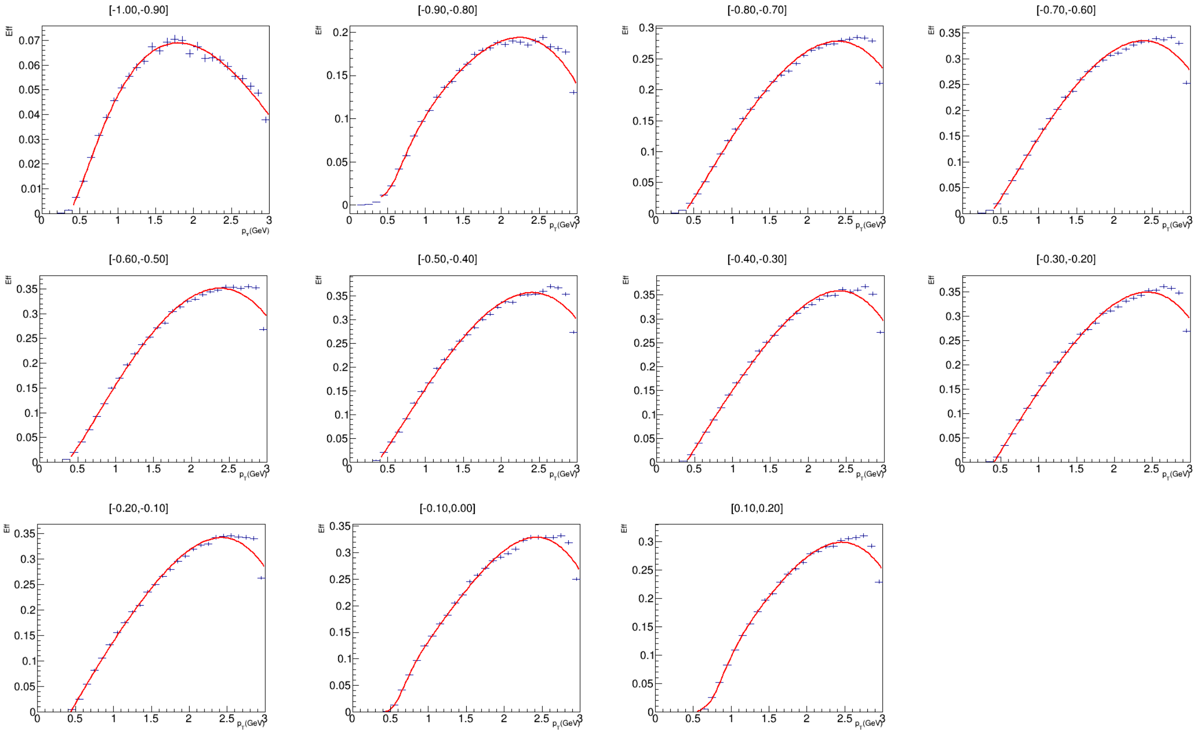
[-1.00,-0.90]
[-0.90,-0.80]
[-0.80,-0.70]
[-0.70,-0.60]
[-0.60,-0.50]
[-0.50,-0.40]
[-0.40,-0.30]
[-0.30,-0.20]
[-0.20,-0.10]
[-0.10,0.00]
[0.10,0.20]

Figure 42: Plot of rapidity slices of TPC detector efficiency with exponential + 2nd order polynomial fits. Label on top of each sub-panel represents the rapidity slice in the y_{lambda}.

effect is due to the high track densities, the TPC gas volume saturates leading to gas occupancy effects causing the efficiency to decrease considerably. The number of track multiplicities increases with the center of mass energy $\sqrt{s_{NN}}$, therefore the occupancy effects observed in the efficiency scales with energy. At the lowest center of mass energy achieved $\sqrt{s_{NN}} = 3.0$ GeV, the occupancy effects diminish considerably in the case of protons, where the efficiency varies less than 5% from highest to lowest centrality (0-5 % to 50-60 %) as it can be observed in Figure 43. These deviations are considered in studies of the systematic uncertainties, taking into account a ±5% systematic variation in the bin-by-bin efficiency. In the case of lambda, Figure 44 shows the TPC detector efficiency in an integrated rapidity from $-0.9 < y < 0$, for three centralities, $0-5\%$, $30-40\%$ and $50-60\%$. As can be observed for values $p_T > 1.5$ GeV, the efficiencies start showing sizable deviations for different centralities. In order to consider this deviation, an efficiency average for the centrality $0-60\%$ is used and a variation of ±10% in the efficiency value in a particular efficiency bin is included in the systematic studies.

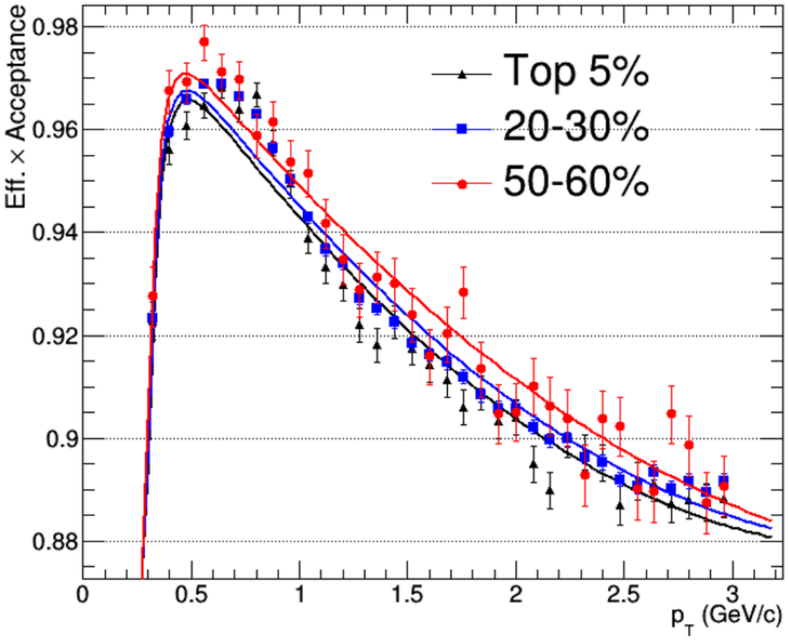

Figure 43: Comparison of proton TPC efficiency as a function of p_T for three centrality classes, integrated from $-0.9 < y < 0.1$. Figure from [39].

6.3 Methodology of the Efficiency Correction Applied to Cumulants

By using the "track-by-track" efficiency correction discussed in Section 6.0.3 and by using the efficiency curves from Section 6.2.1, the efficiency-corrected cumulants are calculated following the procedure

1. Events from the $\sqrt{s_{NN}} = 3.0$ GeV are looped.
2. By using a kinematic acceptance window the lambda candidates are considered in each event.
3. By selecting a mass window corresponding to the lambda signal in each event a lambda "track" is considered.
4. The collection of lambda "tracks" is considered to calculate $q_{(a^r/p^s)} = \sum_{i=1}^{M}(a_i^r/p_i^s)n_i$, in

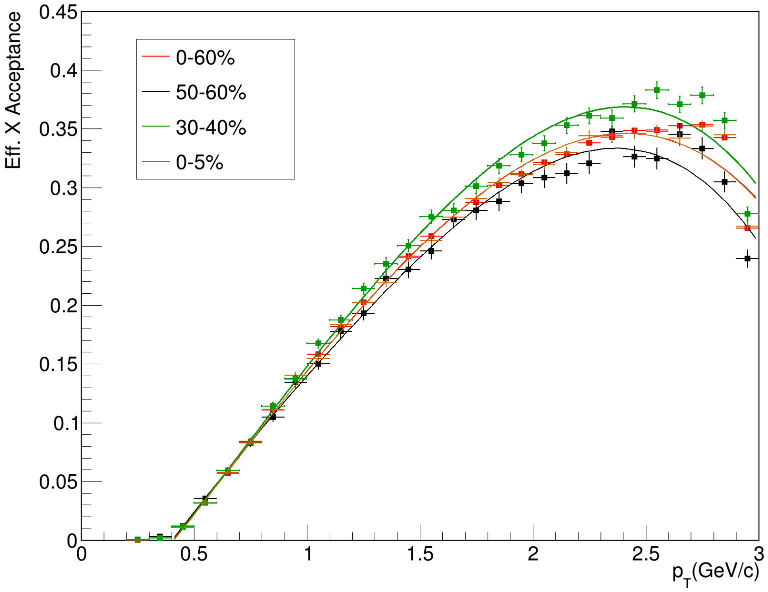

Figure 44: Comparison of lambda TPC efficiency as a function of p_T for three centrality classes, integrated from $-0.9 < y < 0$.

which $a = \pm 1$ for lambda/anti-lambda and p which corresponds to the track efficiency at a given y and p_T.

5. Average the event-by-event $q_{(a^r/p^s)}$ and calculate the cumulants with the procedure from Section 6.0.2.

The corrected results using the "track-by-track" efficiency correction method are shown in Figure 45 and Figure 46, along with the uncorrected cumulants and cumulant ratios.

As shown in Figure 45, the single cumulants increased in magnitude by a large factor after the efficiency correction was applied. However, for the cumulant ratios there is little change with the exception of C_4/C_2, where deviations from the uncorrected case start to be noticeable due to the sensitivity in high order cumulants and the higher order correcting terms that are applied with increasing order of the cumulant, see Figure 46.

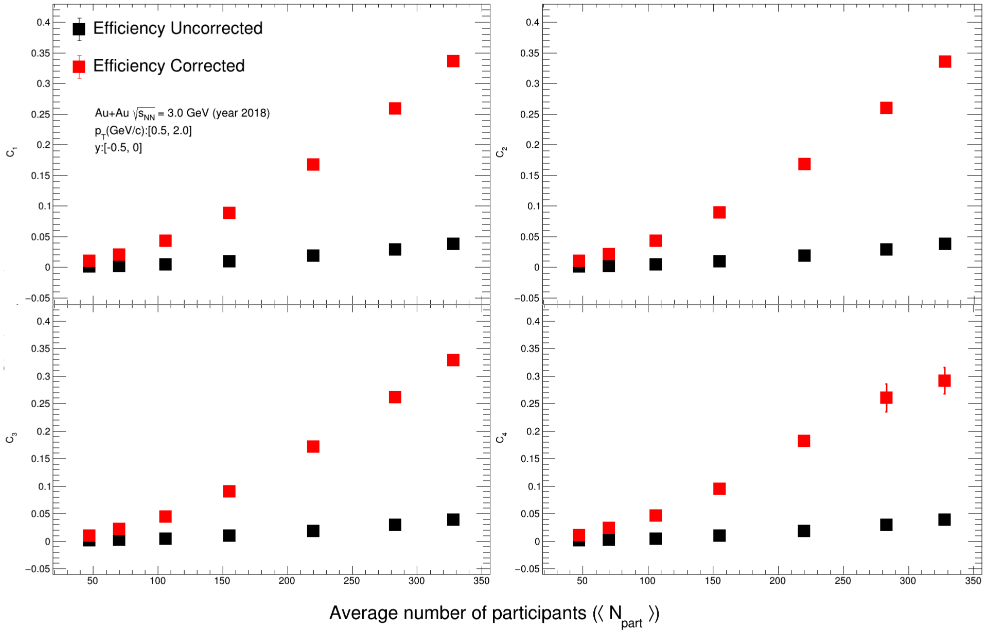

Figure 45: Comparison between efficiency corrected and uncorrected cumulants: C_1, C_2, C_3 and C_4 as a function of average number of participant nucleons $\langle N_{Part} \rangle$. Results were corrected for CBWE. Only statistical errors are presented.

6.4 Volume Fluctuation Effects

As discussed in Section 3.4, centrality cannot be measured directly. It is determined by comparing the produced charged particle multiplicity to Glauber model simulations. The effects of centrality bin determination are potentially the centrality bin-width effect (CBWE). Results of fluctuations of multiplicity distributions are often presented using wide centrality bins. Variations in the finite centrality bin width can cause effects on the results. In order to eliminate the effects of the finite centrality bin width, the observable is weighted by the number of events within the centrality bin as shown in Eq. (111).

$$X = \frac{\sum_i n_i X_i}{\sum_i n_i} \tag{111}$$

where n_i and X_i are the number of events and the observable in the $i-th$ multiplicity bin, where i spans the multiplicity bin in a centrality class.

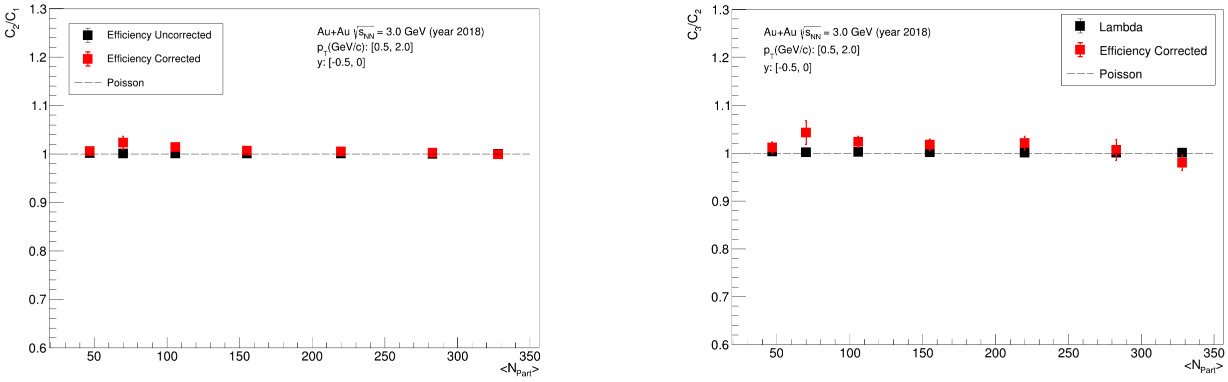

(a) C_2/C_1 (b) C_3/C_2

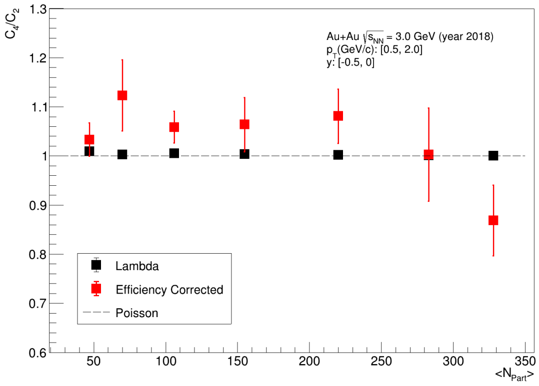

(c) C_4/C_2

Figure 46: Comparison efficiency corrected and uncorrected cumulant ratios as a function of $\langle N_{Part} \rangle$. Results were corrected for CBWE. Only statistical errors are presented.

7 Estimation of Uncertainties:

7.1 Statistical Uncertainty Estimation

For the BES-I, the data for the lowest center of mass energies used were taken in the collider mode, which suffered from low statistics and only around three and seven million of events were used for the $\sqrt{s_{NN}} = 7.7$ GeV and $\sqrt{s_{NN}} = 11$ GeV, respectively. Due to the low statistics, analyzers considered different methods to calculate statistical uncertainties. Three different methods were proposed: the Delta theorem, sub-sample and the Bootstrap method. For the lamba fluctuation analysis at $\sqrt{s_{NN}} = 3.0$ GeV, the Bootstrap method was implemented due to its simplicity. The Delta theorem was also used for the statistical uncertainties of transport models that are compared with data. Therefore in this section, we only describe the Delta theorem [60] and the Bootstrap method [61].

7.1.1 Delta Theorem

The Delta theorem allows to approximate an uncertainty by transforming a distribution with a known uncertainty. The delta theorem allows to calculate an analytical expression for the uncertainties of the cumulants and the cumulant ratios [60]. In order to state the Delta theorem, let us consider the central limit theorem (CLT).

Central Limit Theorem: Let $X_1, ..., X_n$ be a random sample of size n, where n is a sequence of identically distributed random variables from a distribution with $\mu < \infty$ and $\sigma^2 < \infty$. As $n \to \infty$, the difference between sample average $\langle X \rangle = (X_1 + ... + X_n)/n$ and μ when multiplied by $\sqrt{n}$ approximates to a normal distribution with $\langle X \rangle = 0$ and variance σ^2

$$\sqrt{n}(\langle X \rangle - \mu) \xrightarrow{d} N(0, \sigma^2). \tag{112}$$

From the CLT, the Delta theorem states: If there is a sequence of random variables X_n that satisfies Eq. (112), then

$$\sqrt{n}(g(\langle X\rangle) - g(\theta)) \xrightarrow{d} N(0, \sigma^2 \cdot g'(\theta)^2) \tag{113}$$

for any function g, where $g'(\theta)$ exists and is non-zero valued. It is know from [60] that, if the central moments $\mu_{2k} = \langle(X-\mu)^{2k}\rangle < \infty$, then the random vector $\sqrt{n}(\tilde{\mu_2} - \mu_2, ..., \tilde{\mu_k} - \mu_k)$ converges in distributions to $(k-1)$-variate normal with mean vector $(0, ..., 0)$ and the covariance matrix $[\sum_{ij}]_{(k-1)\times(k-1)}$, where

$$\sum_{ij} = \mu_{i+j} - \mu_i\mu_j - i\mu_{i-1}\mu_{j+1} - j\mu_{i+1}\mu_{j-1} + ij\mu_{i-1}\mu_{j-1}\mu_2. \tag{114}$$

With Eq. (114) and the Delta theorem, the limiting distribution central moments transformed by a function g can be calculated. For example, using Eq. (114), the limiting distribution of the sample variance is

$$\hat{\sigma} \xrightarrow{d} N(\sigma^2, \frac{\mu_4 - \sigma^4}{n}). \tag{115}$$

To calculate the limit distribution of the standard deviation $\hat{\sigma}$, one can define the function $g(x) = \sqrt{x}$. Applying the Delta theorem, the limit distribution is

$$\hat{\sigma} \xrightarrow{d} N(\sigma, \frac{\mu_4 - \sigma^4}{4\sigma^2 n}). \tag{116}$$

Multivariate Delta Theorem: In order to calculate the statistical uncertainties for the cumulants and cumulant ratios, it is required to use the multivariate case of the Delta theorem. Consider $\boldsymbol{X} = \{X_1, ..., X_n\}$ is normally distributed as $N(\mu, \sigma/n)$, where Σ is a covariance matrix. Let $\boldsymbol{g(x)} = (g_1(x_1), ..., g_m(x_k))$, where $\boldsymbol{x} = (x_1, ..., x_k)$, a vector-valued function. Each component function $g_i(x)$ is real valued and has a non-differentiable $g_i(\mu)$, at $\boldsymbol{x} = \mu$. With the use of the

Jacobian determinant

$$\boldsymbol{D} = \left[\frac{\partial g_i}{\partial x_j} \Big|_{x=\mu} \right] \tag{117}$$

the approximate statistic can be calculated as

$$\boldsymbol{g(X)} \xrightarrow{d} N(\boldsymbol{g}(\mu), \frac{\boldsymbol{D\Sigma D'}}{n}) \tag{118}$$

To calculate the standard error on cumulants or cumulant ratios, one can define a random sample moments vector as

$$\hat{T} = \begin{pmatrix} \hat{u_2} \\ \hat{u_3} \\ \hat{u_4} \end{pmatrix} \xrightarrow{d} N \left(\begin{pmatrix} u_2 \\ u_3 \\ u_4 \end{pmatrix}, \frac{\boldsymbol{\Sigma}}{n} \right) \tag{119}$$

where $\boldsymbol{\Sigma}$ is defined in Eq. (114). With Eq. (118), the sample error of the transformed random vector can be calculated. The calculated variances of the cumulant ratios C_3/C_2 and C_4/C_2 are

$$\mathrm{Var}(C_3/C_2) = (9 - 6\mu_4 + \mu_3^2(6 + \mu_4) - 2\mu_3\mu_5 + \mu_6)\sigma^2/n \tag{120}$$

$$\mathrm{Var}(C_4/C_2) = (-9 + 6\mu_4^2 + \mu_4^3 + 8\mu_3^2(5 + \mu_4) - 8\mu_3\mu_5 + \mu_4(9 - 2\mu_6) - 6\mu_6 + \mu_8)\sigma^4/n \tag{121}$$

7.1.2 Bootstrap Method

In the bootstrap method [62], the variance of the sample distributions is used to estimate the statistical uncertainty. B number of statistical samples are generated and each sample size is equivalent to the data set. The samples are generated by randomly selecting events. Consider a sample X, where the measurement is $\hat{e}$, the procedure for the error calculation is the following:

1. Given a parent sample size N, create B number of independent bootstrap samples $X_1, ..., X_B$, each sample containing n data points randomly drawn with replacement from the parent sample.

2. The estimator(measurement) of each bootstrap sample is calculated, $\hat{e}_b = \hat{e}(X_b)$ for $b = 1, ..., B$.

3. The sample variance of the estimator is given by
   $\text{Var}(\hat{e}) = \frac{1}{B-1} \sum_{b=1}^{B} (\hat{e}_b - \bar{\hat{e}})^2$, where $\bar{\hat{e}} = \frac{1}{B} \sum_{b=1}^{B} (\hat{e}_b)$.

Studies have shown [62] that the number of boostraps that show agreement between the Delta theorem and boostrap method is when $B > 1000$. Both methods agree at 1% level if the number of bootstraps is increased significantly ($B > 10000$). For the lambda fluctuation analysis at $\sqrt{s_{NN}} = 3.0$ GeV, the Bootstrap method is the selected uncertainty estimator technique. The reason of choosing the Bootstrap method instead of the Delta theorem is the naturally propagation through the cumulant corrections and most importantly is that the Delta theorem requires to calculate the μ_{2n} of the n^{th} highest moment. This is problematic as background and efficiency corrections become more difficult at higher orders. After tests of different values of bootstrap samples it was observed that increasing the number of bootstraps for values greater than $B = 50$ did not change the magnitude of the uncertainties, therefore $B = 50$ number of bootstraps was used in order to reduce the computational demand in the calculation.

7.2 Estimation of Systematic Uncertainties:

The systematic uncertainty of the cumulants and correlation functions of net-lambda fluctuation at $\sqrt{s_{NN}} = 3.0$ GeV is subdivided into four categories: uncertainty associated with the efficiency corrections, particle identification, track quality and reconstruction of V^0. Detector imperfections are addressed to some level in the efficiency corrections using the procedure explained in Section 6. The uncertainty associated with the selection process used for the identification of charged particles is studied by varying the $n\sigma$ for each charged particle, which uses the ionization energy loss to identify charge particles in the TPC, as seen in Figure 18. The purity of the samples depends on the particle identification (PID) cuts. Different topological cuts were used for the reconstruction of V^0s, varying the cuts change the signal and the background of the V^0s, the different cuts and properties are shown in Section 4.5. The different cuts affected the purity of the sample and the reconstruction efficiency as a well. Therefore, variations of the topological cuts were included as a source for systematic uncertainty estimation. Additionally, the uncertainties in the reconstruction efficiency were included as a source for systematic uncertainties. The sources and variations are listed in table 5. The root mean square (RMS) value for each cut variation for cumulants and correlation functions as a function of centrality is shown in Figure 48 and Figure 50, respectively. RMS for each cut variation for cumulants and correlation functions as functions of rapidity window (Δy) are shown in Figure 52 and Figure 54, respectively. The calculation of the systematic uncertainty was done by using Equations (122) and (123) by considering the contribution from all potential sources mentioned above. The results are corrected for reconstruction efficiency for each cut-set variation. Then, the point by point difference between the results from each cut selection and the default value is calculated. The RMS for each cut is calculated using Eq. (122), where N stands for the number of different cuts used in a certain cut variation, X_i, corresponds to the results from a particular cut set, and Y corresponds to the default result. The systematic uncertainty is calculated from Eq. (123), where j stands for the number of sources used in the error estimation,

$$RMS = \sqrt{\frac{1}{N}\sum_{i=1}^{N}(X_i - Y)^2} \tag{122}$$

$$SysError = \sqrt{\sum_j RMS_j^2}. \tag{123}$$

The main source of systematic uncertainty is the selection criteria used in the identification of protons and pions ($n\sigma$). It has a relative contribution of 48.2% to the systematic uncertainty in C_3/C_2 for $0-5\%$ central collisions. The second largest contribution comes from the topological cut variations. The contribution of the variation in efficiencies on the systematic error was relatively small, as seen in Table 5.

7.2.1 Systematic Variations as a Function of $\langle N_{Part} \rangle$

Figure 47 and Figure 49 show the comparison of the cumulant ratios and factorial cumulant ratios for different sources as a function of $\langle N_{Part} \rangle$. It can be observed in Figure 48 that for most central collisions the main source of systematic uncertainty is due to the particle identification ($n\sigma$), similarly the topological variations contribute considerably to the source of uncertainty in most central and most peripheral collision. The reason of the contribution for most peripheral collisions in the case of the topological variations is due to the decrease of lambda tracks and the effects of the tight topological cuts. The effect of the track quality and efficiency variations are small for most centralities. In general, systematic uncertainties for all sources increase with increasing order of the cumulant ratio. Figure 50 shows that the effect of topological variations is stronger in most central collisions and in most peripheral collisions. It can be observed that the quality of the tracks contributes considerably in most central collisions but the least in most peripheral collisions, this is due to the fact that more tracks are produced in most central collisions which represents difficulties to recognize good tracks from broken tracks. Variations in efficiencies contribute the least to the systematic uncertainty.

Table 5: Sources of the systematic uncertainty, their variations and the contribution for the systematic error. Relative contributions are calculated in the most central collisions($0-5\%$) of C_3/C_2

Source	Variation	Contribution
Topological cuts	$\chi^2_{prim} > 15$, $\chi^2_{topo} < 5$, $\chi^2_{NDF} < 5$ (standard) $\chi^2_{prim} > 10$, $\chi^2_{topo} < 5$, $\chi^2_{NDF} < 5$ $\chi^2_{prim} > 12$, $\chi^2_{topo} < 5$, $\chi^2_{NDF} < 5$ $\chi^2_{prim} > 5$, $\chi^2_{topo} < 7$, $\chi^2_{NDF} < 5$ $\chi^2_{prim} > 7$, $\chi^2_{topo} < 10$, $\chi^2_{NDF} < 6$	42.5%
$n\sigma(\pi)$ and $n\sigma(p)$	< 3.0 & 3.0 (default) < 2.5 & 2.5 < 2.0 & 2.0	48.2%
nHitsFit	> 15 (default) > 12 > 10	6.1%
Efficiency(lambda)	ε (default) $\varepsilon \times (1 + 10\%)$ $\varepsilon \times (1 - 10\%)$	3.2%

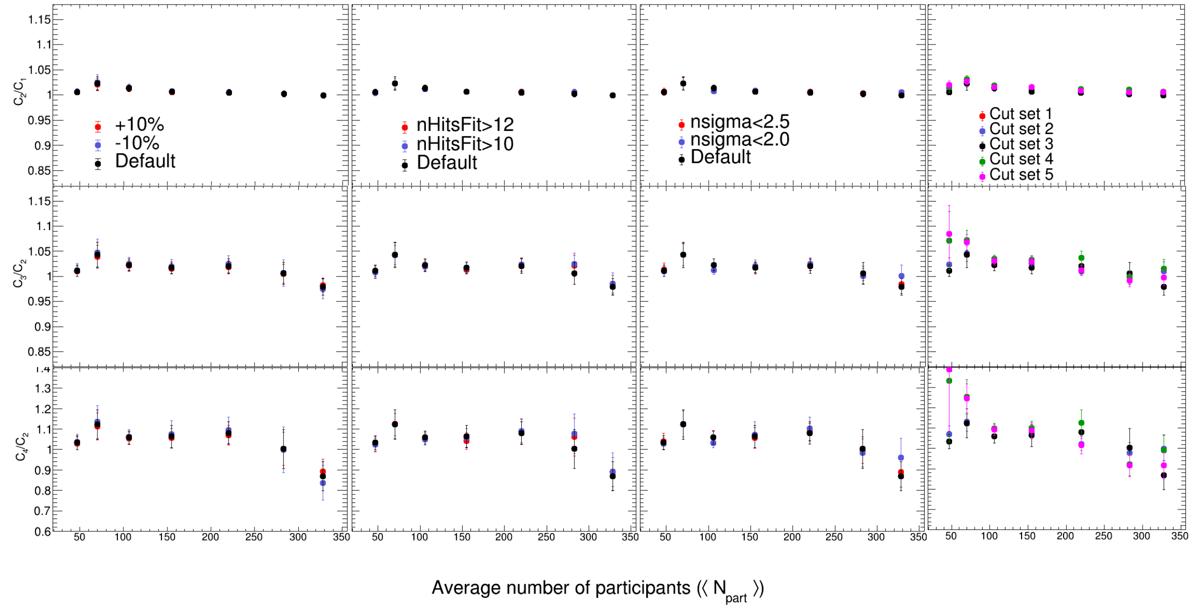

Figure 47: Effect of cut parameter variations and efficiency variation on the efficiency corrected net-lambda *cumulant ratios* as a function of *centrality* at $\sqrt{s_{NN}} = 3.0$ GeV Au+Au collisions.

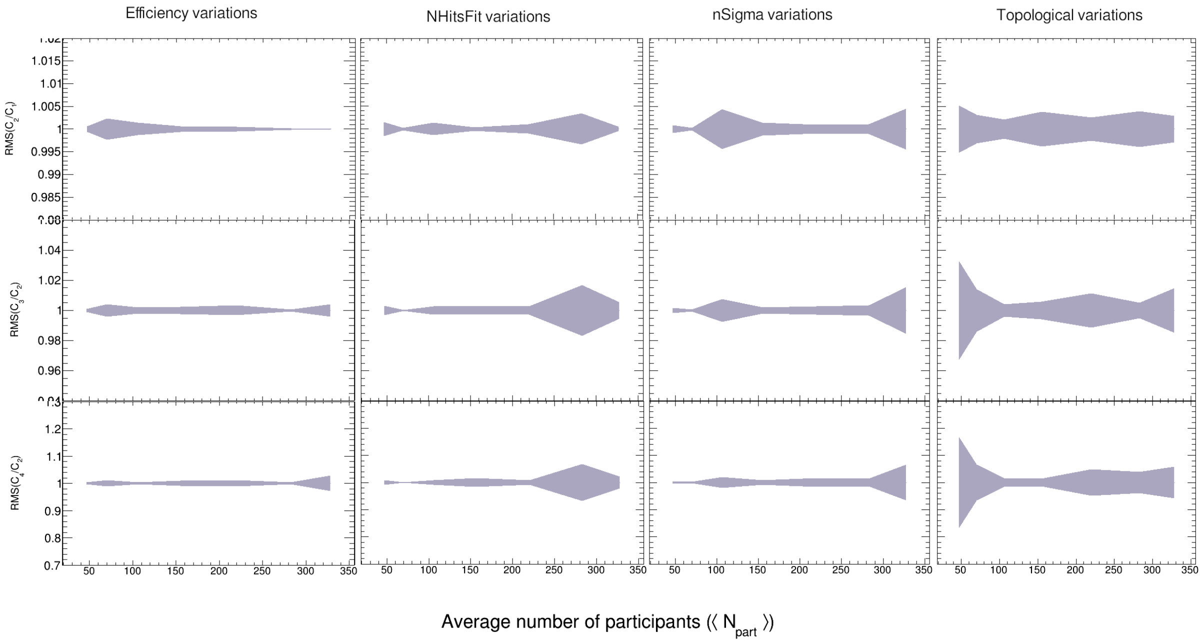

Figure 48: RMS values of *cumulant ratios* as a function of *centrality* at $\sqrt{s_{NN}} = 3.0$ GeV Au+Au collisions.

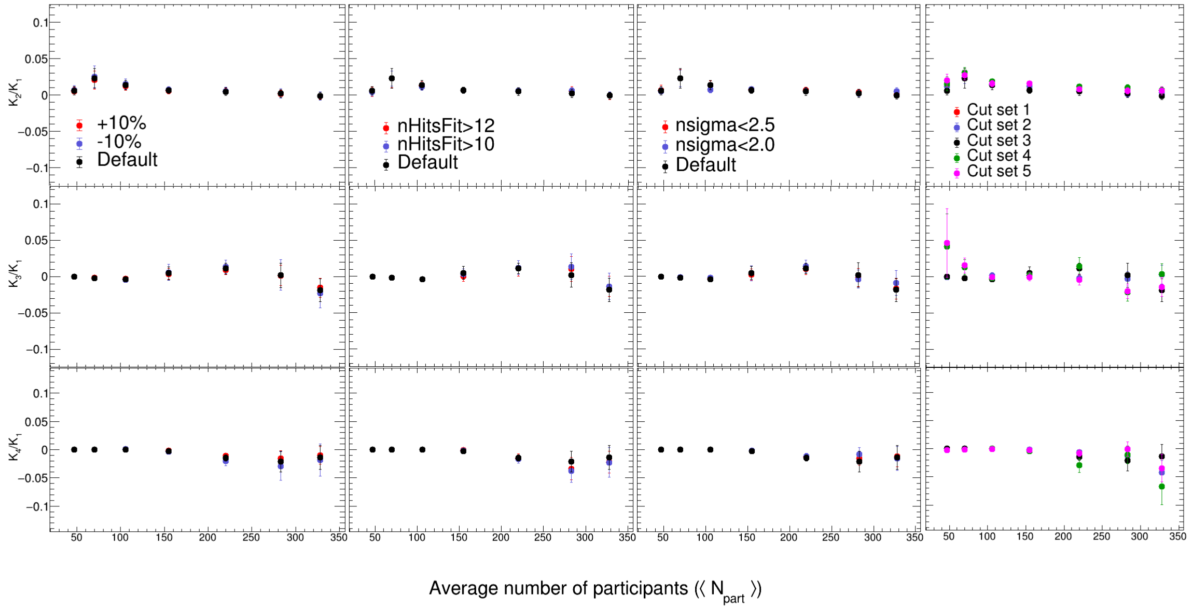

Figure 49: Effect of cut parameter variations and efficiency variation on the efficiency corrected net-lambda *correlation function ratios* as a function of *centrality* at $\sqrt{s_{NN}}$ = 3.0 GeV Au+Au collisions.

7.2.2 Systematic Variations as a Function of Δy

Figures 51 and 53 show the comparison of the cumulant ratios and correlation function ratios for different sources as a function of Δy for most central collisions $(0-5\%)$. It can be observed in Figure 52 that the topological variations dominate the systematic uncertainties in all centralities, the effect is stronger with higher order of the cumulant ratio and with increasing Δy, the reason of the contribution is due to the low efficiencies at higher Δy. The similar effect can be observed in the efficiency variations, where the contribution to systematic uncertainties increases with increasing rapidity window. The contribution of the quality of the tracks shows a constant behavior with increasing . In the case of $n\sigma$, it can be observed that there is an increasing contribution to systematic uncertainties in the region between $\Delta y = 0.4$ to $\Delta y = 0.8$, which corresponds to the central region of the TPC where most of the charge particles are detected, therefore the quality of the charged particle identification becomes more difficult. Figure 54 show the contribution of the

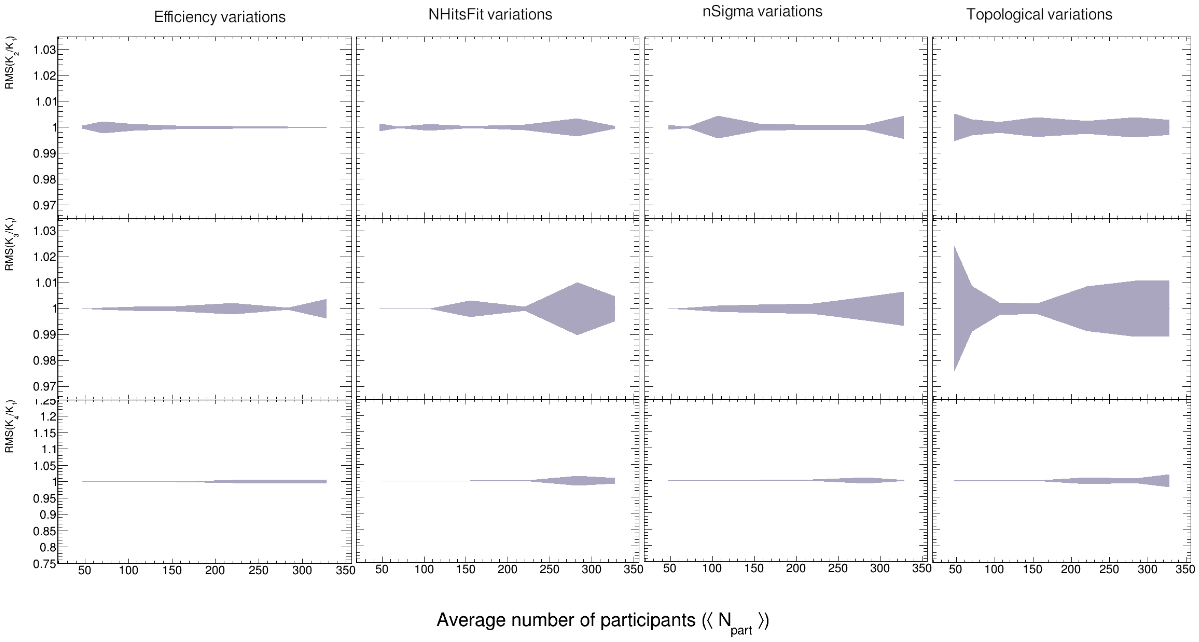

Figure 50: RMS values of *correlation function ratios* as a function of centrality at $\sqrt{s_{NN}} = 3.0$ GeV Au+Au collisions.

sources for the correlation functions, similarly to what was observed for the cumulant ratios the contribution of the topological variations is dominant for all values of Δy.

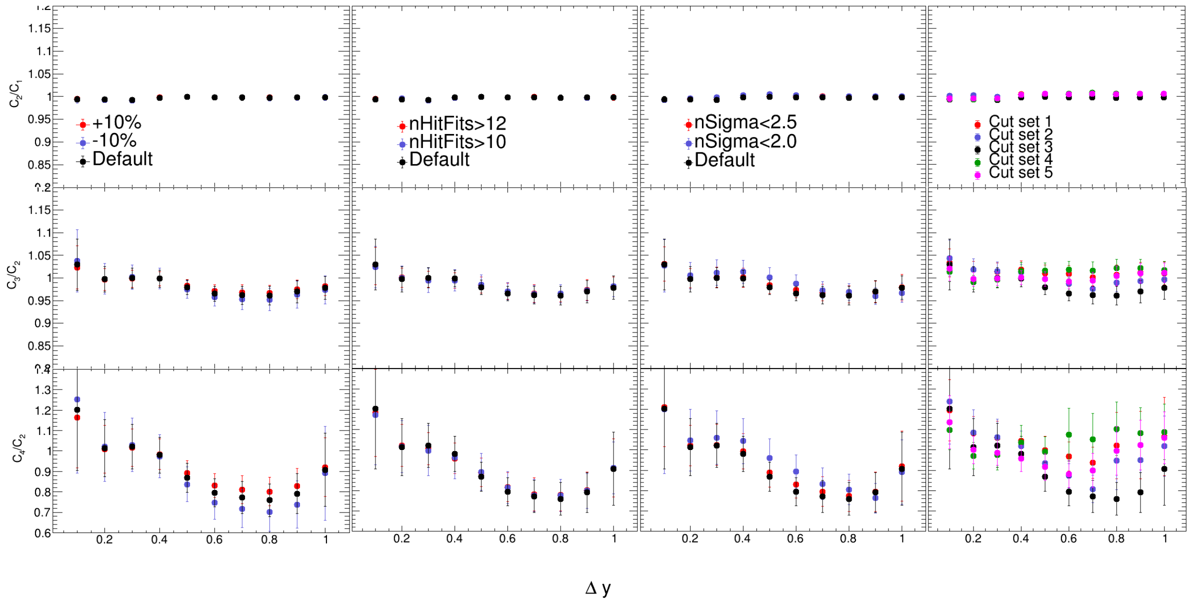

Figure 51: Effect of cut parameter variations and efficiency variation on the efficiency corrected net-lambda cumulant ratios as a function of rapidity window at $\sqrt{s_{NN}} = 3.0$ GeV Au+Au collisions.

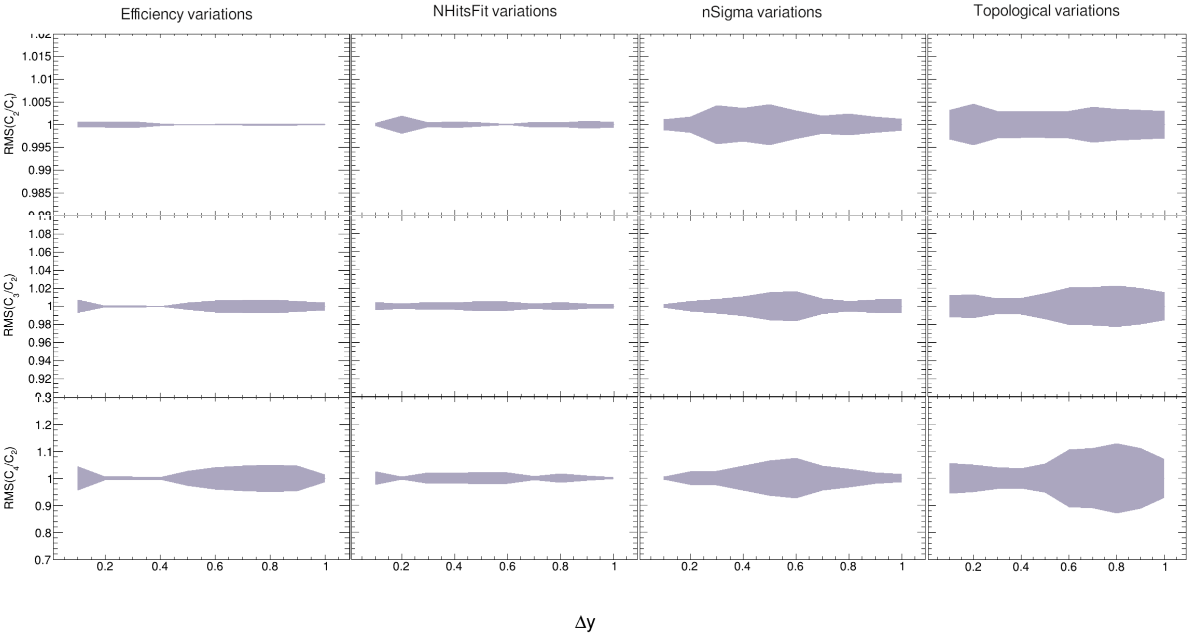

Figure 52: RMS values of cumulant ratios as a function of rapidity window at $\sqrt{s_{NN}} = 3.0$ GeV Au+Au collisions.

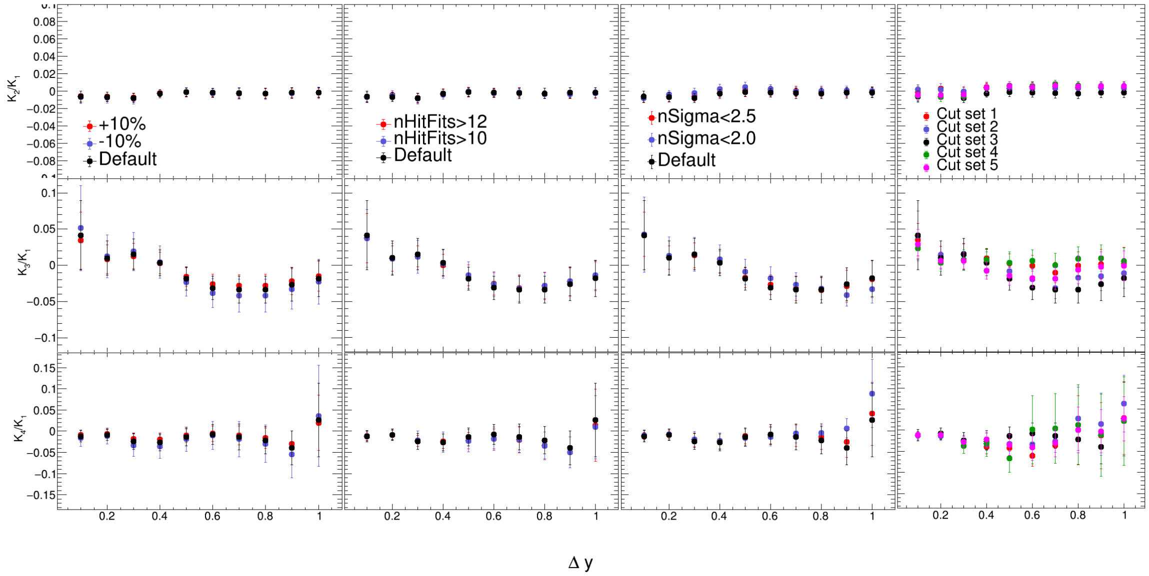

Figure 53: Effect of cut parameter variations and efficiency variation on the efficiency corrected net-lambda correlation function ratios as a function of rapidity window at $\sqrt{s_{NN}} = 3.0$ GeV Au+Au collisions.

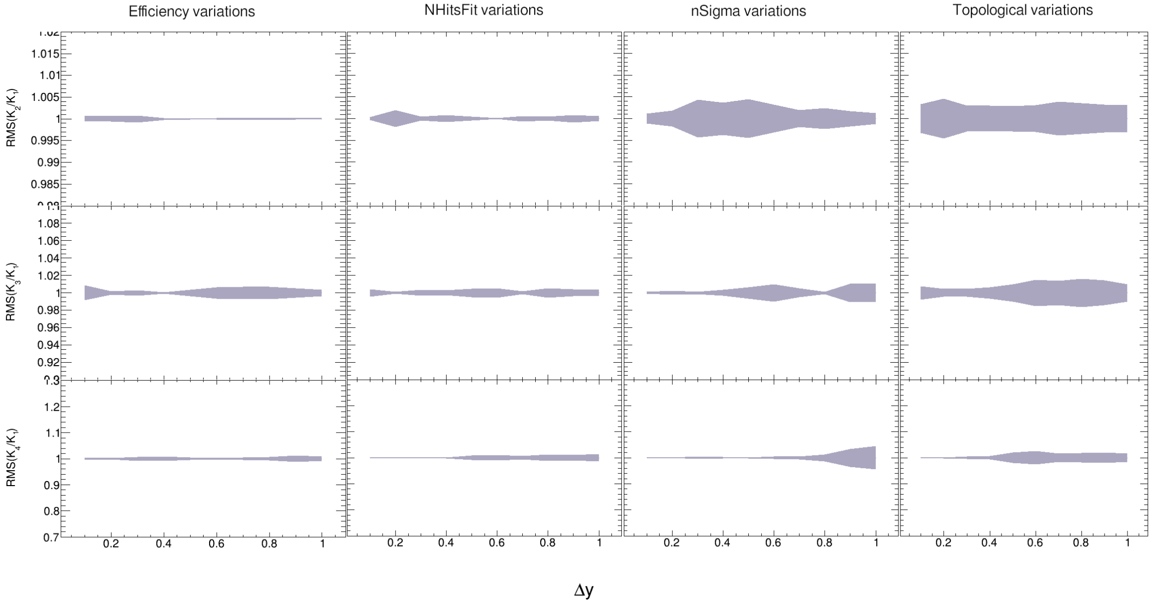

Figure 54: RMS values of correlation function ratios as a function of rapidity window at $\sqrt{s_{NN}} = 3.0$ GeV Au+Au collisions.

8 Baseline and Model Comparison

The results of the net-lambda fluctuation at $\sqrt{s_{NN}} = 3.0$ GeV need to be studied and compared with different baselines. These baselines can provide the underlying physics interpretation of the measured data.

8.1 Poisson Baseline

In the abscence of particle correlations, the measured particles behave as a gas of free particles that obey a Poission statistics. In a net-particle multiplicity distribution, the proper baseline that was used was the difference of two independet Poission distributions which is called a Skellam distribution. The probability mass function for a Skellam distribution is given by

$$P(N) = \left(\frac{\mu_1}{\mu_2}\right)(N/2) I_N(2\sqrt{\mu_1 \mu_2}) e^{-(\mu_1+\mu_2)} \tag{124}$$

where μ_1 and μ_2 are the means of the particle and anti-particle distributions. I_N corresponds to the modified Bessel functions of the first kind. The baseline for the cumulants of a net-particle distribution is given by

$$C_{2n} = \mu_1 + \mu_2, \quad n = 1, 2, 3, ... \tag{125}$$

$$C_{2n-1} = \mu_1 - \mu_2, \quad n = 1, 2, 3, ... \tag{126}$$

As mentioned previously for the net-lambda fluctuation analysis at $\sqrt{s_{NN}} = 3.0$ GeV, the production of antilambdas is negligible. Therefore, for this analysis the corresponding baseline for the cumulants is given by

$$C_{2n} = \mu_{\text{lambda}}, \quad n = 1, 2, 3, ... \tag{127}$$

$$C_{2n-1} = \mu_{\text{lambda}}, \qquad n = 1, 2, 3, ... \tag{128}$$

Thus, all cumulant ratios equate to one in the poissonian limit (e.g. $C_2/C_1 = C_3/C_2 = C_4/C_2 = 1$).

8.2 UrQMD Transport Model

All results from the net-lambda fluctuation, at $\sqrt{s_{NN}} = 3.0$ GeV were compared to UrQMD. UrQMD is a microscopic transport model which is tuned to reproduce particle observables. This microscopic transport model describes phenomenologically the interactions between hadrons at collision energies of $\sqrt{s_{NN}} < 5$ GeV [63] in terms of interactions between known hadrons and their resonances. The microscopic theory is based on the covariant propagation of hadrons on classical trajectories in combination with stochastic binary scatterings, color string formation and resonance decay. The model represents the Monte Carlo solution of a set of coupled partial integro-differential equations for the time evolution of phase space densities of different particle species. It is important to emphasize that the model does not produce a system in equilibrium and therefore does not contain any critical phenomena. The model additionally guarantees that quantum numbers are conserved globally event-by-event on the Cooper-Frye hypersurface [64]. For this analysis, 80 million of events were used using UrQMD 3.4 in Au+Au collisions at $\sqrt{s_{NN}} = 3.0$ GeV in cascade mode. The net-lambda single cumulants and cumulant ratios were calculated as functions of collisions centrality and rapidity.

8.3 Hadron Resonance Gas Model

Thermal-statistical models, such as the hadron resonance model, have been used as a good description of many experimental hadron yield data from heavy-ion collisions for a broad range of collision energies [65], [66]. Thermal-statistical models assume emission of particles from a thermally and chemically equilibrated source created in these reactions. By fitting the observed yields of stable hadrons, one is allowed to determine thermal parameters that correspond to the chemical freeze-out stage of the collisions. The results from the net-lambda fluctuation analysis at $\sqrt{s_{NN}} = 3.0$ GeV were compared with the Thermal-FIST package [67], which allowed to study the results within the different extensions of the HRG model.

8.3.1 Ideal HRG

In the simplest setup of the HRG model, the thermodynamics of the hadronic phase is described by an ideal gas of point-like hadrons. Interacting hadronic matter in the ground state is approximated by a non-interacting resonance gas. In the grand canonical ensemble (GCE) of the ideal HRG model there are no correlations between different hadronic species. Therefore, the pressure is written as

$$p(T, \mu) = \sum_i p_i^{id}(T, \mu_i) \tag{129}$$

where the sum is over all hadron species included in the model and the pressures $p_i(T, \mu_i)$ is given by the ideal Fermi or Bose gas at the corresponding temperature and chemical potential.

$$p_i^{id}(T, \mu_i) = \frac{d_i}{6\pi^2} \int_0^\infty \frac{k^4 dk}{\sqrt{k^2 + m_i^2}} \left[\exp\left(\frac{\sqrt{k^2 + m_i^2} - \mu_i}{T} \right) + \eta_i \right]^{-1} \tag{130}$$

where d_i and m_i are the spin degeneracy and mass of hadron species i, respectively. η_i, equals to $+1$ for fermions and -1 for bosons, 0 for the Boltzmann approximation. Within the GCE formulation, all conserved charges, such as baryon number B, electric charge Q and strangeness S, are conserved on average. The susceptibilities of conserved charges can be calculated as

$$\chi_{lmn}^{BSQ} = \frac{\partial^{l+m+n} p/T^4}{\partial(\mu_B/T)^l \partial(\mu_S/T)^m \partial(\mu_Q/T)^n} \tag{131}$$

where l, m and n stand for the different orders in the susceptibility.

8.3.2 Quantum Van der Waals HRG

Interactions between hadrons can be assigned explicitly within the HRG model. The presence of both, short-range repulsive and intermediate/long range attractive interactions can be treated in the framework of the Quantum Van der Waals (QvdW) equations [68]. The HRG-QvdW model is defined by using the following pressure function

$$p(T, \mu) = \sum_i p_i^{id}(T, \mu_i^*) - \sum_{i,j} a_{ij} n_i n_j \tag{132}$$

where p_i^{id} corresponds to the pressure in the ideal HRG and n_i corresponds to the particle number densities, which satisfy the system of linear equations

$$\sum_j [\delta_{ij} + \tilde{b}_{ji} n_i^{id}(T, \mu_i^*)] n_j = n_i^{id}(T, \mu_i^*). \tag{133}$$

The shifted chemical potentials, μ_i^*, satisfy the system of transcendental equations

$$\mu_i^* + \sum_j \tilde{b}_{ij} p_j^* - \sum_j (a_{ij} + a_{ji}) n_j = \mu_i. \tag{134}$$

Therefore, in order to calculate the pressure $p(T, \mu)$, first one needs to solve numerically the system of equations for μ_i^* and then use these results in Eq. (132). The parameters $\tilde{b}_{ij}$ and a_{ij} correspond to the repulsive and attractive part between hadrons of the QvdW equation, respectively. The HRG-QvdW model allows the inclusion into the HRG model of the basic features of nuclear matter, in particular, the nuclear liquid-gas phase transition. At $\sqrt{s_{NN}} = 3.0$ GeV, the values used for the repulsive and attractive parameters are $b = 3.42$ fm^3 and $a = 329$ MeVfm^3, which are obtained by fixing a and b in order to reproduce properties of nuclear matter in its ground state [68].

8.3.3 Strangeness Canonical Ensemble HRG

The canonical ensemble assummes exact conservation of the corresponding conserved charges in the system. At intermediate heavy-ion collision energies, such as $\sqrt{s_{NN}} = 3.0$ GeV, the abundances of hadrons carrying strangeness are significantly smaller than the produced light flavored hadrons. Therefore, in this case it is sufficient to implement the canonical treatment of strangeness only, while preserving the grand canonical treatment of the baryon number. Within Thermal-FIST, the canonical treatment of strangeness is archived in the strangeness-canonical ensemble (SCE).

9 Results and Discussion

In this section, the net-lambda fluctuation measurements are presented as a function of centrality, rapidity window and a comparison with the previous net-lambda measurements [35] is done as a function of collision energy. The cumulant and factorial cumulant results are calculated accordingly to the procedures described in Section 3 and Section 4 and 6 of this dissertation. The net-lambda cumulants and correlation functions were corrected for reconstruction efficiency using the "track-by-track" efficiency correction as described in Section 6.0.3. The statistical uncertainties and systematic uncertainties were calculated and are presented using a vertical error-bar and a shaded error bar, respectively. The results are presented for different centralities, where the centrality bin-width correction is used to reduce the bin-width effect. The results are compared as a function of centrality and rapidity with the poissonian baseline and predictions from the UrQMD model. Cumulant ratios as a function of rapidity window are compared with thermal model predictions (HRG) for different cases.

9.1 Single Cumulants and Correlation Functions as a Function of Centrality

As it was discussed in Section 3, the collision centrality is used as a measure of the degree of overlap between the two colliding nuclei. The quantity used to represent the collision centrality is the average number of participating nucleons ($\langle N_{Part} \rangle$). Figure 55 shows the centrality dependence of the first four single cumulants. As it can be observed, the single cumulants show increasing behavior with increasing $\langle N_{Part} \rangle$. It can be observed that C_1, that represents the mean number of lambdas at $\sqrt{s_{NN}} = 3.0$ GeV , shows low production of strange particles at this energy and increases for most central collisions, as expected. The transport model UrQMD has better agreement with data for most peripheral collisions and starts to deviate from data for most central collisions. The deviation increases with increasing order of the cumulant. The deviation of the single cumulants from UrQMD was also observed for higher energies [35], impliying that UrQMD might over-predict strange baryon production at low $\sqrt{s_{NN}}$. The relative deviation of the transport model for the higher moments is consistent when propagating the initial over-prediction in the produced particle mean (C_1) to C_2, C_3, C_4. Figure 56 shows the centrality dependence of the correlation function. It can be observed that UrQMD agrees better for factorial cumulants greater than K_1. This again might indicate that UrQMD over-predicts the lambda yield.

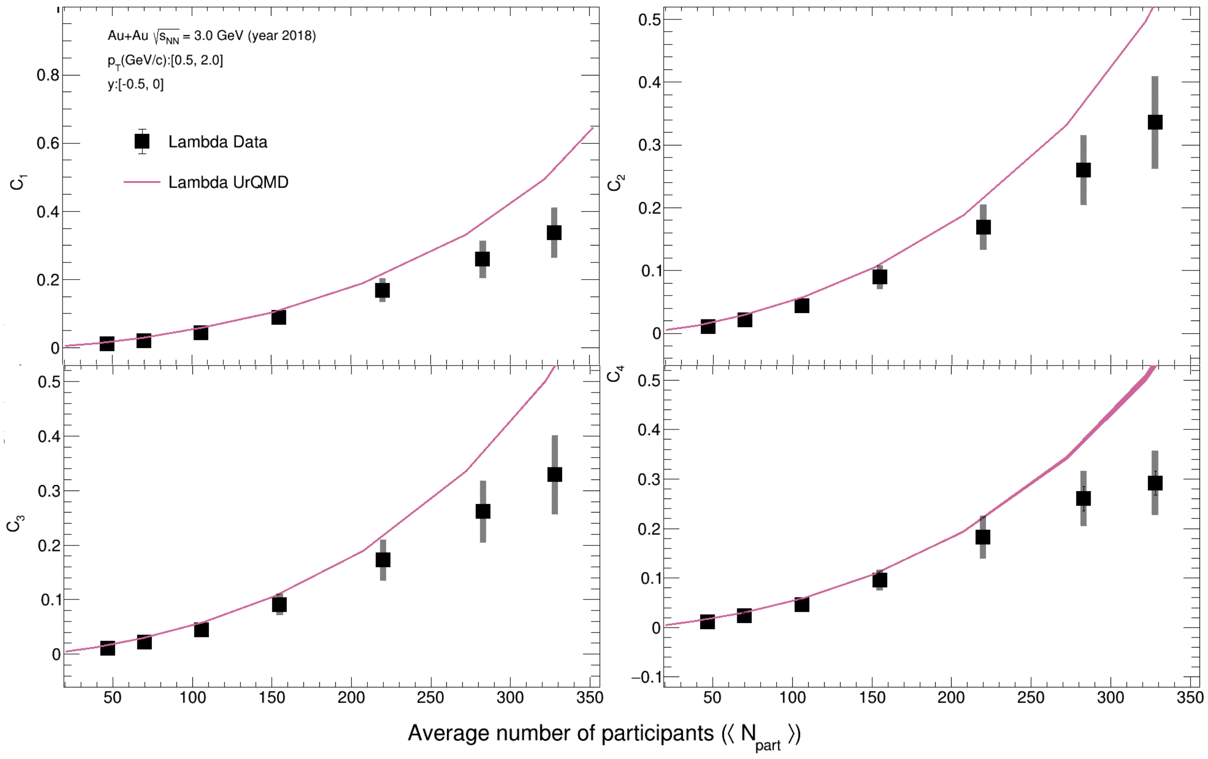

Figure 55: Single cumulants as functions of centrality.

9.2 Cumulant Ratios and Correlation Function Ratios as a Function of Centrality

Figure 57 shows the cumulant ratios as a function of centrality. It can be observed that the cumulant ratios are consistent with the Poissonian baseline at all centralities and for all orders of the ratios. This is also true for the UrQMD calculations. A slight depletion for central collisions,

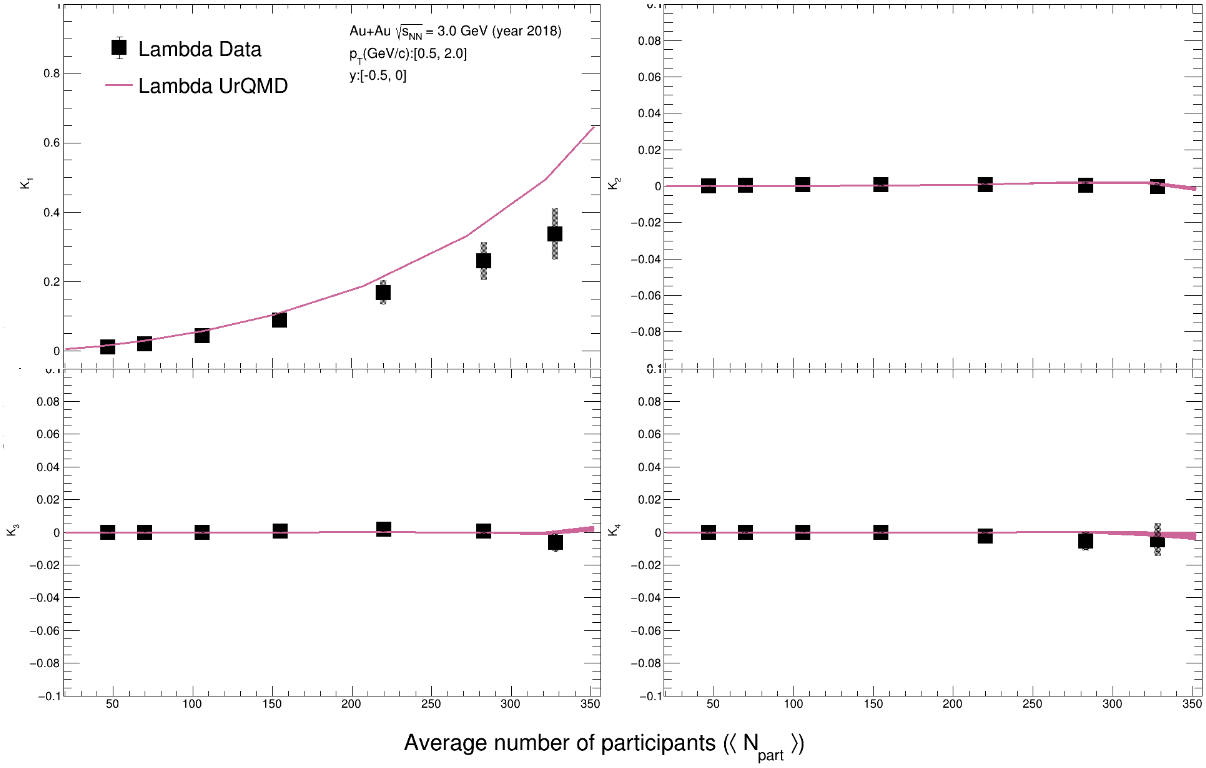

Figure 56: Correlation functions as functions of centrality.

away from the baseline, can be observed for the higher moment ratios, which becomes statistically significant for C_4/C_2 at the highest centralities. As described in Section 1, the reason for using cumulant ratios is due to the easy comparison of fluctuation measurements with theory due to the volume independence of the observable. Therefore, as observed in Figure 57, the ratios show weak dependence on the collision centrality, as it is expected. The UrQMD cumulant ratios show better agreement with data as a function of centrality. Deviations from UrQMD start to be noticeable with increasing order of the cumulant ratio. Regarding the statistical uncertainties, it can be observed that they dominate in most peripheral collisions, mainly due to the low lambda production at $\sqrt{s_{NN}} = 3.0$ GeV and the high contribution of systematics for most peripheral collisions is mainly due to the sensitivity of the V^0 reconstruction to topological cuts (see Figure 48) in a centrality with low lambda multiplicity. Overall, systematic uncertainties dominate for most peripheral and most central collisions, in the latter due to increased background in the particle identification and the sensitivity of the topological cuts at low $\sqrt{s_{NN}}$. Figure 58 shows the correlation function ratios as a function of centrality. As mentioned in Section 5.2, the correlation function ratios represent a genuine measure of multi-particle correlations [69]. K_2/K_1, K_3/K_1 and K_4/K_1 indicate two, three and four lambda particle correlations. As it can be observed, the ratios behave independently of the centrality. This indicates that the correlation function ratios depend very weakly on the number of produced lambdas, since lambda production increases with increasing participating nucleons. One scenario proposed for the aforementioned behavior, is that the sources of correlation are correlated themselves or that the sources correlate with increasing number of particles [69]. In any case, centrality independence of the correlation functions indicates that an increasing number of lambda particles are correlated [69] . In summary, the centrality dependence of both the cumulant ratios and factorial cumulant ratios show small correlation for mid-central and peripheral collisions. At the same time, higher order cumulant ratios (C_4/C_2 and C_3/C_2) show weak suppression from the poissonian baseline for most central collisions.

9.3 Cumulant Ratios and Correlation Function Ratios as a Function of Δy

In light of the deviation of C_4/C_2 away from the Poissonian baseline in central collisions, it was decided to measure the ratios and correlation functions also as a function of rapidity for the most central collisions ($0-5\%$). The study of cumulant and correlation functions as a function of rapidity was done by asymmetrically increasing the rapidity window (Δy), where the studied window is $y_{min} < y < 0$. The rapidity cut y_{min} is varied from -0.9 to -0.2. Figure 59 show, the rapidity dependence of lambda cumulant ratios within $y_{min} < y < 0$ and $0.5 < p_T(\mathrm{GeV/c}) < 2.0$ for the most central $(0 - 5\%)$ centrality class. It can be observed that all cumulant ratios approach unity as the rapidity window (Δy) is decreased. The C_2/C_1 ratios shows a largely independence of Δy. The cumulant ratio C_3/C_2 and C_4/C_2 show suppression from unity with increasing Δy. The values of the UrQMD cumulant ratios show similar decreasing trends with increasing Δy but not

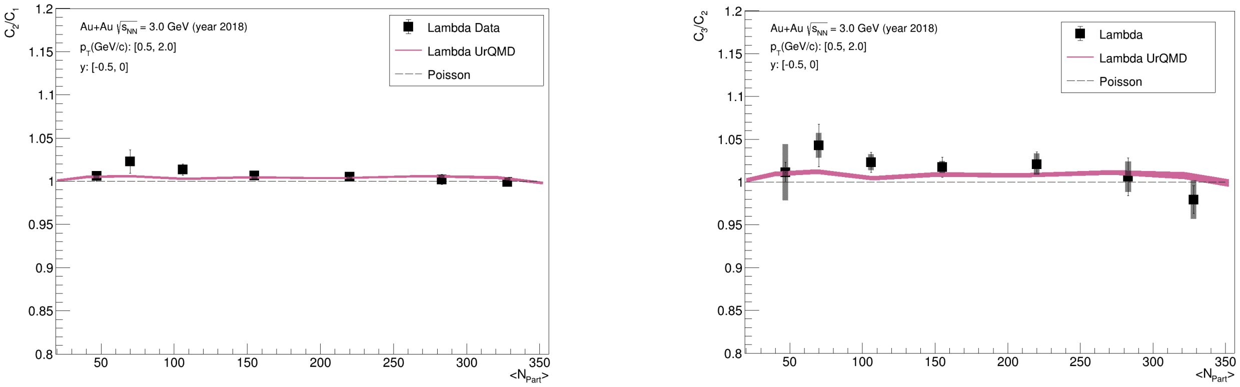

(a) C_2/C_1 (b) C_3/C_2

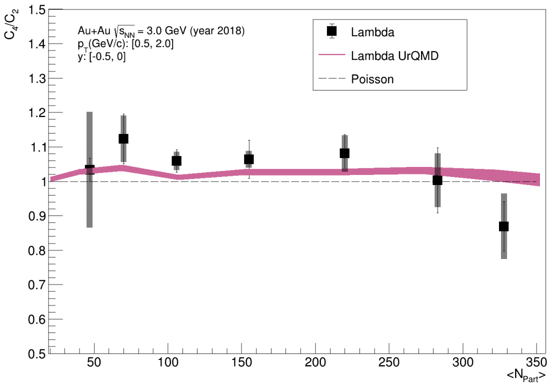

(c) C_4/C_2

Figure 57: Cumulant ratios as functions of centrality.

as strong as shown in data. Qualitatively, there are two different acceptance regimes in the system: when $\Delta y \gg \Delta y_{corr}$ and $\Delta y \ll \Delta y_{corr}$, where Δy is the width of the acceptance in rapidity and Δy_{corr} is the range of the lambda correlation in rapidity. When $\Delta y << \Delta y_{corr}$, it is expected that $\Delta y \sim \langle N \rangle \to 0$ and the cumulant ratios approach to Poisson limit. This is shown in Figure 59. Similarly, as $\Delta y \to 0$, it is expected that the correlation functions become rapidity independent and approach 0; this is also observed in Figure 60. In the large rapidity window $\Delta y >> \Delta y_{corr}$, cumulants are expected to grow linearly as Δy increases. Figure 61 shows the linear-like behavior for the cumulants: C_4 seems to deviate from a linear behavior for high values of Δy. Therefore, as the cumulants grow linearly, the cumulant ratios will plateau, which indicates a saturation of the physical correlations. The saturation is observed in cumulant ratios C_3/C_2 and C_4/C_2 for values greater than $\Delta y = 0.6$. It is important to mention that, if the cumulant ratios continue to increase,

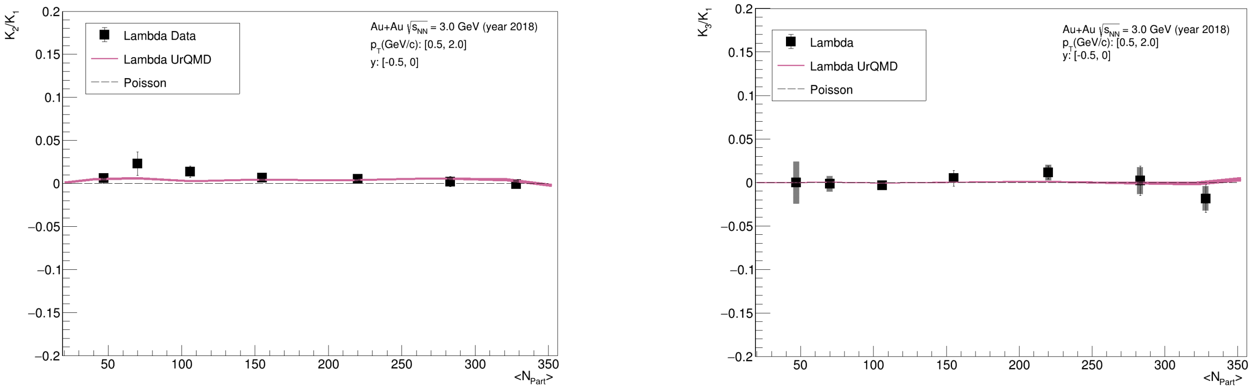

(a) K_2/K_1 (b) K_3/K_1

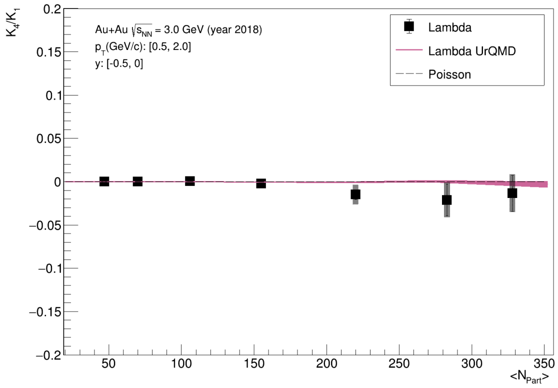

(c) K_4/K_1

Figure 58: Correlation function ratios as functions of centrality.

this could indicate uncorrelated effects in the measurement, such as volume fluctuations [69]. The deviation of the cumulant ratios C_3/C_2 and C_4/C_2 from the poissonian limit does not imply a priori the presence of any three or four particle correlations, since two-particle correlation functions might also play a role in the contribution to the linear combination of multi-particle correlation functions to construct the cumulant ratios [69]. Other non-equilibrium effects might enter into play when studying the acceptance dependence of the cumulant ratios, such as hadronic rescattering in the expansion of the system [70].

In the case of the rapidity dependence of the correlation functions, it can be observed from Figure 60 that the ratio K_2/K_1 shows values close to zero and shows agreement within error bars with the transport model UrQMD. K_3/K_1 shows suppression from the poissonian baseline ($K_3/K_1 = 0$) and deviates from UrQMD as Δy increases. K_4/K_1 shows small suppression from the poissonian baseline ($K_4/K_1 = 0$) at $\Delta y = 0.3$. For all other rapidity windows it remains poissonian within error bars. UrQMD shows poissonian-like behavior for all correlation functions.

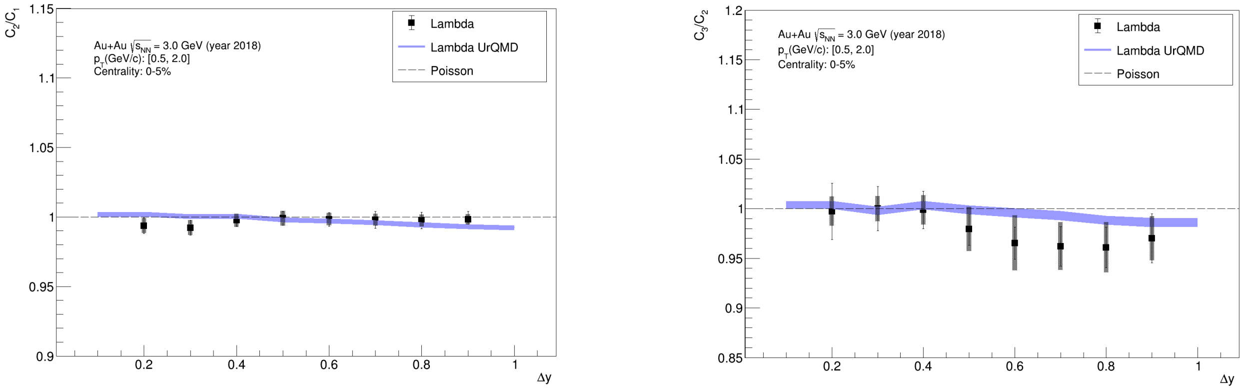

(a) C_2/C_1 (b) C_3/C_2

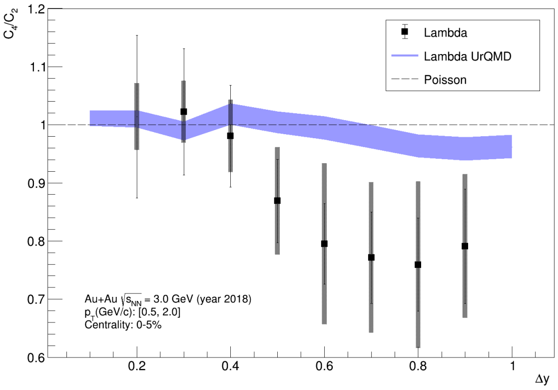

(c) C_4/C_2

Figure 59: Cumulant ratios as functions of rapidity window.

9.4 Comparison with Thermal Model Predictions

Figures 61 and 62 show the comparisons between lambda single cumulants and cumulant ratios as functions of Δy with results from the HRG model for most central collisions ($0 - 5\%$). The magenta and green bands show the HRG prediction for lambda cumulants and cumulant ratios at the freeze-out temperatures (T_f) and chemical potential (μ_f) extracted from preliminary particle yields from the STAR collaboration at $\sqrt{s_{NN}} = 3.0$ GeV. Table 6 shows the parameters obtained from the fit of the particle yields in the GCE and SCE for both ideal and QvdW case. The magenta

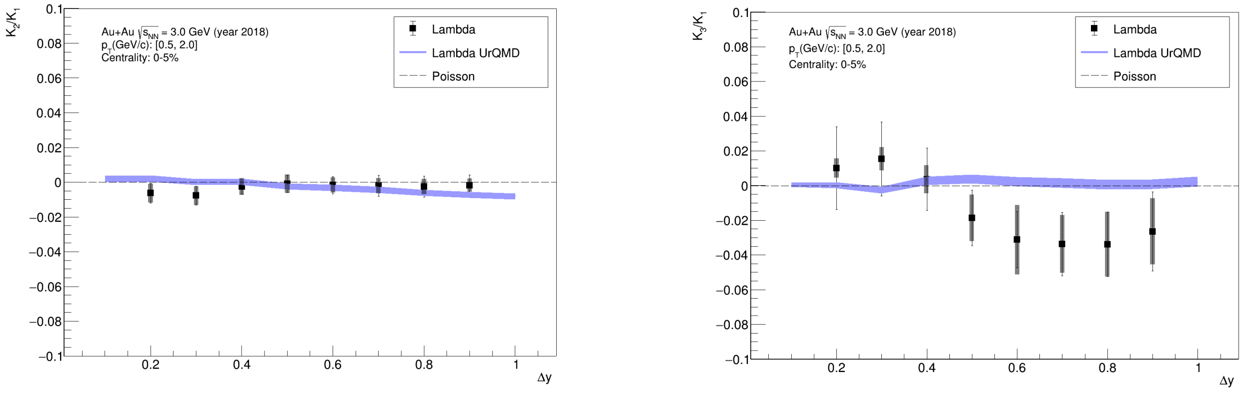

(a) K_2/K_1

(b) K_3/K_1

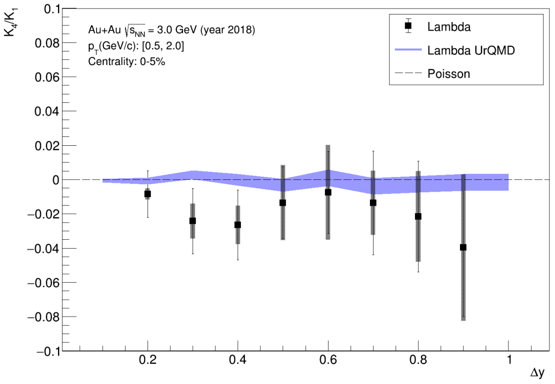

(c) K_4/K_1

Figure 60: Correlation functions as functions of Δy.

band shows the prediction in the case of the grand canonical ensemble with quantum Van der Waals interactions (QvdW GCE), where the charges (Q, B, S) are conserved on average. Similarly the green band shows the prediction in the case of the strangeness canonical ensemble (SCE), where the strangeness charge is conserved exact while preserving the grand canonical treatment of baryon number. The blue band corresponds to the interacting case of the canonical ensemble (QvdW SCE). As it can be observed in Figure 61, the trend of the data is described by the two versions of HRG but it fails to completely agree with the data. The GCE version deviates from the data in all orders of the cumulants. For the SCE ensemble, it can be observed that the results show less deviation from data when the order of the cumulant increases, implying a higher sensitivity of the local strangeness conservation in higher order cumulants.

Figure 62 shows the cumulant ratios compared with the thermal model. It can be observed

Table 6: Parameters obtained from Thermal FIST [67] using preliminary particle yields at $\sqrt{s_{NN}} =$ 3.0 GeV

Parameters	Ideal GCE	QvdW GCE	Ideal SCE	QvdW SCE
T(MeV)	57.7 ± 0.9	57.7 ± 0.9	64.3 ± 0.6	64.3 ± 0.6
μ_B(MeV)	703.8 ± 4.6	701.9 ± 4.3	714.7 ± 5.3	711.5 ± 5.1
r(fm)	21.9 ± 1.1	21.9 ± 1.1	16.9 ± 0.8	16.9 ± 0.7
r_{corr}(fm)	–	–	10 ± 0.6	9.9 ± 0.6
μ_Q (MeV)	-10.69	-10.64	-12.94	-12.94
μ_S (MeV)	97.51	97.5	–	–
χ^2/NDF	8.6	8.6	11.9	11.8

that the cumulant ratios for the QvdW GCE case remain poissonian ($C_2/C_1 = C_3/C_2 = C_4/C_2 = 1$) for all values of Δy. It has to be noted that, in the ideal GCE case, the cumulant ratios remain poissonian. On the other hand, the cumulant ratios in the SCE case show suppression with increasing Δy; the suppression is stronger with increasing order of the cumulant ratio. The SCE ensemble describes qualitatively the trend observed in the data, except for the C_4/C_2 case, where for the value at $\Delta y = 0.5$ the model describes the data. It has to be noted that the values of the cumulants and cumulant ratios from SCE here obtained from the extracted parameters obtained from the particle yields at $\sqrt{s_{NN}} = 3.0$ GeV. Some of these parameters are the volume of the system (V) and the strangeness canonical correlation volume (V_c), which assumes two spheres with radii r and r_c, respectively. r_c defines a region of the particle production phase space inside which the production of strangeness is canonically conserved. It is important to point out that the QvdW and the Ideal model do not show major differences. The extracted values used to obtain the cumulants from the thermal model are $r = (16.9 \pm 0.8)$ fm and $r_c = (10.0 \pm 0.6)$ fm. The sensitivity of the cumulants is highly dependent on the value of r_c . If the value of r_c is increased while maintaining fixed r, the cumulant ratios show stronger suppression than the one observed in Figure 62. On the other hand, if r_c decreases while maintaining a fixed r, the cumulant ratios show weak suppression and show values close to 1.0. Recently, the STAR collaboration reported the measurements of strange hadrons K^-, ϕ and Ξ^- yields and their ratios in Au+Au collisions at $\sqrt{s_{NN}} = 3.0$ GeV [71]. The 4π yields were compared to thermal model predictions with the grand canonical ensemble and the canonical ensemble for strangeness. It was observed that the ratios were reproduced using the canonical ensemble of strangeness with correlation lengths of $r_c \sim 2.7$ fm and $r_c \sim 4.2$ fm for the ϕ/K^- and ϕ/Ξ^- , respectively. This indicates that the event-by-event strangeness conservation is crucial at these energies [72] and more importantly it implies that the value of r_c dependents on the strangeness quantum number S. This suggest that the value of r_c needs to be studied for the case of lambda particles, which seems to have higher value than the one obtained from the particle yields at $\sqrt{s_{NN}} = 3.0$ GeV. Since higher order cumulant ratios are significantly more sensitive to any quantum number correlation volume than the simple yield ratios, it is likely that the combination of strangeness and baryon number in the case of lambda particles requires a larger volume that is only fully mapped out when studying the event-by-event kurtosis over variance ratio of the particle distribution. Thus, these first results indicate that further studies of the fluctuations of multi-strange baryons might be needed.

9.5 Beam-energy Dependence of Net-lambda Cumulant ratios, C_2/C_1 and C_3/C_2

Figure 63 shows the beam-energy dependence of the net-lambda cumulant ratios, where the values of the lowest center of mass energy achieved in STAR ($\sqrt{s_{NN}} = 3.0$ GeV) was included to the already published results [35]. Where a) shows C_2/C_1 and b) C_3/C_2 for most central collisions. Due to low statistics during the first beam energy scan at RHIC, higher order cumulants were not possible to obtain. It can be observed in a) that C_2/C_1 increases monotonically as a function of increasing collision energy in most central collisions. The measured values shows better agreement with the Ideal HRG model at high s_{NN}, while UrQMD shows strong deviations from data with increasing $\sqrt{s_{NN}}$.

Figure 63 b), shows that C_3/C_2 monotonically decreases as a function of increasing collision energy with approach to zero at 200 GeV and approach to unity at 3 GeV. UrQMD predictions for C_3/C_2 also followed the same trend as in the data and decreased as a function of

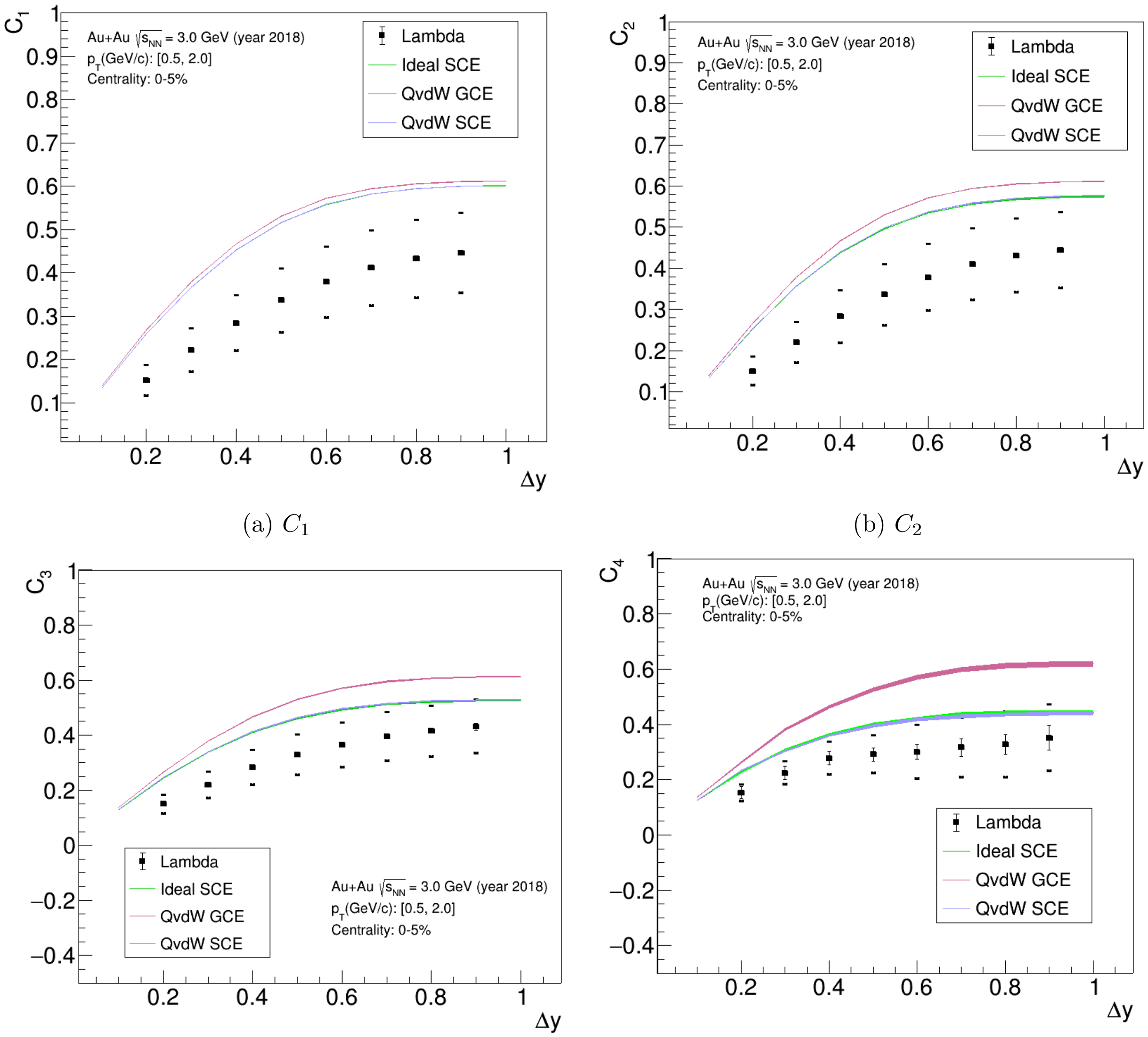

(a) C_1

(b) C_2

(c) C_3

(d) C_4

Figure 61: Single cumulants as functions of rapidity window compared with thermal model calculations.

increasing energy but deviate from most of the data points. It can also be observed that the results from the ideal HRG model show better agreement with the data points. The ideal HRG predictions for net-lambda cumulant ratios were calculated at the values of freeze-out temperatures (T_f) and chemical potentials (μ_f) extracted from particle yields from different energies ($\sqrt{s_{NN}}$ = 3, 4.9, 7.7, 11.5, 19.6, 27, 39, 62.4, 200GeV). The ideal HRG using the SCE ensemble is added for comparison at $\sqrt{s_{NN}}$ = 3.0 GeV; overall it shows a weak suppression from the predicted

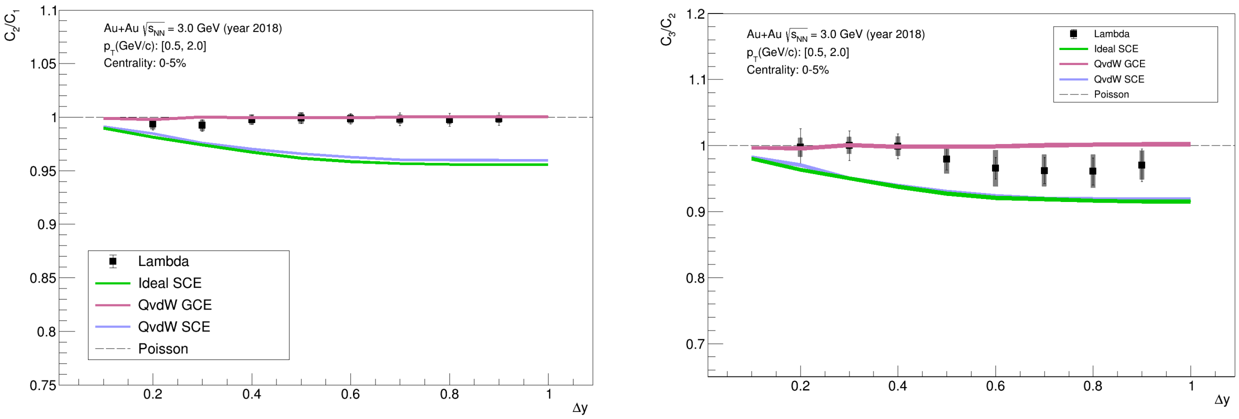

(a) C_2/C_1 (b) C_3/C_2

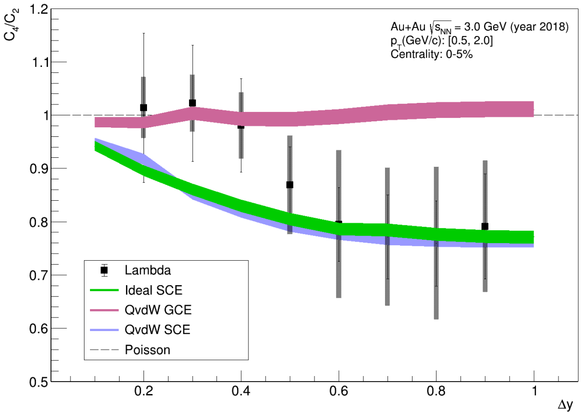

(c) C_4/C_2

Figure 62: Cumulant ratios as functions of rapidity window compared with thermal model calculations.

point of ideal HRG GCE.

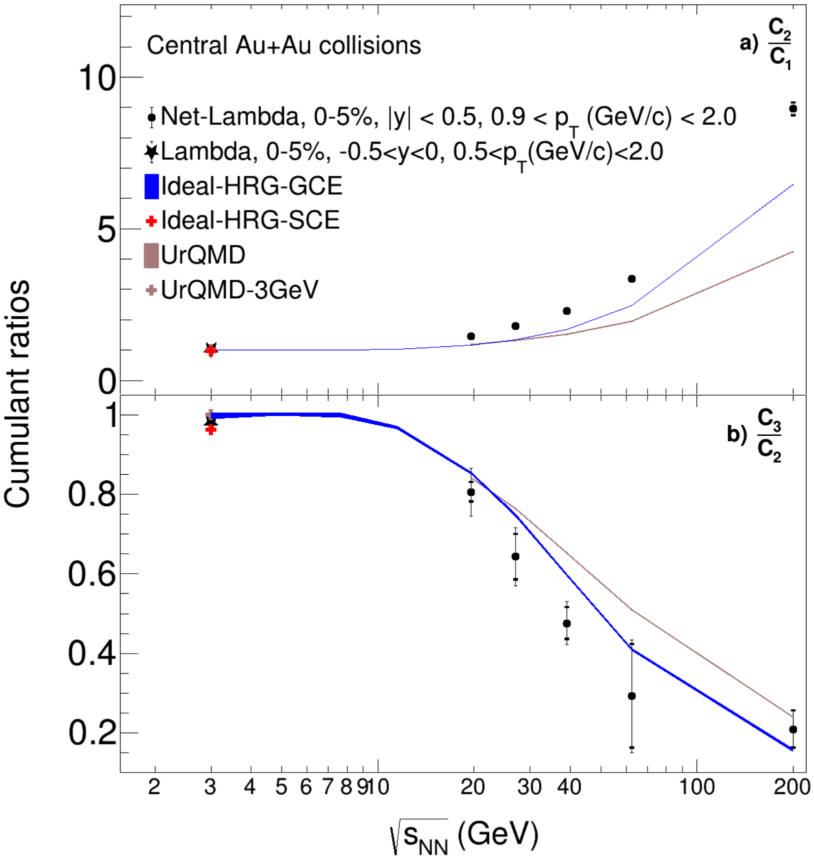

Figure 63: Cumulant ratios (C_3/C_2 and C_2/C_1) as functions of center of mass energy.

10 Summary

The objective of the beam energy scan (BES) at RHIC is to study the characteristics of the QCD-phase diagram to obtain information about the strongly interacting matter and its evolution along the temperature and chemical potential. The identified net-particle multiplicity distributions that were created after heavy ion collisions were used as proxies for net quantum number fluctuations. The importance of the proxies relies on their sensitivity to the correlation length that could provide hints on the location of the QCD critical point. The second beam energy scan (BES-II) was motivated by many results obtained in the BES-I that suggested a change in the equation of state of QCD matter [73], [74]. The study from BES-I showed a non-monotonic behavior of the cumulant ratio C_4/C_2 of net-proton multiplicity distributions in central Au+Au collisions as a function of energy [75]. This result motivated the focus on the collision energy in the region between $3-20$ GeV, which required the change in configuration in the STAR detector from collider mode to fixed-target mode.

From the previous work on net-lambda fluctuations [35], it was shown that the first cumulant ratios and did not provide any information about the location of the critical point, higher order fluctuations were necessary to have better sensitivity to the location of the critical point due to their relation with the correlation length. Therefore, in order to measure higher order fluctuations higher statistics are necessary. During BES-II the statistics was increased and the fixed target mode extended the range of energies down to $\sqrt{s_{NN}} = 3.0$ GeV. This dissertation describes a systematic study of cumulants and correlation functions of lambda multiplicity distributions from Au+Au collisions at $\sqrt{s_N} = 3.0$ GeV. The data was collected with the STAR fixed-target mode in 2018 at RHIC. The results include cumulants and factorial cumulants as functions of centrality, acceptance and the result was compared with the previous results at other different energies. The STAR TPC detector was used for the charged particle identification of protons and pions for the reconstruction of the invariant mass of the lambda baryon. The purity of the reconstruction of the V^0 for the lambda particle was enhanced by optimizing topological cuts. The result is shown for a purity of ($\sim 93.75\%$) and it was systematically studied for other lower values of purity. The reconstructed lambda particles were corrected for reconstruction inefficiencies using a binomial response function. Due to a weak correlation between the measured reference multiplicity and the initial number of participants, a considerable effect from volume fluctuations was expected. The effects of volume fluctuations were suppressed in first order by using the centrality bin-width correction, which is a data-driven correction. The results of proton fluctuations at the same energy $\sqrt{s_{NN}} = 3.0$ GeV [59] used a method to suppress the remaining effects of volume fluctuations [76]. However, the results are highly dependent on the choice of the model and therefore difficult to trust; due to this reason, the method was not applied to this analysis. It is important to mention, that the most central events of higher order cumulant ratios C_4/C_2, C_3/C_2 and C_2/C_1 are the less affected by volume fluctuations. For the net-lambda fluctuation analysis in the BES-I [35], the effects of contamination due to lambda baryons coming from multi-strange and weak decays were studied and feed-down correction was performed. It was found that the corrections increased the single cumulants but the cumulant ratios were not affected, (the feed-down contribution used was $\sim 15\%$). The contribution due to feed down decreases as the $\sqrt{s_{NN}}$ is decreased. An estimate of the feed-down contribution from the strange production suggests a 0.4% of feed-down contribution at $\sqrt{s_{NN}} = 3.0$ GeV mostly by the contribution of Ξ^-. Therefore effects from feed-down contribution for this work are negligible for single cumulants and not expected to impact cumulant ratios. This analysis was done in the transverse momentum range: $0.9 < p_T(\mathrm{GeV/c}) < 2.0$, and in an assymetric rapidity window of $-0.5 < y < 0$, where the statistics of the sample and the V^0 reconstruction efficiency became reasonable. The results were presented with statistical and systematic error bars, the results were compared with the transport model UrQMD and with the thermal model for different cases. The single cumulants (C_1, C_2, C_3, C_4) increased as a function of centrality due to the increasing number of participating nucleons in most central collisions. The cumulant ratios C_2/C_1, C_3/C_2 and C_4/C_2 show a weak dependence on the collision centrality and their behavior agrees with the poissonian limit for most of the centralities. Most central collision show a weak suppression from the poissonian baseline. Similarly, the correlation function ratios showed values consistent with zero, corresponding to the poissonian baseline. The UrQMD predictions show a similar trend as in data, where most of the cumulant ratios are consistent with the poissonian baseline and agrees largely with data, except for the most central collisions. Regarding the energy dependence of the cumulant ratios (C_2/C_1 and C_3/C_2) for most central collisions, it was shown that C_2/C_1 follows a monotonically increasing trend as a function of energy. C_3/C_2 shows a monotonic decrease as a function of energy, starting from the highest value at $\sqrt{s_{NN}} = 3.0$ and reaches it's nadir at $\sqrt{s_{NN}} = 200$ GeV. The HRG model seem, to have better agreement with data, in contrast to the UrQMD predictions. The rapidity dependence of cumulant and cumulant ratios of lambda show deviations from the poissonian baseline as the rapidity window is increased. The UrQMD results yield similar trends but deviate as the rapidity window decreases. The acceptance dependence of the lambda correlation functions shows very weak variation with respect to the poissonian baseline making the implication of the multi-particle correlations difficult at this energy. Additionally, the acceptance dependence of the cumulant ratios was compared with the HRG predictions, extracted from the published and preliminary particle yields at $\sqrt{s_{NN}} = 3.0$ GeV. The comparison shows that, by using the canonical treatment on the strangeness quantum number, the cumulants show that deviations from the model and data are reduced considerably with increasing order of the cumulant, implying that higher order cumulants are more sensitive to the effects of local conservation laws. Similarly, the cumulant ratios show better agreement using the strangeness canonical approach than using the grand canonical approach. It was noted from recent studies [71] that the correlation radius (r_c) plays a role in the description of conservation laws in event-by-event measurements of strange particles at these low collision energies. Similarly, a description of the effects of local conservation laws for different values of r_c should be further investigated. Overall, although there is no evidence of critical behavior in the lambda moments the detailed measurements of the rapidity dependence of the higher order cumulant ratios in central collisions indicate the impact of strange and baryon number conservation on the measurements, and their sensitivity to these effects. In this regard, the data is consistent with the previously measured proton fluctuation data that showed that at this low collision energies the system likely does not undergo a phase transition and stays in the dense hadronic phase which is well described with purely hadronic thermal and hadronic transport models. The system energy is also too low to indicate any significant flavor hierarchy in the chemical freeze-out, although studies of correlations in multi-strange baryons might be more sensitive to the enhanced correlation of strangeness and baryon number. The precision of the data is encouraging though, for the already sampled higher fixed target collision energies between 3.0 GeV and the lowest collider energies at 7.7 GeV, which showed hints of phase transition behavior.

BIBLIOGRAPHY

[1] M. D. Schwartz, *Quantum Field Theory and the Standard Model.* Cambridge University Press, Mar. 2014, ISBN: 978-1-107-03473-0, 978-1-107-03473-0.

[2] M. Veltman, *Facts and Mysteries in Elementary Particle Physics.* World Scientific Publishing Co. Pte. Ltd., 2003, ISBN: 9812381481.

[3] D. Griffiths, *Introduction to Elementary Particles.* New York, USA: John Wiley and Sons, 1987.

[4] C. Burgard, *UX: Standard Model of the Standard Model*, `https://davidgalbraith.org/portfolio/ux-standard-model-of-the-standard-model/`, [Online; accessed 21-Dec-2022], 2016.

[5] F. Englert and R. Brout, "Broken symmetry and the mass of gauge vector messons," *Phys. Rev. Lett.*, vol. 13, pp. 321–323, 1964.

[6] P. Higgs, "Broken symmetries and the masses of gauge bosons," *Phys. Rev. Lett.*, vol. 13, pp. 508–509, 1964.

[7] B. Martin and G. Shaw, *Particle Physics.* John Wiley and Son Ltd, 2008, ISBN: 9780470032930.

[8] K. Wilson, "Confinement of quarks," *Phys. Rev. D*, vol. 10, pp. 2445–2459, 1974.

[9] R. Pasechnik and M. Sumbera, "Different faces of confinement," *Universe*, vol. 7, 2021.

[10] M. Peskin and D. Schroeder, *An Introduction to Quantum Field Theory.* CRC Press, 2018, ISBN: 9780367320560.

[11] P. Zyla and others (Particle Data Group), "Review of particle physics.," *Prog. Theor. Exp. Phys. 083C01*, vol. 2020, 2020.

[12] P. Braun-Munzinger *et al.*, "Properties of hot and dense matter from relativistic heavy ion collisions," *Phys. Rep.*, vol. 621, pp. 76–126, 2016.

[13] P. B.-M. J. Wamhach, “The phase diagram of strongly-interacting matter,” *Rev. Mod. Phys.*, vol. 81, pp. 1031–1050, 2009.

[14] A. T. (the ALICE Collaboration), “Bulk properties of pb-pb collisions at $\sqrt{s_{NN}} = 2.76$ tev measured by alice,” *J. Phys. G.*, vol. 38, 2011.

[15] S. R. Heinz U, “Collective flow and viscosity in relativistic heavy-ion collisions,” *Annu. Rev. Nucl. Part. Sci.*, vol. 63, pp. 123–151, 2013.

[16] F. Karsh, “Lattice results on qcd thermodynamics,” *Nucl. Phys.*, vol. 698, pp. 199–208, 2002.

[17] Y. Aoki *et al.*, “The order of the quantum chromodynamics transition predicted by the standard model of particle physics,” *Nature*, vol. 443, pp. 675–678, 2006.

[18] D. Thomas *et al.*, “Production of lithium, beryllium, and bron from baryon inhomogeneous primordial nucleosynthesis,” *Astrophys. J.*, vol. 430, pp. 291–299, 1994.

[19] M. A. Stephanov, “Qcd phase diagram and the critical point,” *Prog. Theor. Phys. Suppl.*, vol. 153, pp. 139–156, 2004.

[20] M. A. Stephanov, “Qcd phase diagram: An overview,” *PoS LAT2006*, vol. 024, 2006.

[21] A. Bzdak, S. Esumi, V. Koch, J. Liao, M. Stephanov, and N. Xu, “Mapping the phases of quantum chromodynamics with beam energy scan,” *Phys. Rep.*, vol. 853, pp. 1–87, 2020.

[22] M. P. J. M. Lattimer, “The equation of state of hot, dense matter and neutron stars,” *Phys. Rep.*, vol. 621, pp. 127–164, 2016.

[23] S. R. D. Page, “Dense matter in compact stars: Theoretical developments and observational constraints,” *Ann. Rev. Nucl. Part. Sci.*, vol. 56, pp. 327–374, 2006.

[24] W. Busza, K. Rajagopal, and W. van der Schee, “Heavy ion collisions: The big picture and the big questions,” *Annu. Rev. Nucl. Part. Sci.*, vol. 68, no. 1, pp. 339–376, 2018.

[25] A. Tawfik and A. Shalaby, “Balance function in high-energy collisions,” *Adv. High Energy Phys.*, vol. 2015, pp. 1–24, 2015.

[26] J. Xu, "Energy dependence of moments of net-proton, net-kaon, and net-charge multiplicity distributions at star," *J. Phys. Conf. Ser.*, vol. 736, 2016.

[27] J. T. [STAR], "Higher moments of net-particle multiplicity distributions," *Nucl. Phys.*, vol. 956, pp. 320–323, 2016.

[28] X. L. [STAR], "Energy dependence of moments of net-proton and net-charge multiplicity distributions at star," *PoS CPOD2017*, vol. 019, 2015.

[29] X. Luo, "Exploring the qcd phase structure with beam energy scan in heavy-ion collisions," *Nucl. Phys.*, vol. 956, pp. 75–82, 2016.

[30] E. S. Bowman and J. I. Kapusta, "Critical points in the linear sigma model with quarks," *Phys. Rev. C*, vol. 79, 2009.

[31] M. A. Stephanov, "Sign of kurtosis near the qcd critical point," *Phys. Rev. Lett.*, vol. 107, 2011.

[32] M. A. Stephanov, "Non-gaussian fluctuations near the qcd critical point," *Phys. Rev. Lett.*, vol. 102, p. 4, 2009.

[33] R. Bellwied, J. Noronha-Hostler, P. Parotto, I. Portillo Vazquez, C. Ratti, and J. M. Stafford, "Freeze-out temperature from net-kaon fluctuations at energies available at the bnl relativistic heavy ion collider," *Phys. Rev. C*, vol. 99, 3 2019.

[34] R. Bellwied *et al.*, "Is there a flavor hierarchy in the deconfinement transition of qcd?" *Phys. Rev. Lett.*, vol. 111, 20 2013.

[35] J. Adam *et al.*, "Beam energy dependence of net-Λ fluctuations measured by the star experiment at the bnl relativistic heavy ion collider," *Phys. Rev. C*, vol. 102, p. 024 903, 2 2020.

[36] K. H. Ackermann *et al.*, "Star detector overview," *Nucl. Instrum. Meth. A*, vol. 499, pp. 624–632, 2003. DOI: `10.1016/S0168-9002(02)01960-5`.

[37] *Relativistic heavy ion collider*, `https://science.osti.gov/np/Facilities/User-Facilities/RHIC`, Accessed: 2023-01-30.

[38] Z. Yang, "Measurements of higher-order cumulants of net-proton, proton and anti-proton multiplicity distributions and correlation functions in relavitistic heavy ion collisions," Ph.D. dissertation, College of Physical Science and Technology Central China Normal University, 2020.

[39] S. G. Heppelmann, "A study of the higher-order cumulants and correlation functions of event-by-event multiplicity distributions in au+au heavy-ion collisions from the rhic fixed-target program at $\sqrt{s_{NN}} = 3.0$ gev," Ph.D. dissertation, Office of Graduate Studies of the University of California Davis, 2021.

[40] M. Anderson *et al.*, "The star time projection chamber: A unique tool for studying high multiplicity events at rhic," *Nucl. Instrum. Meth. A*, vol. 499, pp. 659–678, 2003.

[41] N. Kulathunga, "Energy dependence of net-Λ fluctuations measured by the star detector at rhic," Ph.D. dissertation, Faculty of the Department of Physics of the University of Houston, 2018.

[42] D. D. Gruttola *et al.*, "A multigap resistive plate chamber array for the extreme energy events project," *J. Instrum.*, vol. 9, p. C10024, 2014.

[43] J. Adams *et al.*, "The star event plane detector," *Nucl. Instrum. Meth. A*, vol. 968, 2020.

[44] K. Meehan, "Star results from au+au fixed-target collisions at $\sqrt{s_{NN}} = 4.5$ gev," *Nucl. Phys.*, vol. 967, pp. 808–811, 2017.

[45] A. Roel *et al.*, "Centrality determination in heavy-ion collisions with the LHCb detector," *J. Instrum.*, vol. 17, no. 05, 2022.

[46] A. B. Jones and B. A. Brown, "Two-parameter fermi function fits to experimental charge and point-proton densities for ^{208}Pb," *Phys. Rev. C*, vol. 90, 6 2014.

[47] M. L. Miller, K. Reygers, S. J. Sanders, and P. Steinberg, "Glauber modeling in high-energy nuclear collisions," *Annu. Rev. Nucl. Part. Sci.*, vol. 57, no. 1, pp. 205–243, 2007.

[48] X. Luo, J. Xu, B. Mohanty, and N. Xu, "Volume fluctuation and auto-correlation effects in the moment analysis of net-proton multiplicity distributions in heavy-ion collisions," *J. Phys. G. Nucl. Part. Phys.*, vol. 40, no. 10, 2013.

[49] P. Zyla *et al.*, "Particle data group," *Prog. Theor. Exp. Phys.*, 2020.

[50] D. Kharzeev and M. Nardi, "Hadron production in nuclear collisions at rhic and high density qcd," *Phys. Lett. B*, vol. 507, pp. 121–128, 2001.

[51] C. Fuglesang, "Ua5 multiplicity distributions and fits of various functions," in *Conference on Multiparticle Dynamics*, Oct. 1989, pp. 193–210.

[52] R. L. Workman *et al.*, "Review of particle physics," *Prog. Theor. Exp. Phys.*, vol. 2022, 2022.

[53] S. Gorbunov, "On-line reconstruction algorithms for the cbm and alice experiments," Ph.D. dissertation, Faculty of Computer Science and Mathematics of the Johann Wolfgang Goethe University, 2013.

[54] M. Zyzak, "Online selection of short-lived particles on many-core computer architectures in the cbm experiment at fair," Ph.D. dissertation, Faculty of Computer Science and Mathematics of the Johann Wolfgang Goethe University, 2015.

[55] M. K. Toshihiro Nonaka and S. Esumi, "More efficient formulas for efficiency correction of cumulants and effect of using averaged efficiency.," *Phys. Rev. C*, vol. 95, 6 2017.

[56] X. Luo and T. Nonaka, "Efficiency correction for cumulants of multiplicity distributions based on track-by-track efficiency.," *Phys. Rev. C*, vol. 99, 4 2019.

[57] M. K. Toshihiro Nonaka and S. Esumi, "A general procedure for detector–response correction of higher order cumulants.," *Phys. Rev. C*, vol. 906, pp. 10–17, 2018.

[58] T. Nonaka, “Recent results and methods on higher order and off-diagonal cumulants of identified net-particle multiplicity distributions in au+au collisions at star.,” *Nucl. Phys.*, vol. 982, pp. 863–866, 2019.

[59] M. S. Abdallah *et al.*, “Measurements of Proton High Order Cumulants in $\sqrt{s_{\mathrm{NN}}} = 3$ GeV Au+Au Collisions and Implications for the QCD Critical Point,” *Phys. Rev. Lett.*, vol. 128, no. 20, 2022.

[60] X. Luo, “Error estimation for moment analysis in heavy-ion collision experiment,” *J. Phys. G. Nucl. Part. Phys.*, vol. 39, no. 2, 2012.

[61] X. Luo and T. Nonaka, “Efficiency correction for cumulants of multiplicity distributions based on track-by-track efficiency,” *Phys. Rev. C*, vol. 99, 4 2019.

[62] D. M. Ashish Pandav and B. Mohanty, “Effect of limited statistics on higher order cumulants measurement in heavy-ion collision experiments,” *Nucl. Phys.*, vol. 991, 2019.

[63] M. Bleicher *et al.*, “Relativistic hadron-hadron collisions in the ultra-relativistic quantum molecular dynamics model,” *J. Phys. G. Nucl. Part. Phys.*, vol. 25, no. 9, p. 1859, 1999.

[64] S. Basu *et al.*, “Differential two-particle number and momentum correlations with the ampt, urqmd, and epos models in pb-pb collisions at $\sqrt{s_{NN}} = 2.76$ tev,” *Phys. Rev. C*, vol. 104, 6 2021.

[65] J. Letessier and J. Rafelski, “Hadron production and phase changes in relativistic heavy ion collisions,” *Eur. Phys. J.*, vol. 35, pp. 221–242, 2008.

[66] A. Andronic, P. Braun-Munzinger, K. Redlich, and J. Stachel, “Decoding the phase structure of qcd via particle production at high energy,” *Nature*, vol. 561, no. 7723, pp. 321–330, 2018.

[67] V. Vovchenko and H. Stoecker, “Thermal-fist: A package for heavy-ion collisions and hadronic equation of state,” *Comput. Phys. Commun.*, vol. 244, pp. 295–310, 2019.

[68] V. Vovchenko, D. V. Anchishkin, and M. I. Gorenstein, “Van der waals equation of state with fermi statistics for nuclear matter,” *Phys. Rev. C*, vol. 91, 6 2015.

[69] A. Bzdak, V. Koch, and N. Strodthoff, “Cumulants and correlation functions versus the qcd phase diagram,” *Phys. Rev. C*, vol. 95, 5 2017.

[70] B. Ling and M. A. Stephanov, “Acceptance dependence of fluctuation measures near the qcd critical point,” *Phys. Rev. C*, vol. 93, 3 2016.

[71] M. Abdallah *et al.*, “Probing strangeness canonical ensemble with k, (1020) and production in au+au collisions at snn=3 gev,” *Phys. Lett. B*, vol. 831, 2022.

[72] P. Braun-Munzinger, K. Redlich, and J. Stachel, “Particle production in heavy ion collisions,” pp. 491–599, 2003.

[73] L. Adamczyk *et al.*, “Observation of an energy-dependent difference in elliptic flow between particles and antiparticles in relativistic heavy ion collisions,” *Phys. Rev. Lett.*, vol. 110, 2013.

[74] L. Adamczyk *et al.*, “Beam-energy dependence of the directed flow of protons, antiprotons, and pions in au+au collisions,” *Phys. Rev. Lett.*, vol. 112, 16 2014.

[75] J. Adam *et al.*, “Nonmonotonic energy dependence of net-proton number fluctuations,” *Phys. Rev. Lett.*, vol. 126, 9 2021.

[76] P. Braun-Munzinger, A. Rustamov, and J. Stachel, “Bridging the gap between event-by-event fluctuation measurements and theory predictions in relativistic nuclear collisions,” *Nucl. Phys.*, vol. 960, pp. 114–130, 2017.